Dual Spin-Cast Thermally Interdiffused Polymeric Photovoltaic Devices

Manpreet Kaur

Dissertation submitted to the Faculty of Virginia Polytechnic Institute and State University in partial fulfillment of the requirements for the degree of

Doctor of Philosophy
in
Physics

James R. Heflin
Richey M. Davis
Harry C. Dorn
Jean J. Heremans

August 4, 2011
Blacksburg, VA

Keywords: Organic Photovoltaics, Concentration Gradient, Interdiffusion, Conjugated Polymers

Dual Spin-Cast Thermally Interdiffused Polymeric Photovoltaic Devices

Manpreet Kaur

Abstract

An in depth study of the performance of thermally interdiffused concentration gradient polymer photovoltaic devices is carried out with particular attention to the effect of the thickness and the thermal treatments on the power conversion efficiency, short circuit current, open circuit voltage and other key electrical properties. Bilayer films of sequentially spin-cast donor and acceptor materials are exposed to various heat treatments in order to induce the interdiffusion. The depth profiles show concentration gradients in the donor and acceptor as a result of interdiffusion and these devices show an order of magnitude increase in the device performance compared to the bilayer devices. Dual spin-cast poly (3-octylthiophene-2,5-diyl) (P3OT)- [6,6] phenyl C_{61} butyric acid methyl ester (PCBM) and poly (3-hexylthiophene-2,5-diyl) (P3HT)-PCBM interdiffused devices are studied in detail by varying the thickness of the donor and acceptor layers as well as the annealing conditions for initial polymer layer and the time and temperature of the interdiffusion process.

Auger spectroscopy and X-ray photoelectron spectroscopy along with ion beam milling are used to investigate the concentration gradient formed as a result of the interdiffusion. The sulfur signal present in the P3OT and P3HT backbone is detected to identify the concentration profiles in the P3OT-PCBM and P3HT-PCBM devices. The interdiffusion conditions and thickness of the active layers have been optimized to obtain the highest power conversion efficiency. The best device performance of the P3OT-PCBM interdiffused devices is achieved when the interdiffusion is carried out at 150 °C for 20 minutes and the P3OT thickness is

maintained at 70 nm and the PCBM thickness at 40-50 nm. The highest efficiency achieved for P3OT-PCBM interdiffused devices is 1.0 % under AM1.5G solar simulated spectrum.

In order to further increase the efficiency, P3OT is replaced by (P3HT) which has higher hole mobility. P3HT- PCBM based concentration gradient devices show improved device performance over P3OT-PCBM devices. Power conversion efficiency of the order of ~3.0 % is obtained for P3HT-PCBM interdiffused devices when the interdiffusion is carried out at 150°C for 20 minutes. For both P3OT:PCBM and P3HT:PCBM devices, the optimum performance occurs when the concentration gradient extends across the entire film and is correlated with an increase in the short circuit current density and fill factor as well as a decrease in the series resistance. The results demonstrate that an interdiffused bilayer fabrication approach is a novel and efficient approach for fabrication of polymer solar cell devices.

In addition, porphyrin derivative 5, 10, 15, 20-Tetraphenyl-21H, 23H-porphine zinc (ZnTPP) is studied as a new donor material for organic solar cells. ZnTPP: PCBM blend devices are investigated in detail by varying the weight ratio of the donor and acceptor materials in blend devices. The devices with ZnTPP: PCBM in 1:9 ratios showed the best device performance and the efficiency of the order of 0.2% is achieved under AM1.5G solar simulated conditions.

Trimetallic Nitride Tempelated (TNT) endohedral fullerenes are also examined in this thesis as the novel acceptor materials. Bulk heterojunction or blend devices are fabricated with P3HT as the donor material and several TNT endohedral fullerenes as the acceptor material. $Y_3N@C_{80}$PCBH based devices which are annealed both before and after the electrode deposition show improvement in the device performance compared to devices that are only annealed before the electrode deposition. The highest power conversion efficiency achieved for TNT endohedral

fullerene devices is only 0.06%, suggesting that substantial additional work must be done to optimize the compatibility of the donor and acceptor as well as the device fabrication parameters.

I would like to dedicate my thesis to,

my dear husband and my parents

Acknowledgements

Foremost, I would like to express sincere gratitude to my advisor Prof. Randy Heflin for giving me the opportunity to work with him and for his advice, immense knowledge and constant encouragement throughout the last five years. His guidance helped me in understanding the results better and also provided direction to the work presented in this thesis.

I would also like to thank Dr. Rick Davis for his insightful discussion on the various properties of polymers and on the thermal treatments of this work. The discussion with him always brought up new possible ideas. I would like to thank Prof. Jean Heremans for being on my thesis committee and also special thanks to Prof. Harry Dorn for providing endohedral fullerenes for the study of bulk heterojunction devices of these new acceptor materials.

I am very grateful for the help provided to me by everyone in the department of Physics. I am especially very thankful to staff from machine shop Scott Allen, John Miller, Ron Stables and Fred Mahone and Dr. Norman Morgan from the electronics shop and also to Roger link and Travis Heath for their constant help. Also, thanks to Tina Lawrence for taking care of research funds and to Betty Wilkins in helping in travel arrangements for different conferences.

A special thanks to Frank Cromer and Dave Hobart for their hours of help with auger spectroscopy and also to Jerry Hunter and Steve McCartney from NCFL with their help on XPS and AFM. I would like to express my sincere thanks to Chris Thomas for being a wonderful friend and for her constant attention and help throughout last 6 years. I would like to thank Mike Kavic, Chalongrat Daengngam, Vaibhav Jain, Hunter Champion, Shahid Khan, Jason Ridley and Reza Montazami for their insightful discussions on homework and research. I am especially very

thankful to my senior colleagues Martin Drees and Anamika Gopal for their continuous guidance on various topics of research.

I would like to thank my friends Prerna, Sheetal, Anil, Arun, Rajesh, Amlan, Smita and Veena for all the support and caring they provided. I wish to thank my parents, siblings, grandparents especially Ammi for their support. Lastly and most importantly, thanks to my husband, without his love and encouragement, this thesis would not have been possible.

Table of Contents

List of Figures

Chapter 1

Chapter 2

Chapter 3

Chapter 4

Chapter 5

Chapter 6

Chapter 7

List of Tables

Chapter 2

Chapter 4

Chapter 5

Chapter 6

Chapter 7

Chapter 1

Introduction

The demand for energy is increasing globally. With advancements in technology and population increases, the demand for energy will double in the next 50 years. The main sources of energy presently are fossil fuels, which amounted to 70% of the energy production in the US in 2009. However, the combustion of fossil fuels is also primarily responsible for increased carbon dioxide concentrations in the atmosphere leading to the greenhouse effect. The Intergovernmental Panel on Climate Change (IPCC) predicts there will be an increase in temperature of between 1.8 °C and 4.0 °C by the end of the century if no action is taken [1]. Along with the harmful effects of fossil fuels, there is an additional problem that these resources are non-renewable. Hence they are bound to deplete with time and will not be sufficient for the growing energy needs. It is predicted that at the current rate of production worldwide, coal will deplete in 155 years, oil in 40 years and natural gas in 65 years [2].

These issues have motivated research into other resources of energy that are renewable and pollution free. Figure 1.1 shows the different resources used to generate electrical energy in the US in 2009. Renewable resources amounted to ~15% of the total energy generation in 2009 [3].

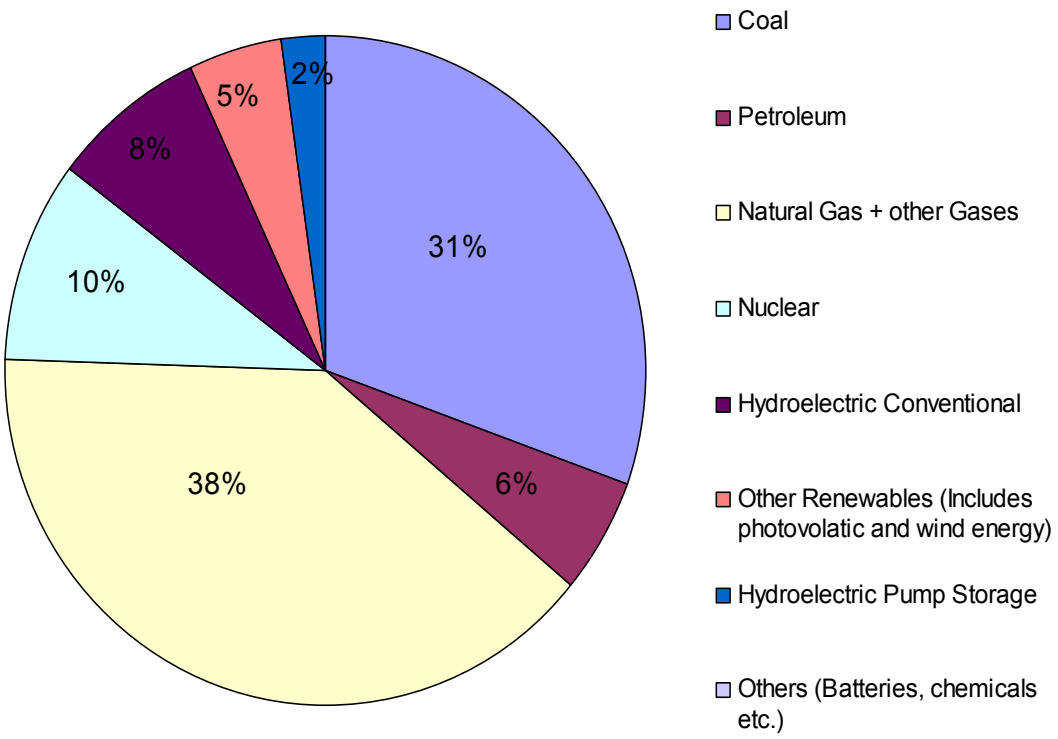

Figure 1.1 Existing capacities at U.S. electric utilities by energy source (2009). The chart shows the percentage of each energy source in the total capacity. The other renewable source includes geothermal, non-wood waste, solar, wind, wood and wood-waste.

This thesis is focused on solar energy. In particular, work has been done to improve the performance of polymeric photovoltaic devices through nanoscale control of the morphology. This is achieved by inducing thermal interdiffusion in a bilayer device consisting of a polymer donor and fullerene acceptor. The dependences on the thickness of initial layers as well as the interdiffusion conditions are the two primary issues that are studied in detail. The thickness of the polymer and fullerene layers is varied to find the optimum conditions for creation of a concentration gradient profile to maximize the device performance. The interdiffusion temperature and time are another set of parameters that are varied in order to achieve the best performance for a particular thickness. Auger spectroscopy (AES) as well as X-ray photoelectron spectroscopy (XPS) is used to monitor the concentration gradient profile. Poly (3-octylthiophene) (P3OT) and poly (3-hexylthiophene) (P3HT) are the polymers that are studied in this thesis with PCBM as the primary acceptor material. Brief studies on the bulk heterojunction blends made with P3OT:PCBM and P3HT:PCBM are also presented. A new study on the incorporation of the porphyrins as new donor materials with PCBM as the primary acceptor material is also discussed. Also, a new study on the incorporation of Trimetallic nitride tempelated (TNT) endohedral fullerenes in bulk heterojunction devices with P3HT as donor material is also discussed.

1.1 Motivation

There is a major global challenge to develop environmentally friendly and efficient renewable energy resources. One of the rapidly growing areas in the field of renewable resources is photovoltaics in which solar energy is converted to electricity. Solar energy is the most abundant renewable energy source. Our planet receives ~1.2×10^{17} W of solar power, while the rate of current worldwide energy consumption is ~10,000 times smaller at ~1.3×10^{13} W [4]. This

means that the Earth receives more solar energy in an hour than the total energy we consume in an entire year. Solar energy alone has the capacity to meet all of the global energy needs for the foreseeable future. Figure 1.2 shows the AM1.5 Global Spectrum, which considers the global clear sky intensity spectrum [6].

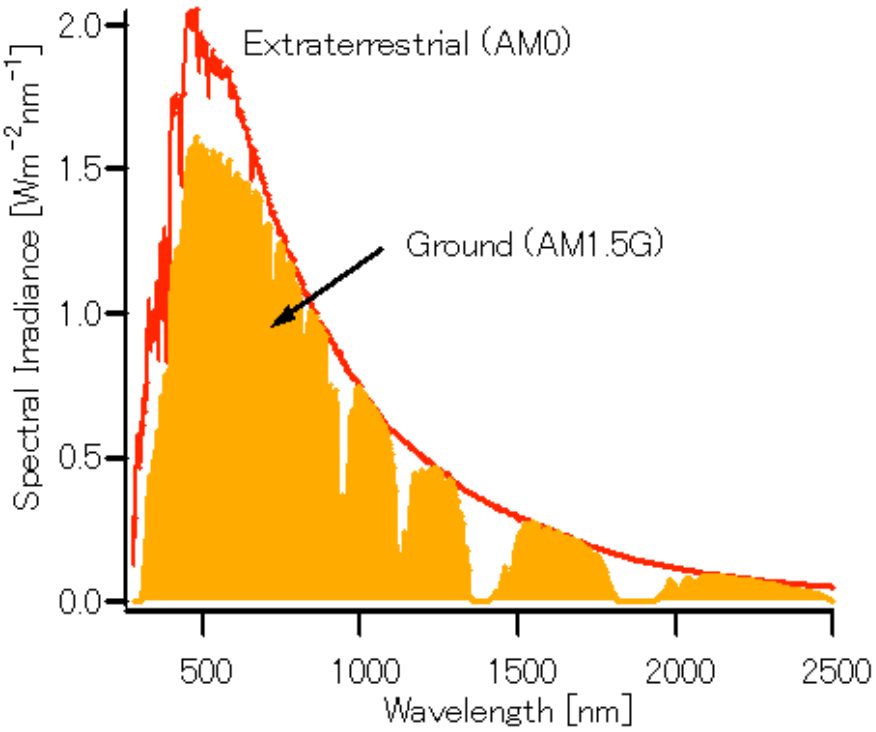

Figure 1.2 The solar spectrum for AM0 and AM1.5 irradiation. AM0 represents the solar radiation outside the earth atmosphere and AM1.5 is the spectrum at the surface when the sun makes an angle of 48° to zenith. Used under fairuse, 2011.

Thus, photovoltaics offer the potential of a clean source of electricity without the pollution concerns of coal power stations or the safety concerns of nuclear energy. However the conventional solar cells are made of crystalline silicon (c-Si). The efficiencies achieved with these materials are of the order of ~14%-16% with theoretical limiting efficiency of 29%. However the excessive cost of these devices has been a major drawback. The cost of using silicon (Si) solar cells to meet the energy requirements of the US ($40x10^{11}$ kWh) will be of the order of ~$\$5x10^{12}$.

Currently, the solar cell industry is dominated by Si solar cells. The efficiency of sc-Si has reached 24.7% and of polycrystalline Si (poly-Si) is 20.3%. Besides wafer Si, other thin film solar cell technologies have been commercialized. This includes amorphous Si (a-Si) and metal chalcogenides such as CdTe and $CuIn_xGa_{1-x}Se_2$ (CIGS) solar cells. The record efficiencies of these materials are in the range of 12%-20% [5]. The record efficiency for all solar cell technologies is held at 40.8% by tandem solar cells, which is a stack of there p-n junction of $Ga_xIn_{1-x}As$ or $Ga_yIn_{1-y}P$ [5]. The present cost of electricity generated from solar cell industry, assuming 20 year lifetime, is in the range of \$0.25-\$0.65/kWh which is much higher compared to coal based electricity which is close to \$0.04/kWh [7].

Due to the high costs of silicon or gallium solar cell systems today, they are mainly used in remote locations where there is no power line from a conventional power plant available. To make solar cell systems more competitive with fossil fuel power plants, a significant reduction in cost must be achieved. Possible alternatives to silicon solar cells include semiconductor thin films [8], the dye sensitized solar cell [9], and thin films of organic materials such as conjugated polymers [10].

1.2 Organic Photovoltaics

In polymer based solar cells, long chain conjugated polymers are used for light induced current generation. These materials should lead to devices which are cheaper and easier to fabricate. Furthermore, the potential of tuning the electrical and optical properties of polymers can lead to further improvement in device performance. The cost of organic solar cells presently is of the order of $0.40-$0.80/Kwh, assuming the efficiency of the devices is of the order of 5% with a 5 year lifetime. However, by increasing the efficiency to 15% and the lifetime to 20 years, the cost can be reduced to $0.07-$0.13/kWh, which will be comparable to the cost of energy produced by non-renewable resources [11].

In this thesis, I have concentrated on organic photovoltaic devices made with conjugated polymers in combination with fullerenes as the active layer. Conjugated polymers are relatively inexpensive and are usually soluble in the common organic solvents. Due to the solubility of these materials, device production can be relatively easier and less expensive compared to inorganic photovoltaics. Conjugated Polymers have high absorption coefficients [12], and this allows thin films to be used and hence lowers material costs. Thin films of these materials can be spin cast, doctor bladed or printed. In addition, there is the possibility of using flexible plastic substrates for organic photovoltaic devices, making the structure far more versatile than conventional silicon solar cells [13] and allowing for cheap roll-to-roll production methods. A major advantage of polymeric materials is that their optical and electrical properties are tunable by altering the molecular structure of monomer. The synthesis of such molecules is very flexible and allows electronic parameters and solubility to be altered [14].

However, the main challenges in organic photovoltaic devices are the low mobility of charge carriers [15] as well as achieving effective charge separation of electrons and holes

created by absorption of photons. Charge separation is achieved by ultrafast transfer of photoexcited electrons from the polymer to the fullerene. Ultrafast transfer of electrons from conducting polymer to fullerenes was first reported by Sariciftci *et al*. [16]. An upper limit for the electron transfer time was found to be 300 fs versus a photoluminescence time of 550 ps in the pristine polymer.

Charge transfer from the polymer to the fullerene leads to a spatial separation of electrons and holes that is needed for efficient photovoltaic devices. The range for charge transfer from the photoexcitation site has been determined within the range of 8-10 nm [17, 18, and 19]. In other words, the fullerene molecule has to be within ~10 nm of the location of the photoexcitation for the charge transfer to occur. As the electron transfer time is three orders of magnitude faster than the photoluminescence, the probability of charge transfer to occur is close to unity if the fullerene molecule is within the ~10 nm of the photoexcited electron. The close proximity of polymer and fullerene is essential for efficient device performance.

Device architectures of various types have been studied to optimize the device performance. The earliest devices studied were bilayer devices. However, bilayer devices have limited efficiency as the efficient volume is limited to a single interface between the electron donor and acceptor where charge separation can occur. In order to avoid this problem, blend devices were prepared by dissolving the electron donor and electron acceptor in a common solvent. In this device structure, a derivative of C_{60}, methanofullerene (phenyl-[6,6]-C_{61})-butyric acid methyl ester (PCBM) was most often used. The addition of the side chain by the derivatization of C_{60} renders it soluble in number of organic solvents. This approach was used by Yu *et al*. in preparing devices from the solution of a blend of poly (2-méthoxy-5-(2-éthyl-hexyloxy)-1,4-phénylène-vinylène) (MEH-PPV) and PCBM [18]. The efficiency of these devices

was 2.9% (monochromatic efficiency under 430 nm illuminations) for 1:4 MEH-PPV- PCBM blends. The efficiency of MEH-PPV and PCBM blends are found to be 1.7 times better than the efficiency of, bilayer devices of MEH-PPV and C_{60}, as donor-acceptor interfaces are present throughout the bulk of the devices; hence they are called “bulk heterojunction devices”. Due to the presence of donor acceptor interfaces throughout the bulk of devices, charge separation is enhanced compared to bilayer devices. However, charge transport is reduced by the presence of two types of materials toward each respective electrode. After the charge separation, the charges must be transported to their respective electrodes. Since, Charge transport occurs by the hopping of electrons between fullerene molecules and holes between polymer chains, transport is optimized by the pure fullerene at the cathode and pure polymer at the anode.

In order to further optimize the device performance, another device structure has been suggested where the interface is diffused but there is only one kind of material present at each electrode. This diffused structure at the interface can provide ample amount of active area for the electron-hole separation and the presence of one pure material toward the electrodes aids the uninterrupted charge transport of the electrons and holes through the acceptor and donor materials, respectively. Hence this structure allows better charge separation than the bilayer devices as well as better rectification compared to blend or bulk heterojunction devices. The increase in rectification will improve the fill factor as well as efficiency of the devices.

Several different approaches have been implemented to achieve this kind of device structure. In one, the temperature dependence of the solubility of the conducting polymer was used [21]. Poly(2-méthoxy-5-(2-éthyl-hexyloxy)-1,4-phénylène-vinylène) (MEH-PPV), exhibits good solubility in xylenes at 90 °C but is only slightly soluble at room temperature. The devices were fabricated by spin casting MEH-PPV from hot solution followed by spin casting PCBM

from room temperature xylenes solution. The device efficiencies of the order of 2.6% were achieved for these devices under monochromatic illumination.

Another approach used to attain this device structure is based on a lamination technique by Granstrom *et al*. In this technique both electron donor and acceptor materials are polymers and spin cast onto different substrates with anode and cathode. Then these two substrates are laminated under vacuum at high temperature (200 °C). Device produced in this fashion had a diffused interface but have only one kind of polymer in contact with either electrode [22]. The power conversion efficiency of 1.9% was achieved for these devices under simulated solar conditions.

"Bulk diffusion bilayer" is another approach used to achieve this device structure [23]. In this approach, a layer of MDMO-PPV was doctor bladed onto the substrate first followed by doctor blading the PCBM layer from the same solvent. The devices produced in this fashion have reduced phase separation of donor and acceptor material and hence reduction in pin holes. These devices have efficiencies comparable to blend devices of the same materials with the efficiency of the order of ~2.5% under simulated solar illumination.

In this thesis, a different approach to achieve the close proximity of polymer and methanofullerene components in a gradient structure is further developed, building on a prior work in our research group [24]. Devices are first fabricated in a bilayer structure and then interdiffusion of the fullerene into the polymer bulk is induced by heating the device at temperatures in the vicinity of the glass transition temperature of the polymer. This way, the morphology of the active layer exhibits good proximity of polymer and fullerene throughout the bulk with a concentration gradient of the two components from one electrode to the other. Most of the earlier work done in our group was based on the development of concentration gradient

photovoltaics devices with C_{60} as the acceptor layer. In that prior work, the bilayer structure was made by spin casting the first donor layer and thermally evaporating the second acceptor layer, followed by interdiffusion to achieve concentration gradient.

Previous work done in our research group has been based on the study of concentration gradient devices of MEH-PPV/C_{60}, P3OT/C_{60} and some preliminary work on dual spin cast devices of P3OT/PCBM. The studies done on MEH-PPV/C_{60} systems concluded that devices with 70 nm of polymer thickness have better performance than the devices with higher thickness and also the heat treatments done above the glass transition of the polymer leads to the enhancement in the device performance [24,25]. Device efficiency of 0.3% was achieved for MEH-PPV/C_{60} devices under monochromatic illumination. The work done on the P3OT/C_{60} showed that the device performance of interdiffused devices is better than the bilayer devices and a monochromatic efficiency of ~1.5% was achieved for P3OT/C_{60} devices interdiffused at 130 °C for 5 minutes. Further work on P3OT/C_{60} systems was done to optimize the thickness of individual layer. The best performance was achieved when the thickness of individual, P3OT and C_{60} layers was maintained in the range of 40 nm - 60 nm. Also, it was concluded that a concentration gradient extending all the way through active layers, ending just short of the electrodes gives best device performance. Preliminary studies on P3OT/PCBM dual spin cast devices achieved efficiency of the order of 0.5% under simulated solar spectrum [26].

In this thesis, work on P3OT/PCBM devices is further developed by optimizing the thickness of each layer and by optimizing the interdiffusion conditions. Also, work is done on P3HT/PCBM interdiffused systems in order to evaluate the optimized conditions for the best device performance. The results are also correlated with the short circuit currents and series resistance values and it is found that these are optimized when the overall efficiency is optimized.

Efficiency of the order of 1% has been obtained under simulated AM1.5 solar conditions for P3OT/PCBM devices and 2.7% for P3HT/PCBM devices. These conversion efficiencies are lower than the best reported (~7.4%), but in those studies different polymer and fullerene materials were used. Therefore with a different choice of materials the interdiffusion approach has a great potential for further improvement.

1.3 Outline

Chapter 2 gives an introduction to excitation processes and charge carriers in polymer and fullerene materials. This knowledge is essential to understand the charge creation and separation processes that occur in organic photovoltaic devices. Afterwards, a basic description of photovoltaic devices and their characteristics is given. Finally, a few considerations concerning heat and mass transfer related to the interdiffusion heating are discussed.

In Chapter 3, the experimental setups and methods are described. In addition, some information about the polymer and fullerene materials in the active layer is given as well as information about the electrode materials of the devices. In Chapters 4, 5 and 6, the main work of this research is described. Two different polymers were used to study the interdiffusion of polymer and methanofullerene layers starting from a bilayer of the two materials. The photocurrents as well as the current-voltage characteristics of photovoltaic cells were investigated under monochromatic as well as AM1.5G simulated solar spectrum conditions.

In Chapter 4, concentration gradient devices of poly 3-octylthiophene (P3OT) and PCBM were studied in detail. Variation in the thickness of the two layers as well the interdiffusion condition was studied in detail to analyze the optimum conditions for the P3OT/PCBM interdiffused system. The thickness of the donor and acceptor layers were varied, and it was

found that best efficiencies were obtained for devices with 70 nm of P3OT and 40-50 nm of PCBM. Interdiffusion conditions were also varied to find the best performance of the devices and it was found that devices interdiffused at 150 °C for 20 minutes had the best performance of 1.0% under AM1.5G spectrum.

To improve the performance of the devices, another polymer poly3-hexylthiophene (P3HT) was used as the mobility of charge carriers is high in P3HT [27]. In Chapter 5, interdiffused devices of P3HT/PCBM were fabricated and studied in detail. In this set of studies, interdiffusion conditions were again varied to optimize the performance of the devices. Efficiency of the order of ~3% was obtained for devices interdiffused at 150 °C for 20 minutes. The thickness was maintained at 45 nm of P3HT and 40 nm of PCBM in these devices. Concentration gradient profiles were studied using Auger spectroscopy. The series resistance of these devices was calculated and it supports the device performance. There is a drop in series resistance for device which has the best device performance.

In Chapter 6, photovoltaic device made with the incorporation of novel donor materials are studied at length. ZnTPP is introduced as new donor material and blend devices of ZnTPP: PCBM are investigated. In Chapter 7, endohedral fullerenes are introduced as the new acceptor material and bulk heterojunction devices with P3HT as the donor and TNT endohedral fullerenes are studied.

Finally, Chapter 8 contains conclusions based on the individual systems studies. Suggestions are also made for further improvements of the device performance in future work.

References

1. Intergovernmental Panel on Climate Change. Climate change 2007: The physical science basis. Technical report, United Nations, 2007.

2. http://earthtrends.wri.org/updates/node/100

3. http://www.eia.doe.gov/neic/brochure/renew05/renewable.html

4. U.S. Department of Energy, Basic Research Needs for Solar Energy Utilization (2005).

5. M. Tao, "Inorganic Photovoltaic Solar Cells: Silicon and Beyond", The Electrochemical Society Interface, 30-35, Winter (2008)

6. http://rredc.nrel.gov/solar/spectra/am1.5/

7. A. Slaoui and R.T. Collins, "Advanced Inorganic Materials for Photovoltaics", **MRS Bulletin**, 32, 211-218, (2007).

8. M.A. Green. "Solar cells: operating principles, technology, and system applications", University of New South Wales, Kensington, N.S.W., (1992).

9. M. Gratzel. **Nature**, "Photoelectrochemical cells", 414 (6861):338–344, (2001).

10. R.A.J. Janssen, J. C. Hummelen, and N. S. Sariciftci, "Polymer–Fullerene Bulk Heterojunction Solar Cells",**MRS Bulletin**, 30, 33–36, 2005.

11. J. Kalowekamo , E. Baker, "Estimating the manufacturing cost of purely organic solar cells", **Solar energy**, 83, 8, 1224-1231, (2009)

12. H. Hoppe and N. S. Sariciftci, "Organic solar cells: An overview", **Journal of Materials Research**, 19 (7), 1924–1945, (2004).

13. M. Al-Ibrahim, H. K. Roth, U. Zhokhavets, G. Gobsch, and S. Sensfuss, "Flexible large area polymer solar cells based on poly(3-hexylthiophene)/fullerene", **Solar Energy Materials & Solar Cells**, 85, 13–20, (2005).

14. S. E. Shaheen, D. S. Ginley, and G. E. Jabbour, "Organic-Based Photovoltaics: Toward Low-Cost Power Generation", **MRS Bulletin**, 30:10–19, (2005).

15. C.D. Dimitrakopoulos and D.J. Mascaro, "Organic thin-film transistors: A review of recent advances."**IBM J. Res. Dev.** 45 (1), 11, (2001).

16. B. Kraabel, D. McBranch, N.S. Sariciftci, D. Moses, A.J. Heeger, "Ultrafast spectroscopic studies of photoinduced electron transfer from semiconducting polymers to C_{60}", **Phys. Rev. B** 50(24), 18543-18552, (1994).

17. D. Vacar, E.S. Maniloff, D.W. McBranch and A.J. Heeger, “Charge-transfer range for photoexcitations in conjugated polymer/fullerene bilayers and blends”, **Phys. Rev. B** 56(8), 4573-4577, (1997).

18. J.J.M. Halls, K. Pichler, R.H. Friend, S.C. Moratti, A.B. Holmes, “Exciton diffusion and dissociation in a poly(p-phenylenevinylene)/C_{60} heterojunction photovoltaic cell.” **Appl. Phys. Lett.** 68 (22), 3120-3122, (1996).

19. A. Haugeneder, M. Neges, C. Kallinger, W. Spirkl, U. Lemmer, , J. Feldmann, “Exciton diffusion and dissociation in conjugated polymer / fullerene blends and heterostructures”, **Phys. Rev. B**, 59 (23), 15346–15351, (1999).

20. G.Yu, J.Gao, J.C. Hummelen, F.Wudl, A.Heeger, “Polymer Photovoltaic Cells: Enhanced Efficiencies via a Network of Internal Donor-Acceptor Heterojunctions”, **Science** 270 (5243), 1789-1791, (1995).

21. F. Zhang, M. Johansson, M.R. Andersson, J.C. Hummelen, O. Inganas, “Polymer Photovoltaic Cells with Conducting Polymer Anodes”, **Advanced Materials** 14(9), 662-665, (2002).

22. M. Granstrom, K. Petritsch, A.C. Arias, A. Lux, M.R. Andersson, and R.H. Friend, “Laminated fabrication of polymeric photovoltaic diodes”,**Nature** 395, 257, 1998.

23. C.J. Brabec, A. Cravino, D. Meissner, N.S. Sariciftci, M.T. Rispens, L. Sanchez, J.C. Hummelen, T. Fromherz, , “The influence of materials work function on the open circuit voltage of plastic solar cells”, **Thin Solid Films** 403-404, 368-372, (2002).

24. M. Drees, K. Premaratne, W. Graupner, J.R. Heflin, R.M. Davis, D. Marciu, M. Miller, “Creation of a Gradient Polymer-Fullerene Interface in Photovoltaic Devices by Thermally Controlled Interdiffusion.” **Applied Physics Letters** 81(24), 4607-4609, (2002).

25. M. Drees, R.M. Davis, J.R. Heflin, “Improved Morphology of Polymer-Fullerene Photovoltaic Devices with Thermally Induced Concentration Gradients." **J. Appl. Phys.** 97 (3), 036103, (2005).

26. A. Gopal, “Effects of Thickness, Morphology and Molecular Structure of Donor and Acceptor Layers in Thermally Interdiffused Polymer Photovoltaics”, (2007).

27. A. Zen, M. Saphiannikova, D. Neher, U. Asawapirom, and U. Scherf, “Comparative Study of the Field-Effect Mobility of a Copolymer and a Binary Blend Based on Poly(3-alkylthiophene)s.”**Chem.Mater.**,17(4),781-786,781,(2005).

Chapter 2

Background on Polymer Photovoltaics

This chapter is primarily aimed as an introduction and description of the evolution of organic photovoltaics as well as to explain the basic aspects of polymer photovoltaics. Polymers (plastics) have been heavily studied and commercialized for more than fifty years because of their attractive mechanical and structural properties. However, with the discovery of conducting properties of polymers in the late 70s [1], intense research started on this new class of materials showing that polymers can be semiconducting to conducting with conductivity values as high as 100,000 S/cm. Hence, this new class of materials has conductivities equivalent to inorganic conductors and semiconductors along with mechanical flexibility. The electrical and optical properties of polymers can be quite similar to inorganic materials. However, the mechanism of charge transfer and transport are quite different. In this chapter, the theory behind organic solar cells, charge transfer and charge transport mechanisms as well as various aspects of I-V curves are explained in detail. Here the aim is to provide basic understanding of characteristics of solar cells with a focus on organic solar cell devices. The next section gives a brief historic overview of the evolution of organic photovoltaics to its current form. The subsequent sections will discuss the theory behind the functioning of current organic solar cells.

2.1 History of Polymer Solar Cells

The credit for the discovery of the photovoltaic (PV) effect goes to Becquerel [2] in 1839, who discovered a photocurrent when platinum electrodes, covered with silver bromide or silver chloride, were illuminated in aqueous solution. However, anthracene was the first organic compound in which photoconductivity was observed by Pochettino in 1906 and Volmer in 1913. Chlorophyll was one of the earlier compounds discovered to exhibit a photovoltaic-like effect in nature, as plants convert light to energy through the process of photosynthesis. In 1959, Kallmann and Pope observed a photovoltaic effect in a single crystal of anthracene when sandwiched between two identical electrodes and illuminated from one side [3]. Early organic PV devices also consisted of either a liquid active layer of chlorophyll solutions or microcrystalline films of chlorophyll or other dyes such as phthalocyanines sandwiched between metal electrodes with offset work functions. However, these materials had poor conductivity and in addition, in these devices charge generation takes place in a thin layer at the metal-organic interface and hence photovoltaic cells using such materials yielded low power conversion efficiencies. In order to improve the efficiency of the devices based on these molecules, bilayer devices were made with the combination of electron transporting dyes such as rhodamines or perylene with hole transporting dyes such as phthalocyanines. Tang *et al.* reported an efficiency of 1% for these devices with perylene derivative as n type material in 1986 [22]. The discovery of metal-like electrical conductivity in conducting polymers in 1976 by Shirakawa, Heeger and MacDiarmid, which was induced by doping of conjugated polymers, such as polyacetylene with halogens, opened the field of research of polymer photovoltaics [4].

In 1982 Weinberger *et al*. investigated polyacetylene as the active material in a polyacetylene/graphite solar cell, however the efficiency of these devices was of the order of

0.3%. Glenis *et al*. further investigated different polythiophenes in solar cell devices [5]. These devices, too, had low power conversion efficiencies. The discovery of electroluminescence in poly (*p*-phenylene vinylene) (PPV) films, led to the study of semiconducting properties of conjugated, conducting polymers and their potential use in flexible large area light emitting displays [6]. Although these initial devices had a rather low current output when operated in the reverse mode, this triggered interest in conducting polymers for organic photovoltaics. The conducting polymers in the initial studies were insoluble and to obtain them in film form involved lengthy processing of precursor forms of the polymer. The development of solution processible conducting polymers by suitable funtionalization results in the easier processing of solar cell devices. [7]. Poly (alkyl-thiophenes) (PATs), PPV and its derivatives are the most heavily investigated conjugated polymers in PV devices. The next few sections describes the mechanism of the operation of organic photovoltaic devices followed by the different architectures adopted for the devices made with conducting polymers as donor material and the fullerene or its derivative as an acceptor material.

2.2 Polymeric Solar Cells

Polymeric solar cells consist of semiconducting polymers as donor and typically a fullerene or its derivative as acceptor materials sandwiched between electrodes where the donor plays a role similar to the p-type and the acceptor, the n-type material, analogous to an inorganic solar cell.

2.2.1 Semiconducting Polymers

Semiconducting polymers can usually be described as quasi-one-dimensional conjugated polymers, which refers to the alternating single and double bonds between the carbon (and other)

atoms on the polymer backbone. The double bonds result from the fact that, while carbon has four valence electrons, the carbon atoms in conjugated molecules bind to only three (or two) other atoms, hence the carbon atoms have sp^2 (or sp) hybridization. In the case of sp^2 hybridization three of the four valence electrons of carbon participate in the σ backbone, and one of the double bond is the localized covalent bond formed with this sp^2 hybridized orbital (Figure 2.1(a)). The second bond in the double bond is formed by overlapping un-hybridized p_z orbitals resulting in π electron bonds that are delocalized over the entire molecule [8,9]. The π bonds are the basic source of conduction in the conjugated systems. The conjugation length along the polymer chain can be interrupted (e.g. by foreign atoms, bending of the polymer chain, or crosslinks) and is typically less than 100 nm.

As a result of the long-range interaction of the π electrons of carbon atoms, there is a band-like splitting of energy levels. The band edge of the valence band is referred to as the "Highest Occupied Molecular Orbital" (HOMO) and the edge of the conduction band is called the "Lowest Unoccupied Molecular Orbital" (LUMO) (Figure 2.1(b)).

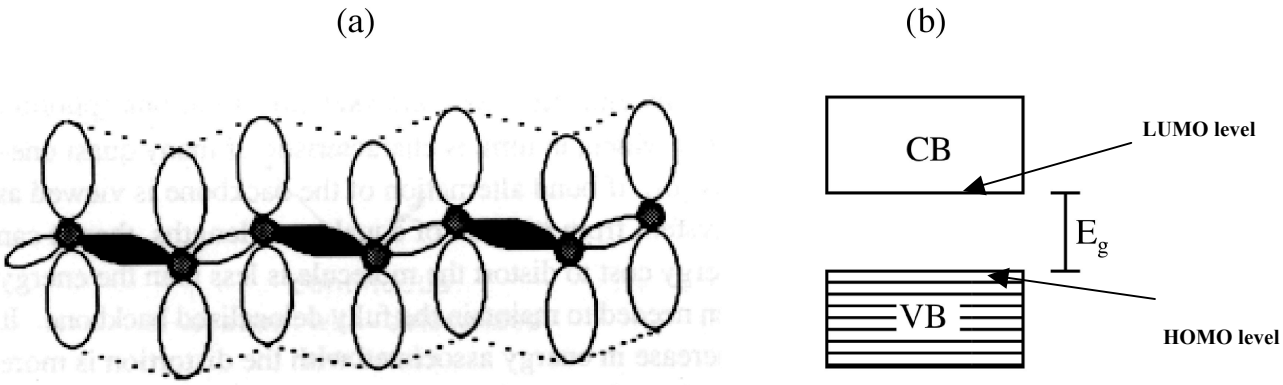

Figure 2.1 (a) Alternating single and double bonds along the conjugated polymer chain. (b) Energy level splitting to form the conduction and valence bands.

Conjugated polymers have semiconductor-like electronic properties along with the processing advantages of polymers. Also, the bandgap of the polymer is tunable enabling tailoring of electronic and optical properties. The band gap of the conjugated polymers is typically in the range of 1-4 eV [10].

2.3 Overview of Organic Photovoltaic Process

The basic operation of the organic photovoltaic process is described in Figure 2.2. The process of conversion of light into electricity by an organic solar cell involves the following steps. The initial process involves the absorption of a photon leading to the formation of an excited state, (bound electron-hole pair (exciton) creation). This is followed by diffusion of exciton to a region where exciton dissociation, (charge separation) can occur. Finally, there is the charge transport within the organic semiconductors to the respective electrodes.

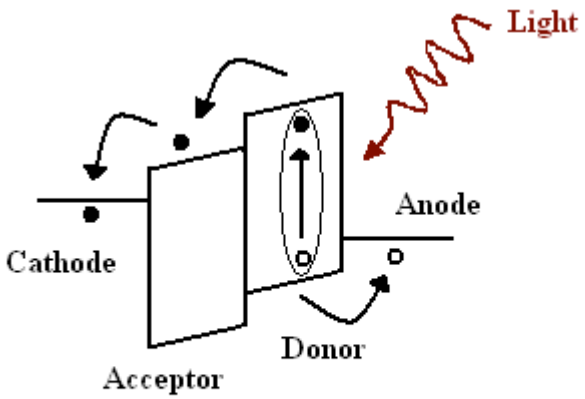

Figure 2.2 Basic operation of organic solar cell; exciton formation in semiconducting donor material, charge separation, and electron transport to the cathode and hole transport to the anode.

The basic stepwise process for photo excitation on a donor (D), charge transfer to a nearby acceptor (A) and charge separation is discussed in Table 2.1[8]. Here, 1 and 3 indicate if the excited state is singlet or triplet. In the initial step, photoexcitation in the donor upon the absorption of light leads to the formation of singlet/triplet excited states called excitons. In the second step, there is the formation of a donor-acceptor complex, when the donor is in the vicinity

of the acceptor and there is delocalization of the excitation on the D-A complex. In the third step, electron transfer to the high electron affinity acceptor is initiated. Here δ denotes the fraction of charge transferred, where δ =1 is the state when the whole electron is transferred leading to the formation of the ion-radical pair in the fourth step. In the final step, D-A complex dissociates to give positive donor and negative acceptor, hence completing the charge transfer process. The separated charge carriers hop along the well-connected path till they reach the respective electrode.

Table 2.1 Stepwise process of photo-excitation, charge transfer and charge separation.

Steps of photovoltaic process	
Initial step	$D + A \rightarrow {}^{1,3}D^{*} + A$
Second step	${}^{1,3}D^{*} + A \rightarrow {}^{1,3}(D-A)^{*}$
Third step	${}^{1,3}(D-A) \rightarrow {}^{1,3}(D^{\delta+} - A^{\delta-})*$
Fourth step	${}^{1,3}(D^{\delta+} - A^{\delta-})* \rightarrow {}^{1,3}(D^{+\bullet} - A^{-\bullet})$
Final step	${}^{1,3}(D^{+\bullet} - A^{-\bullet}) \rightarrow D^{+\bullet} + A^{-\bullet}$

In the following sections, a more detailed description of the photoexcitation, charge transfer and charge transport process are given.

2.3.1 Photoexcitation

Photoexcitation results in the formation of different quasi-particles, (exciton, polarons and bipolarons) in the non-degenerate ground state conjugated polymers.

A. Exciton

An exciton is a bound electron-hole pair which is one of the predominant species formed as a result of excitation of a polymer. This bound electron-hole pair is weakly bound and is held together by Coulomb interaction. Exciton nomenclature is different depending on its delocalization. If the exciton is localized, it is called a Frenkel exciton. If it is delocalized over many molecular units, it is called Mott-Wannier type of exciton [8]. Exciton states can be singlet (spins are antiparallel) or triplet (spins are parallel) in nature. However, singlet excitons are of most interest as photoexcitation directly produces singlet exciton as a result of conservation of spin. The triplet exciton is localized on the chain, and hence is called a Frenkel exciton while the singlet exciton was found to be delocalized over many molecular units of the polymer and hence is called a Mott-Wannier type of exciton. The typical lifetime of singlet excitons is in the hundreds of picoseconds after which they can recombine radiatively or nonradiatively [12] and the diffusion length is typically of the order of ~10 nm.

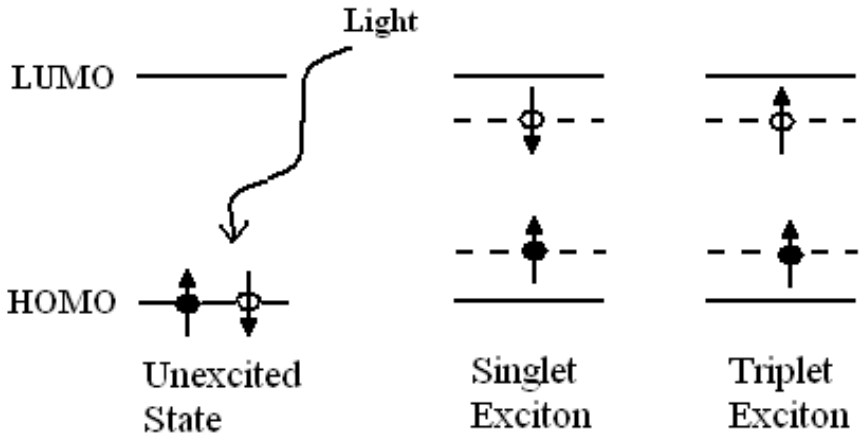

Figure 2.3 Singlet and triplet exciton states.

B. Polarons

Polarons are charged quasi-particles which induce a lattice deformation. Polarons give rise to the states within the forbidden bandgap. Hence, a polaron is a charged particle with lattice deformation. Polarons can be positively charged (P^+) or negatively charged (P^-). Polarons can increase the energy of the associated molecule and hence can induce a bond configuration, leading to part of the chain changing from one structure to another [11].

2.3.2 Charge Transfer

In organic semiconductors, charge transfer occurs at the interface of the donor (D)-acceptor (A) through exciton dissociation. The separated charge carriers after the charge transfer hop towards the respective electrodes by inter-chain and intra-chain transport of charge carriers. The discovery of ultrafast charge transfer from the conducting polymer poly(2-methoxy, 5- (2'-ethylhexyloxy)-1.4-phenylene-vinylene) (MEH-PPV) to the acceptor C_{60} by Sariciftci *et al*. has been the initiator for the work being done on polymeric solar cells [12] The main factors that affect the charge transfer are electron affinity of the acceptor (A_A), ionization potential of the donor in the excited state (I_D^*) and the Coulomb attraction of the separated radicals (U_C). Here, Coulomb attraction summarizes all the electrostatic interactions including the exciton binding energy and all polarizations. In order to have effective charge transfer, the electron affinity of the acceptor should be greater than the ionization potential of the donor in its excited state and net Coulomb forces and can be expressed as,

$$I_D^* - A_A - U_C < 0 \qquad .$$

The range of the charge transfer process from electron to donor in polymer-fullerene systems has been found to be ~10 nm [13] and the time of charge transfer has been found in the range of 300 femtoseconds (fs) [14]. The reported time scale of charge transfer is 1000 times faster than the time scale of electron-hole radiative recombination and charge transfer dominates the recombination at the donor-acceptor interface.

The actual mechanism of charge transfer is still debated. Halls *et al*. proposed the diffusion model which states that the singlet excitons diffuse from the location of photoexcitation to the

polymer-fullerene interface and are dissociated at the interface [15]. They studied the photovoltaic response in heterojunction devices prepared from poly (phenylenevinylene) (PPV) and C_{60} and modeled the photocurrent spectra under the assumption that all absorbed photons create singlet excitons and all singlet excitons within the diffusion range of the interface are dissociated and contribute to the photocurrent. From the quantitative agreement of the modeled current spectra and the experimental spectra they proposed a diffusion range of 6-8 nm and concluded that the agreement is strong evidence in support of their diffusion model. This diffusion model is disputed by Vacar *et al*. [13]. They found that with the time scale of picoseconds and diffusion range of ~10 nm, the diffusion constants and mobility in the polymer would have to be at least 2 times higher than what they are assumed to be, where the mobility is related to the diffusion coefficient,

$$\mu = \frac{eD}{k_B T} \quad .$$

They suggested that the wave function of the primary excitation on the polymer must spatially extend over ~10 nm in order to explain the charge transfer. Further analysis of their experiment also reported a diffusion range of the order of ~10 nm.

Although there is disagreement on the actual mechanism of charge transfer, there is, however, consensus on the charge transfer range. The charge transfer range is found between 8 to 10 nm, which means if there is an excited donor species within 8-10 nm of the acceptor, there will be nearly 100% probability for the charge transfer to occur.

2.3.3 Charge Transport

The separated charge carriers at the donor-acceptor interface transport to the respective electrodes by interchain hopping. The field created due to the offset in the work function of the collecting electrodes, guides the motion of charge carriers from one molecule to another. In the absence of external bias, the difference in the work function of electrodes gives rise to an internal field (band bending, V_{bi}). This internal electric field guides the motion of charge carriers to the respective electrodes.

Bredas *el al*. studied the charge hopping between adjacent polymer chains. They did a study on the transfer integrals which is an indicator of the strength of interaction between any two species where charge hopping can occur and deduced that large transfer integrals are required in order for charge hopping to occur [16]. Hence, a close proximity of molecules, well-connected path and an offset in the work function of electrodes are all required for the effective charge transfer to the electrodes.

2.4 Process that Hinder the Photovoltaic Process

A. Photo-oxidation or Oxygen Traps

Photo-oxidation occurs in polymers as a result of simultaneous exposure to light and oxygen. In some polymers, such as PPVs, photo-oxidation of the vinyl group leads to the formation of carbonyl. These carbonyls act as high electron affinity sites where exciton dissociation can occur. However, they do not contribute to photocurrent as they are not D-A interface sites, hence charge separation cannot occur. These charges remain trapped on these sites and contribute to space charge accumulation. However, the polymers used in this thesis work are polythiophenes and it has been found that thiophenes show a higher stability in the oxygen rich environment [17]. In oxygen rich environment, polythiophenes resist the photo-oxidation and

hence are stable but they lead to the formation of carbonyl which leads to the chain scission, hence reducing the conjugated chain length and as a consequence reducing the electronic conductivity of polymers [18].

Hence, all of the processing and characterization of the polymeric photovoltaic devices should be done in the oxygen free environment.

B. Traps

Traps are localized sites that trap the charge carriers and thus hinder the photovoltaic process. There are two types of traps, shallow and deep traps. Traps are a result of structural defects in the polymer chain, oxidation sites or impurities. In shallow traps, charge carriers are trapped for a limited amount of time, which increases the time taken by the charged particle to reach the electrode. The increase in the time of flight of charge carriers decreases the mobility of charge carriers. The mobility of the charge carriers decreases as the time of flight and the density of traps increases. The effective mobility can be expressed as,

$$\mu_{eff} = \frac{L}{\tau_{eff} E} \quad .$$

Here τ_{eff} is the total effective time of a charge to the electrode, L is the diffusion length for the charge and E is the electric field. The total effective time is given by,

$$\tau_{eff} = \tau_0 + N\tau_{trap} \quad .$$

τ_{eff} is the combination of time spent by the charge carrier in the trap-free region (τ_0) and τ_{trap} is the time spent by the charge carrier in the trapped site. Here N is the average number of traps encountered in the path.

Deep traps are the regions where the charge carrier can be trapped for a long period of time, which reduces the available charge carriers for charge transport. Hence, it results in the build-up of the space charges, which results in the decrease of conductivity as well as mobility of the charge carrier.

C. Recombination

Electron-hole recombination is another one of the critical processes that hinder the photovoltaic process. The exciton formed by photon absorption has a lifetime of the order of picoseconds after which the electron and hole combine radiatively or non-radiatively. In the absence of D-A interface near the photoexcitation site, recombination dominates, as charge transfer can not occur within the lifetime of exciton. Recombination of charges can be avoided by increasing the donor-acceptor interface throughout the bulk of the device as well as by making sure that device processing occurs in an oxygen free environment so that there are no traps.

2.5 Architecture of Polymer Solar Cell Devices

In polymer solar cells devices, different architectures of the devices have been employed for the efficient separation of bound electron-hole pairs. In polymer solar cell devices, the conjugated polymer absorbs the incident light. The absorption process generates an exciton that can either relax back to the ground state or dissociate into an electron and a hole. Since, in organic cells, exciton diffusion lengths are small and the dissociation process only occurs at the donor/acceptor interface, controlling the structure of the active layer is very important to constructing efficient devices. In the following, the most typical device architectures and their individual advantages and disadvantages are discussed. Their main difference lies in the exciton

dissociation or charge separation process, which occurs at different locations within the photoactive layer. A second issue is the consecutive charge transport to the electrodes.

A. Single Layer

The first organic solar cells were based on single thermally-evaporated molecular organic layers sandwiched between two metal electrodes of different work functions. The earliest photovoltaic devices were made with non-polymeric organic semiconductors. The rectifying behavior of these devices can be explained by the metal-insulator-metal (MIM) model [2]. The potential difference in these devices is the difference in the work function of the metal electrodes when no external voltage is applied. However, this potential difference is not high enough to provide efficient photoinduced charge generation. As the exciton diffusion length for most organic solar cell materials is close to ~10 nm, only those excitons generated in a small region within ~10 nm from the contacts contribute to the photocurrent. Hence, the short exciton diffusion length combined with poor electron mobility results in very low power conversion efficiency, typically of the order of 10^{-3} %. However, in 1978, Ghosh *et al.* reported an efficiency of 0.7% for single layer devices made with merocyanine dyes [19]. Here, an organic layer is sandwiched between a metal–metal oxide and a metal electrode, thus enhancing the Schottky-barrier effect. It is termed as metal-insulator-semiconductor (MIS) device. Figure 2.4 shows the schematic of the single layer device [2]. The open circuit voltages (V_{oc}) observed was not much lower than the current organic counterparts; however the photocurrent densities and efficiencies had much room for improvement. With the development in the field of conjugated polymers, single layer devices made with these materials were introduced. However, the efficiency of these devices was also quite low, with power conversion efficiency of the order of 0.1% [20]. The observation of photoinduced transfer from conjugated polymers to C_{60} in 1992, led to the

development of the polymer / fullerene bilayer and bulk heterojunction devices [21]. The first successful donor-acceptor bilayer devices based on non-polymeric organic molecules was built in 1985 and is explained in detail in the subsequent sections.

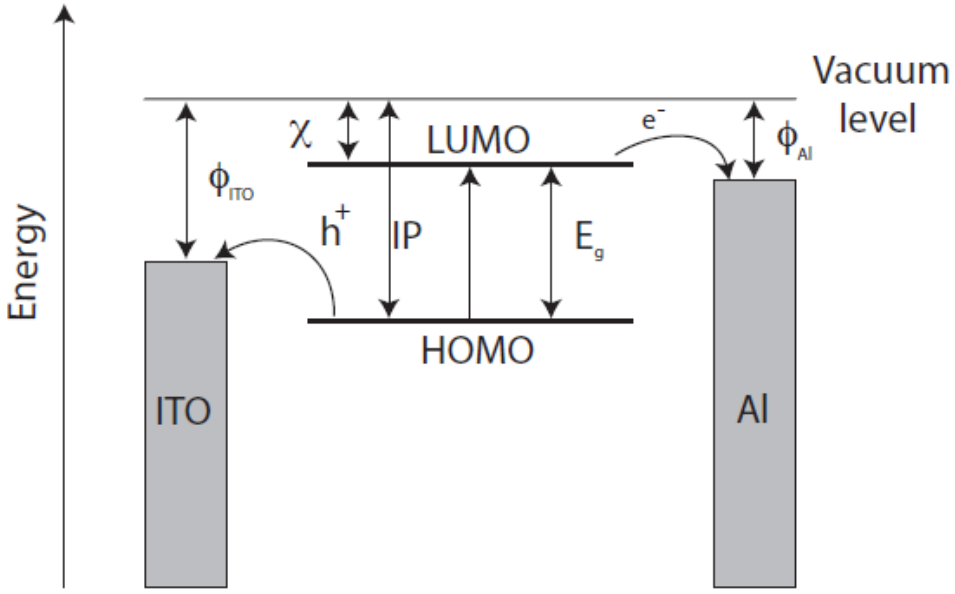

Figure 2.4 Charge generation process in a single layer conjugated polymer device, here, LUMO: lowest unoccupied molecular orbital, HOMO: highest occupied molecular orbital, ϕ: the work function, χ : the electron affinity, IP : Ionization potential, E_g : Optical band gap.

B. Bilayer Heterojunction

In a bilayer device, a donor and an acceptor material are stacked together with a planar interface. It is there that the charge separation occurs, which is mediated by a large potential drop between the donor and acceptor at the planar interface. However, as the volume where charge separation can occur is limited, so is the efficiency of this device too. The bilayer is sandwiched between two electrodes appropriate to the donor HOMO and the acceptor LUMO, for efficient

extraction of the corresponding charge carriers [Figure 2.5]. This requires an anode with a work function higher than the HOMO of the donor and a cathode with a work function lower than the LUMO of the acceptor. Rectification is observed in the current-voltage characteristics of such devices as is evident from energy band diagram of the bilayer [2].

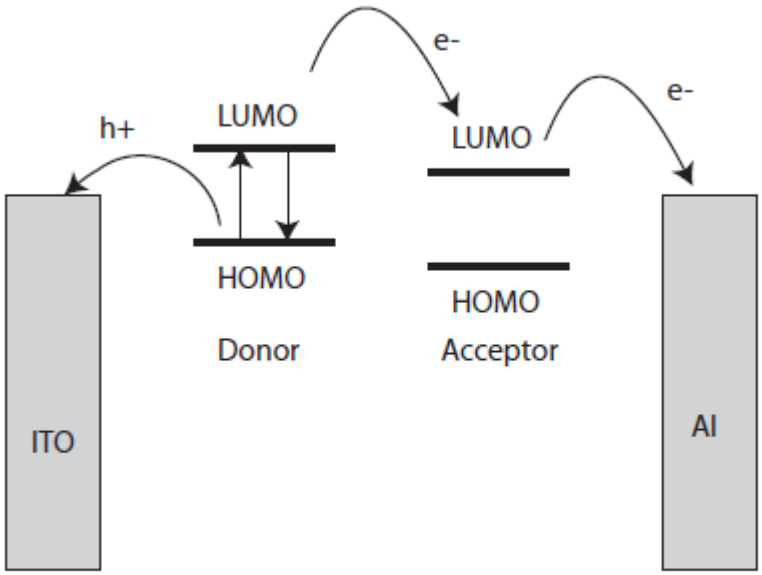

Figure 2.5 Schematic of exciton dissociation at the donor–acceptor interface. The electron goes to the acceptor while the hole stays on the donor.

In 1986, Tang *et al*. reported one of the initial successful non-polymeric organic semiconductor bilayer devices. This bilayer device with a phthalocyanine derivative as p-type semiconductor and perylene as n-type semiconductor had a power conversion efficiency of 1% [22]. Sariciftci *et al*. first used this approach for a polymeric bilayer device in which C_{60} is evaporated on the top of spin-cast MEH-PPV layer [23]. The efficiency of these bilayer devices was quite low. However Halls *et al.* demonstrated an increase in the efficiency of the devices

made with the same materials by optimizing the thickness of the two layers [15]. As the exciton diffusion length in conjugated polymers has been found to be in the range of ~10 nm, the efficiency of bilayer devices is limited by the number of photons that can be utilized within the exciton diffusion length of the interface.

C. Bulk Heterojunction

Since the exciton dissociation is most effective at the interface of donor and acceptor, the exciton should be within the diffusion length of such an interface. The diffusion length is in the range of ~10 nm for organic semiconductors however device thicknesses of that range are not sufficient for harvesting a substantial fraction of the light. This problem can be overcome by blending the donor and acceptor, a concept called dispersed (or bulk) heterojunction. Bulk heterojunctions are based on mixing the donor and acceptor materials in a bulk volume so that donor-acceptor interfaces are present throughout the bulk of the device. In this architecture, D-A interfaces are present within the exciton diffusion length of each absorbing site, hence increasing the interfacial area where charge separation can occur. Yu *et al*. first fabricated a bulk heterojunction device by blending MEH-PPV with a soluble form of C_{60}, (6,6)-phenyl C_{61}-butyric acid methyl ester (PCBM) [24]. These devices had a significant increase in the device performance compared to bilayer devices of MEH-PPV/C_{60}. Shaheen *et al*. further showed that the device performance of the bulk heterojunction devices can be improved significantly by using a solvent that prevents the long-range phase separation and hence enhances the polymer chain packing [25]. They studied bulk devices of MDMO-PPV with PCBM in 1:4 and found that devices fabricated with chlorobenzene as solvent had better performance compared to devices spin casted from toluene with AM1.5 power conversion efficiency of the order of ~2.5%. The next breakthrough in bulk heterojunction devices was the use of the P3HT as donor polymer in

place of PPV derivatives, and the devices based on blends of P3HT: PCBM had an efficiency of 3.5% under AM1.5G conditions [26]. Through further refinements in processing, solution cast P3HT: PCBM blends have yielded greater than 5% power conversion efficiency under AM1.5G [27, 28]. The current record efficiencies, using low bandgap thiophenes-based polymers, are 7.4% under AM1.5 conditions [29]. Bulk heterojunctions have significant advantage over bilayer devices in terms of charge transfer, however charge transport is limited by the presence of the interpenetrating network near the electrodes.

D. Diffuse Bilayer Heterojunction

This device architecture is meant to adopt the advantages of both increased D-A interface and uninterrupted pathway for charge transport. This architecture is in-between the bilayer and bulk heterojunction. The diffuse interface is achieved in different ways:

(i) If processed from solution, two thin polymer films can be pressed together in a lamination procedure applying moderate pressure and elevated temperatures [30]. These laminated devices had a power conversion efficiency of 2% under AM1.5G conditions.

(ii) Another way to achieve a diffuse interface is to spin coat the second layer from a solvent that partially dissolves the underlying polymer layer. [31, 32]. In our work, a diffusion bilayer is achieved by heating the bilayer device at elevated temperatures. By interdiffusing the device at a higher temperature results in the intermixed interfacial region in the bulk however there is only one kind of material present towards the electrodes. Power conversion efficiency of ~3% has been achieved for the bilayer diffused devices made with P3HT as a donor and PCBM as an acceptor [31].

The diffused bilayer architecture offers the potential advantage of increased D-A interface area without compromising the charge transport of charge carriers.

2.6 Photovoltaic Characterization of Organic Solar Cells

In the following, the main properties used to characterize the photovoltaic behavior of organic solar cells are described. This section provides a basic understanding of organic photovoltaic devices. The parameters that are used to describe the performance of the device and I-V characteristics of the device are explained.

2.6.1 Parameters Characterizing Solar Cells

A. External Quantum Efficiency (EQE) and Photoresponsivity (PR)

EQE and PR are wavelength-dependent quantities and are extracted from the current measurements made under illumination. The current spectral response obtained from a solar cell for a particular illumination helps determine electrical energy conversion capability at a particular wavelength. PR is defined as the ratio of photocurrent extracted as a function of incident power at a particular wavelength,

$$\mathrm{PR} = \frac{I_{sc}(\lambda)}{P_{source}(\lambda)} \quad .$$

Here $I_{sc}(\lambda)$ is the short circuit current, the value of current obtained when no bias is applied to the device at a specific illumination wavelength. $P_{source}(\lambda)$ is the incident power of illumination at that specific wavelength.

EQE is very important parameter as it gives information on the efficiency of generating and collecting free electrons and holes, when a solar cell is illuminated by a particular wavelength. Hence EQE is the conversion efficiency of incident photons to extracted electrons,

$$\text{EQE}(\lambda) = N_e / N_{ph}$$

Here N_e is the number of electrons extracted and N_{ph} is the number of photons incident. Thus, the EQE is the fraction of incident photons that generate an electron collected in the photocurrent.

EQE can also be calculated from photoresponsivity as,

$$PR(\lambda) = \frac{I_{sc}(\lambda)}{P_{source}(\lambda)} = \frac{eN_e / \Delta t}{h\nu N_{ph} / \Delta t}$$

Hence EQE can be expressed as,

$$EQE(\lambda) = \frac{hc}{e} * \frac{PR(\lambda)}{\lambda} \quad .$$

Here, h is Planck's constant and c is the speed of light in vacuum. EQE has no units and is expressed in terms of percentage.

B. IV Characteristics – Short Circuit Current, Open Circuit Voltage, Fill Factor, Power Conversion Efficiency, Series and Shunt Resistance

The current-voltage curve is obtained by applying the variable voltage and measuring the current obtained. These curves are measured in dark as well under monochromatic and solar spectrum illuminations. The typical current voltage curve of a solar cell is shown in Figure 2.6.

Figure 2.6 shows an example of the I-V curve under dark and illumination. Some important parameters that are used in calculation of efficiency of solar cells have been labeled.

- Short circuit current (I_{sc}): I_{sc} is the maximum current value obtained at a particular illumination under zero bias. I_{sc} occurs at the beginning of forward bias sweep and is given by intersection of I-V curve with the y-axis in the 4th quadrant.
- Open circuit voltage (V_{oc}): V_{oc} is the value of voltage when the current passing through the cell is zero and is given by the intersection of I-V curve with x axis.

As the external applied voltage is increased from zero, the photocurrent decreases and at a given external bias, it becomes zero. This occurs when the external voltage is exactly opposite to the voltage generated by the solar cell. This bias value is the open circuit voltage and after this voltage, there is an exponential increase in current.

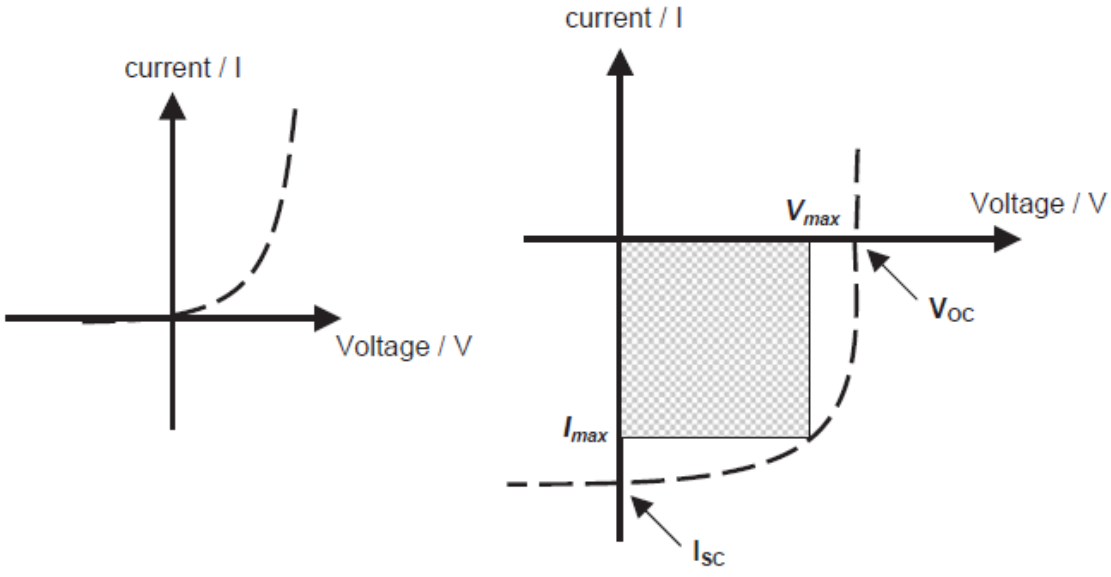

Figure 2.6 Typical I–V curves of an organic PV cell under dark (left) and illuminated (right) conditions. The open- circuit voltage (V_{oc}) and the short-circuit current (I_{sc}) are shown. The maximum output is given by the square I_{max}* V_{max}.

- Fill Factor [FF]: FF is the measure of the quality of power extraction of solar cells. I_{max} and V_{max} are the current and voltage values at which the device has maximum power output (P_{max}). P_{max} is given by the product of I_{max} and V_{max} and is the area of smaller shaded rectangle in Figure 2.6. FF is defined as the ratio of maximum power to the theoretical power (P_T). P_T is theoretical power output and is given by the product of V_{oc} and I_{sc}. This quantity has no dimensions and is wavelength dependent. It is defined through,

$$FF = \frac{P_{\max}(\lambda)}{P_T(\lambda)} = \frac{V_{\max} * I_{\max}}{V_{OC} * I_{SC}} \quad .$$

- Efficiency [η]: The power conversion efficiency (η) is the ratio of the electrical power output P_{out} to the solar power input P_{in}. P_{out} can be taken to be P_{MAX} since the solar cell can be operated up to its maximum power output to get the maximum efficiency. It is dimensionless quantity, is wavelength dependent and is defined by.

$$\eta = \frac{P_{out}}{P_{in}} \Rightarrow \eta_{\max} = \frac{P_{\max}}{P_{source}(\lambda)} = \frac{V_{\max} * I_{\max}}{P_{source}(\lambda)} = \frac{FF * V_{OC} * I_{SC}}{P_{source}(\lambda)} \quad .$$

- Series Resistance [R_S]: The series resistance in solar cells is due to the finite conductivity of the semiconducting material, the contact resistance between the semiconductor and adjacent electrodes and the resistance associated with electrodes and interconnections. R_S should be as small as possible. R_S can be deduced from the inverse slope of I-V curve at voltage greater than V_{oc}. That is

$$R_S \approx \left(\frac{I}{V}\right)^{-1} \qquad \text{For } V > V_{OC} \quad .$$

- Shunt Resistance [R_{Sh}]: The shunt resistance takes into account the loss of carriers via leakage paths as well as pinholes in the film, and also the recombination and trapping of the carriers during the transport in the cell. Ideally, R_{Sh} should be infinite. R_{Sh} can be derived by taking the inverse slope of I-V curve around 0 volts external bias,

$$R_{sh} \approx \left(\frac{I}{V}\right)^{-1} \qquad \text{At V = 0 volts.}$$

2.6.2 Equivalent Circuit Diagram

The equivalent circuit diagram (ECD) is used to describe the electrical circuit elements in a system. It makes the study of different individual parameters affecting the whole system much easier. Figure 2.7 shows the ECD for an ideal solar cell where none of the loss mechanism has been taken into account. The various components can be described as follows.

• The current source G generates a current I_G. This is the output current as a result of the dissociation of excitons into electrons and holes after photon absorption. I_G depends on the efficiency of creation of separated charge carriers.

• The shunt resistor R_{Sh} represents the current lost due to the recombination of electrons and holes near the exciton dissociation site before significant charge transport through the bulk has occurred. R_{Sh} can be derived by taking the inverse of the slope around 0 Volts. At very low

voltage, as the diode is not conducting, the current driven by external voltage is determined by (R_{Sh}+ R_S) with R_{Sh} being dominant.

• The series resistor R_S takes into account the mobility of charge carriers in the bulk of the solar cell. The mobility will be influenced by defects and barriers as well as space charges in the device. R_S will also increase with thickness of the device since the distance that the charges have to travel to the collecting electrodes increases. R_S can be deduced from the inverse slope at voltage greater than V_{oc} as at the higher positive external voltage, the diode D becomes much conducting than R_{Sh} so that R_S is dominant.

• The diode D describes the asymmetric conductivity in the solar cell. In organic cells, it can be due to a blocking contact at the semiconductor/electrode interface or a built-in field resulting from a donor-acceptor interface. I_D is the current through the diode. It is negligible under reverse bias conditions.

• The resistor R_L results when the solar cell is contacted to an external load.

An external voltage is applied to the solar cell to obtain the current voltage characteristics. For an ideal solar cell, R_{Sh} would be infinitely large and R_S would be zero. Typical values for inorganic cells are R_{Sh} larger than 1000 Ohms and a few Ohms for R_S. These values can be significantly different in organic devices since the mobility is usually lower (increasing R_S) and charge recombination can be an issue (lowering R_{Sh}).

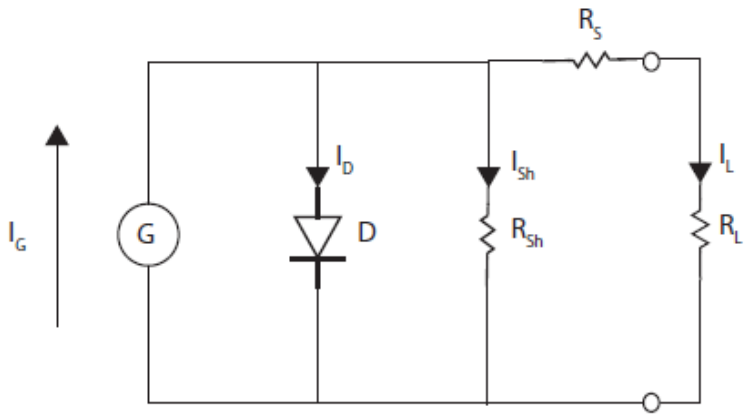

Figure 2.7 Equivalent circuit diagram of an ideal solar cell.

The ECD of an ideal solar cell does not include the different loss mechanisms which are present in real solar cell devices. Figure 2.8 shows the ECD of a real solar cell. Here, the additional components are:

• A diode D_2 that takes into account a possible blocking contact at the electrode. This blocking contact which is often formed at the electrode semiconductor interface provides an addition rectifying barrier which can influence the extraction of holes at the ITO interface.

• A second shunt resistor R_{Sh2} that directly connects the electrodes. This shunt resistor accounts for possible recombination of charges at the extracting electrodes. In addition, this shunt resistor can result from direct conducting pathways between the electrodes, for example due to shorts/pinholes in the film. When R_S is much smaller than either of the two shunt resistors, a splitting of the shunt resistance into R_{Sh} and R_{Sh2} is not necessary and both loss mechanisms can be represented by R_{Sh}.

• The capacitance is contributed the trapped charges and these space charges create a field that hinders the transport of free charges. The space charges are distributed over the area of the device, which is much larger than the thickness and hence can become important factor that affects the device performance. [C =εA/d]

This ECD can be used to interpret I-V curves measured for a photovoltaic device. The observed shape can be related to certain components of the ECD, and from that conclusions can be drawn about the physical properties of the solar cell.

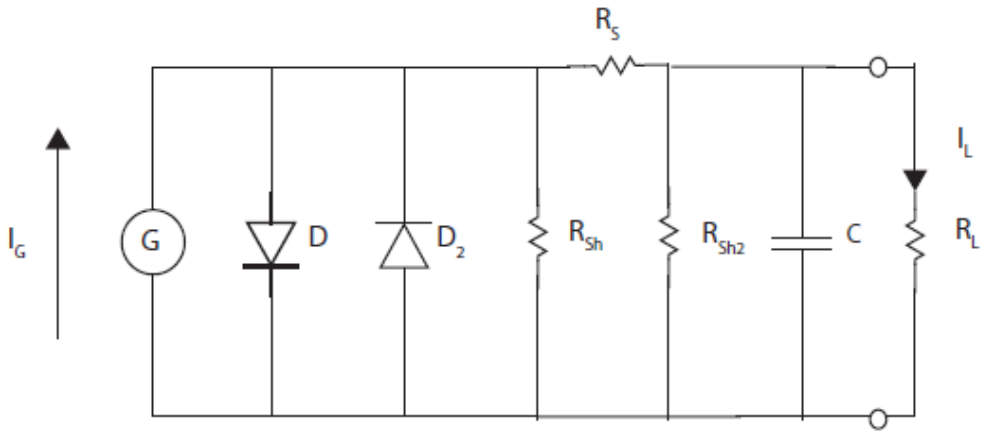

Figure 2.8 Equivalent circuit diagram of a real solar cell.

2.6.3 I-V Characteristic Study from ECD Diagrams

I-V characteristics can be studied with respect to the ECD shown in Figure 2.8. When a voltage is applied across the device, the current through D and R_L is affected by series resistance (R_S) in series and all the other loss mechanism shunt resistance (R_{SH}) present. The shape of I-V curves can reveal details about the different undesirable mechanisms present in the solar cell. In the following section, different examples of the detrimental mechanisms and how they affect the I-V curves is given.

A. High Series Resistance

In the ECD, as the series resistance, R_S, is increased, less current is drawn in the circuit and hence the output current is lesser. In this thesis, R_S values are calculated from the dark I-V curve. Figure 2.9 shows the effect of change of R_S on the I-V curves. I_{SC} and FF decreases with the increase in the value of R_S. The V_{oc} is more or less unaffected since it is measured when the current in the circuit is zero. Increased R_S indicates a drop in charge carrier mobilities and hence the photocurrents. The 4^{th} quadrant I-V curves change shape from solid to dash to dot with the increase in R_S.

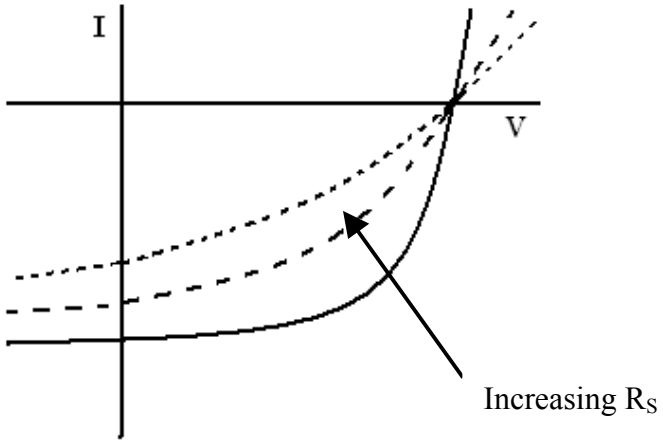

Figure 2.9 shows the effect of change of series resistance on 4th quadrant I-V curves. Arrow points towards the increase in series resistance.

B. Low Shunt Resistance

Figure 2.10 shows the effect of R_{Sh} on the I-V curve. The value of the R_{Sh} can be found from I-V curves. In this thesis, dark I-V curves are used to evaluate the value of shunt resistance. It has been found that as the value of R_{Sh} decreases, there is a drop in the V_{oc} and FF of the device. There are different sources of shunt resistance, however they all affect the I-V curves in a similar way. The I-V curve becomes more ohmic as the shunt resistance decreases. In the limit of very small $R_{Sh,}$ V_{oc} will approach zero and the FF will go to its theoretical limit (0.25). Figure 2.10 shows a sketch of I-V curves as a function of R_{Sh}, the curves get progressively more linear (solid to dashed to dotted) as the shunt resistances decrease. The short circuit current (I_{sc}) however stays almost constant with the change in shunt resistance as it is measured under no voltage and is affected mainly by the R_S. In ideal conditions, R_{Sh} should be as large as possible.

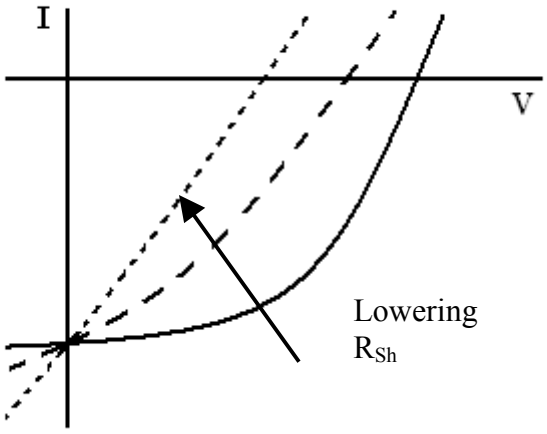

Figure 2.10 shows the effect of change in shunt resistance on I-V curves. The arrows points toward the decrease in shunt resistance.

C. Illumination Intensity Dependence

With the decrease in the intensity of illumination, the number of charge carriers that are photogenerated will also decrease (I_G). This will decrease the I_{sc}. Riedel *et al*. showed a linear dependence of I_{sc} on the intensity of illumination [41]. Figure 2.11 shows the effect on 4th quadrant I-V curves as a function of intensity of illumination. The shape of the I-V curves changes from solid to dotted line with a of decrease of the intensity of illumination which also depicts that there will be decrease in V_{oc} and FF values too. Hence it is imperative to quote the light intensity when publishing data on the efficiency of solar cells.

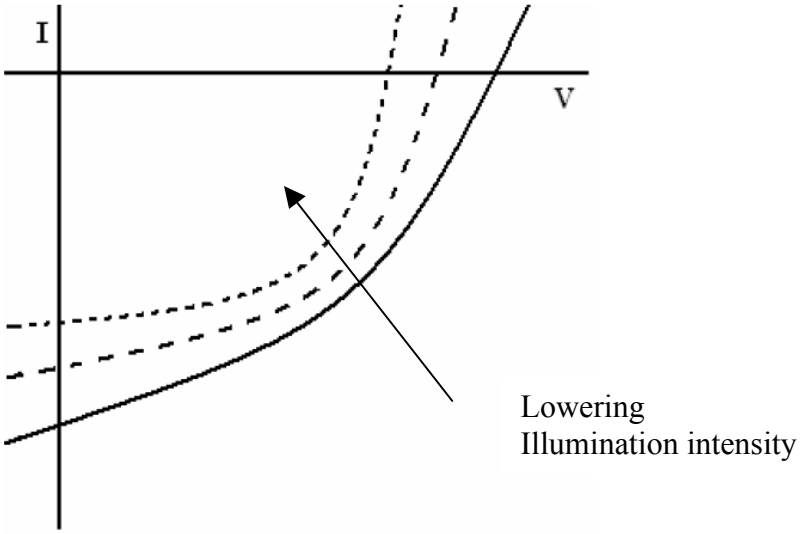

Figure 2.11 Effect of change in intensity of illumination on the 4th quadrant I-V curves. The arrows points toward the decrease in illumination intensity.

2.7 Heat Treatment of Conducting Polymers

Heat treatment of polymer solar cell devices is done both for annealing the polymer as well as for interdiffusing the bilayer.

Annealing: Conducting polymers are annealed by heating the polymer film at elevated temperature. This helps in removing the residual water and other solvents as well as in increasing the crystallinity of the polymer.

Interdiffusion: In bilayer devices, increase of interfacial area is achieved by heating the bilayer device. Interdiffusion of the bilayer device is achieved by heating the device in the vicinity or

above the glass transition of the polymer under controlled heating conditions. Two different conditions were used for heating the device.

- The sample was placed on a hot plate under the continuous flow of argon so that oxygen is prevented from entering the system.
- The sample was heated on a hot plate under vacuum.

In the following discussion, topics related to interdiffusion such as heat and mass transfer are discussed.

2.7.1 Heat Transfer

It is the thermal energy that is transferred between the hot and cold body due to spatial temperature difference. Heat can be transferred by the process of conduction, convection or radiation. As radiation can be neglected for the hot plate setup used in this process, conduction and convection will be discussed here.

A. Conduction

It refers to the heat transfer that occurs across the medium due to the presence of a thermal gradient. Heat transfer occurs from higher temperatures to lower as the molecular energy is higher for molecules associated with the higher temperature medium and as neighboring molecules collide, there is a heat transfer from the high energetic to less energetic molecules. In this process, net transfer of energy is caused by random molecular motion, and can also be described as diffusion of energy. The energy of heat transfer can be described in terms of heat flow rate (H) [33].

Heat flow rate for conduction is given by Fourier's law. For a one dimensional plane wall, which is a valid assumption for the heating setup used in this experiment, heat flow rate through a unit area is directly proportional to the temperature gradient. The heat flow rate H is given by,

$$H = \frac{dQ}{dt} = \frac{kA(T_1 - T_2)}{L} \quad .$$

Here, k is thermal conductivity (W/m*K) and is characteristic of the wall material and L is the thickness.

B. Convection

Convection is a heat transfer process in which heat transfer occurs by random molecular motion as well as by macroscopic motion of the bulk. As the bulk must be able to move, convection is only possible in the case of fluids.

A specific case of study is the interface between the solid surface and the fluid in motion where the two are at different temperatures. As a result of surface –fluid interaction, the velocity of the fluid varies from zero at the interface to some finite value away from the interface. Heat transfer at the interface is mainly due to random molecular motion at the interface where the fluid velocity is zero. Heat transfer is sustained by both random molecular motions as well as by bulk motion of the fluid at any point away from the interface. In convection mode, the heat transfer rate is proportional to the temperature difference between two phases as well to the surface area of contact [33, 34] where,

$$H = \frac{dQ}{dt} = h * A * (T_s - T_f) \quad .$$

Here, h (W/m^2*K) is the convection heat transfer coefficient and T_s and T_f are the surface and fluid temperatures, respectively. In this experimental setup, conduction and convection are mainly responsible for heat transfer between the hot plate and the sample device.

C. Temperature at the Surface of Film

The temperature at the surface of the film that is heat treated can be modeled in terms of heat transfer through a single wall. Figure 2.12 shows the schematic of the setup used for heat treatment of the devices. In this setup, thermal contact resistance, which is due to the surface roughness of either of the two surfaces in contact, is considered negligible. The film is heated by the process of conduction through the glass slide and the process of convection dictates the heat transfer from the film into the atmosphere.

The heat transfer rate into the film is given by,

$$H_{in} = \frac{dQ_{in}}{dt} = \frac{k_{glass} A(T_{hp} - T_{film})}{L_{glass}} \quad .$$

The heat transfer out of the film is given by the process of convection and is given by,

$$H_{out} = \frac{dQ_{out}}{dt} = h * A * (T_{film} - T_{gas}) \quad .$$

In the state of equilibrium, the rate of heat transfer into the film should be equal to the rate of heat transfer out of the film. Solving for T_{film} under the state of equilibrium gives:

$$H_{in} = H_{out}$$

and,

$$T_{film} = \frac{k_{glass} T_{hp} + h * L_{glass} * T_{gas}}{k_{glass} + h * L_{glass}} \quad .$$

Hence T_{film} can be evaluated using the above equation.

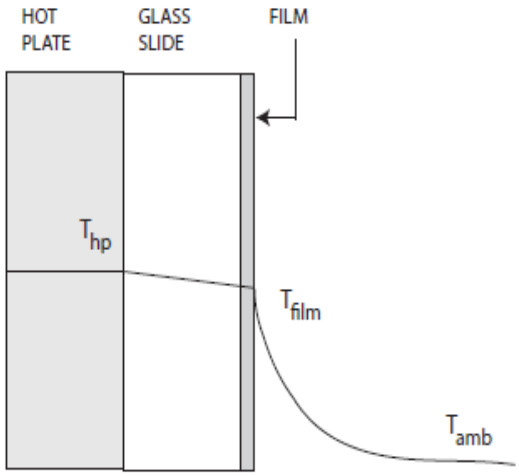

Figure 2.12 Heat treatment setup for a device on a hot plate.

2.7.2 Mass Transfer

During the process of heat transfer, mass transfer also can occur. Mass transfer results due to the concentration gradient in materials. Mass transfer is the process of diffusion of one species into another as a result of that concentration gradient. In polymeric solar cells based on the bilayer architecture, upon heat treatment of the devices, there is diffusion, which can be explained by Fick's law of diffusion [35].

The rate equation, for the mass diffusion of species A is given by Fick's Law,

$$J_A = -C * D_{AB} * \nabla f_A \quad . \quad [1]$$

Here, J_A(Kmol/m^2s) is the molar flux of species A, C ($C = C_A+C_B$) is the total molar concentration, D_{AB} is the binary diffusion coefficient and f_A is the mole fraction of species A(f_A

$=C_A/C$). For the case of the bilayer system, the following assumptions are assumed in order to simplify the process:

- There is no chemical reaction involved in this process and hence there is conservation of species.
- The diffusion of species is one directional.
- Diffusion coefficients are considered constant as the diffusion occurs at constant temperature.
- Here species A is assumed to move into species B and hence B is considered stationary medium and the A-B interface does not move.

As this process is concentration gradient dependent, the molar flux at any point is dependent on the concentration in a small distance dx.

$$J_{A,x+dx} - J_{A,x} = \frac{\partial J_{A,x}}{\partial x} * dx \qquad [2]$$

As there has to be conservation of species, the amount of material flowing into a region should equal the combination of the material flowing out and the material stored, so that,

$$\frac{dM_{A,in}}{dt} - \frac{dM_{A,out}}{dt} = \frac{dM_{A,stored}}{dt} \quad . \qquad [3]$$

The rate at which mass is stored can also be expressed as,

$$\frac{dM_{A,stored}}{dt} = \frac{dC}{dt} * dx \quad . \qquad [4]$$

Comparing equations 2 and 3,

$$-\frac{dJ_{A,x}}{dx} = \frac{dC}{dt} \qquad [5]$$

Equation 5 can be modified further using equation 1 to obtain

$$-\frac{d(-C * D_{AB} * \nabla f)}{dx} = \frac{dC}{dt} \quad . \qquad [6]$$

Assuming C and D_{AB} as constants, it can be simplified further to

$$D_{AB}\frac{d^2C_A}{dx^2} = \frac{dC_A}{dt} \quad .$$

This equation can be solved with the assumption of certain boundary conditions. Here in this situation, the following boundary conditions are assumed.

The initial concentration of species A in the bulk of region B is zero,

$$C_A(x,0) = 0 \quad .$$

As specified in the assumptions, pure A can be found at the interface, x = 0, at any time t. At x = 0, C_A is maximum. This yields,

$$C_A(x,t) = C_{\max}[1 - erf(\,x \big/ \sqrt{4 * D_{AB} * t}\,)] \quad .$$

This model is useful for getting a feel of the interdiffusion process. But this theory, as is, is an over simplification that cannot be used directly to model the interdiffusion process of our system.

2.8 Origin of the Open Circuit Voltage (V_{oc})

The origin of the open circuit voltage in organic solar cells has been a subject of great debate in the recent past. In general, it has been found that V_{oc} is related to the built-in potential

of the photovoltaic device. The built-in potential strongly depends on the morphology of the active layer and is different for varied device architectures. In single layer devices, the built-in potential is determined by the difference in work functions of the two metal contacts. In bilayer/bulk organic solar devices, V_{oc} is dependent on the difference of the highest occupied molecular orbital HOMO level of the donor and the lowest unoccupied molecular orbital LUMO level of the acceptor. The various parameters that affect the V_{oc} are the LUMO level of acceptor (first reduction potential), the HOMO level of the donor (oxidation potential) and the work function of the top electrode material. However, it has been found that effect of the variation of work function of top electrode material on the V_{oc} is quite insignificant.

A. Electron acceptor

Brabec *et al*. studied the correlation of the LUMO level of acceptor and the observed V_{oc} of the devices [36]. Figure 2.13 shows the effect of the variation of different derivatives of fullerene C_{60} on the observed open circuit potential of devices.

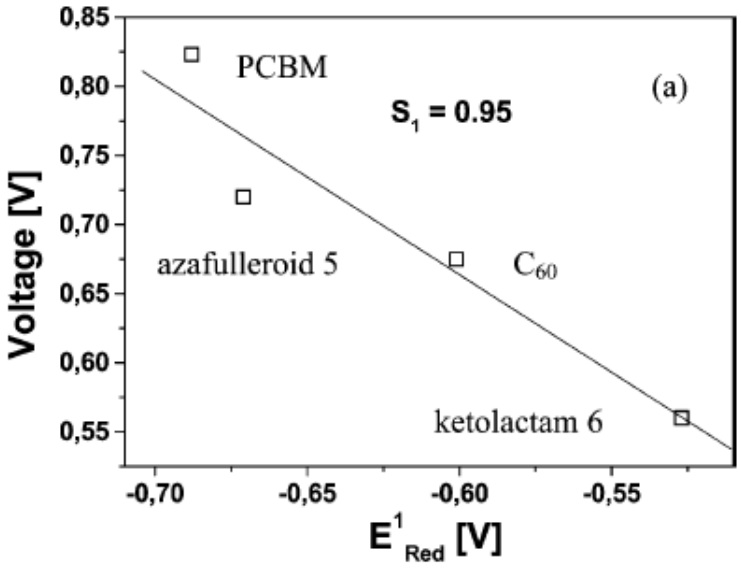

Figure 2.13 Dependence of V_{oc} on the LUMO levels of various fullerene derivatives.

B. Electrode Material

PCBM was chosen as the reference electron acceptor in order to study the influence of the work function of the top electrode material on the built-in potential of the organic solar cells. Figure 2.14 shows the plot of the variation of the V_{oc} as a function of the work function of the top electrodes. A variation of less than 200 mV was observed in V_{oc} when the work function of electrode material is varied by 2.2 Volts. Hence the effect of the change of work function on the open circuit voltage is quite insignificant.

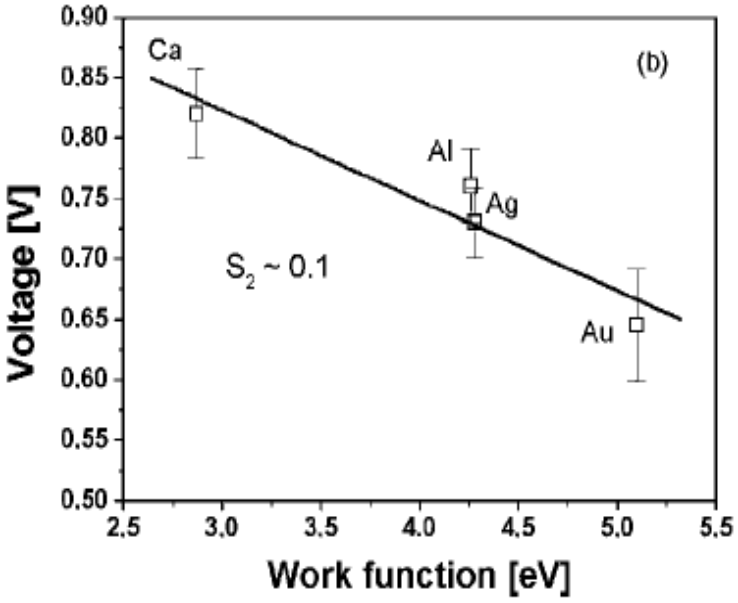

Figure 2.14 Dependence of V_{oc} on the work function of the various top electrodes.

C. HOMO Level of Polymer

Gadisa *et al*. studied the correlation in the V_{oc} as a function of the variation of the HOMO level (first oxidation potential) of the donor conjugated polymer [37, 38]. Scharber *et al*. reported for 26 different bulk heterojunction solar cells that there is a linear relation between the oxidation potential (HOMO level) of the conjugated polymer and the V_{oc} [38].

Hence V_{oc} can be defined as a function of the HOMO level of the polymer donor and the LUMO level of the fullerene acceptor and can be described as,

$$V_{OC} = (A_{OX} - S_1 E_{red(A)}) - S_2(\phi_M - E_{red(A)}) \quad .$$

Here, $E_{red(A)}$ is the reduction potential or LUMO level of the acceptor (fullerene derivative), A_{OX} is a constant which is a function of oxidation potential or HOMO level of conjugated polymer and Φ_M is the work function of the metal. S_1 and S_2 are the slopes calculated from the Figure 2.13 and Figure 2.14. As S_2 is a small parameter, it can be neglected.

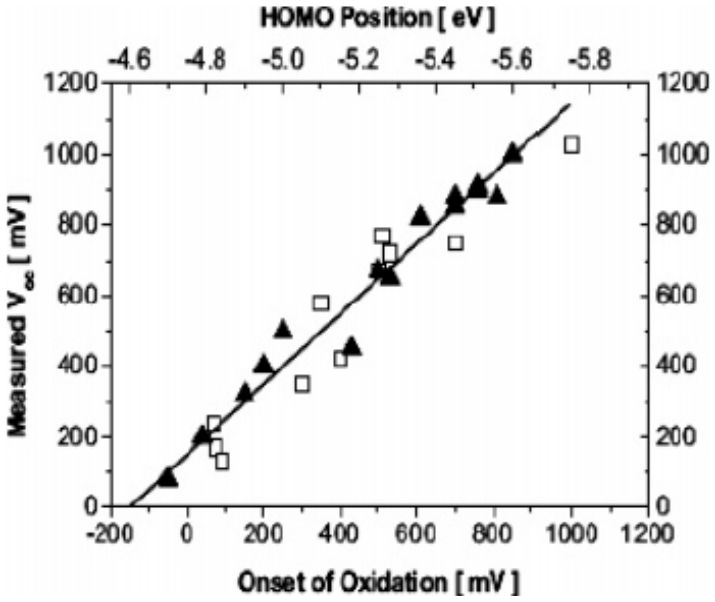

Figure 2.15 Dependence of V_{oc} on HOMO level of the polymer donor as reported by Scharber *et al*.

Hence V_{oc} can be defined as,

$$V_{OC} = ((A_{OX} - S_1 E_{red(A)}) - 0.3V \quad .$$

Here, 0.3 Volts is the empirical parameter which can be related to the difference between the LUMO of the donor and the LUMO of the acceptor, the potential difference which is sufficient for efficient charge separation. Hence V_{oc} of polymer solar cells can be controlled by the appropriate choice of the donor and acceptor materials.

Further, Vandewal *et al*. [40] reported that V_{oc} can be correlated to the formation of charge transfer complex (CTC) between the polymer and the fullerene. The presence of a weak emission signal, which is red-shifted compared to the pure components, was detected in the photoluminescence and electroluminescence spectra and was assigned to the emission of interface electron-hole pairs or charge-transfer excitons. This can also be characterized by the presence of a weak sub-gap absorption band in several polymer fullerene blends used for photovoltaics which are required for the formation of a CTC. The injected current in an organic solar cell is given by the ideal diode equation,

$$J_{IN}(V) = J_0(\exp(\frac{qV}{kT}) - 1) \quad . \quad (1)$$

At open circuit, the injected current $J_{IN}(V)$ causing the low quantum efficiency charge-transfer emission equals J_{sc}; hence, from equation (1), we obtain a commonly used equation for V_{oc},

$$V_{OC} = \frac{kT}{q}\ln(\frac{J_{SC}}{J_O} + 1) \quad . \quad (2)$$

This formula for V_{oc} does not contain a parameter related explicitly to any optical gap. However, both J_o and J_{sc} are a function of the spectral band positions and it is implicitly integrated in their formula. V_{oc} values obtained by this formula have been found quite close to the experimental values obtained for different preparation techniques as well as for different materials. These differences can be related to the change in the spectral position of charge transfer complexes for different parameters.

Based on these studies, it has been found that the efficiency of bulk heterojunctions is primarily dependent on the bandgap and the LUMO level of the donor [39, 40]. Figure 2.16 shows the contour plot of the power conversion efficiency where, the x and y axes are band gap and LUMO level of the donor, respectively. The straight lines in Figure 2.16 define lines of constant donor HOMO levels of –5.7 and –4.8 eV. The following assumptions are assumed while making this plot.

- The external quantum efficiency (*EQE*) of the solar cell for photon energies equal to or larger than the bandgap energy of the donor and the *FF* are each set to 65 %.
- Any contribution to the short-circuit current from photons absorbed by the fullerene is neglected.
- It is assumed that an energy difference of 0.3 eV between the LUMO of the donor and LUMO of the acceptor is sufficient for efficient charge separation.

It is evident from Figure 2.16 that the energy conversion efficiency of a bulk-heterojunction solar cell should be much more sensitive to changes of the donor LUMO level compared to variations of the donor bandgap. It is evident that a variation of the donor bandgap by 0.65 eV leads to a variation of only 1% in the device efficiency. In contrast, a 0.65 eV

variation of the polymer LUMO level results in efficiency changes between 3.5% and 8% depending on the donor bandgap. In order to achieve efficiency greater than 10 %, the donor polymer must have a bandgap of less than 1.74 eV and a LUMO level of less than –3.92 eV. These results indicate that besides reducing the band gap, new materials needs to be designed in order to optimize the LUMO level of the donor.

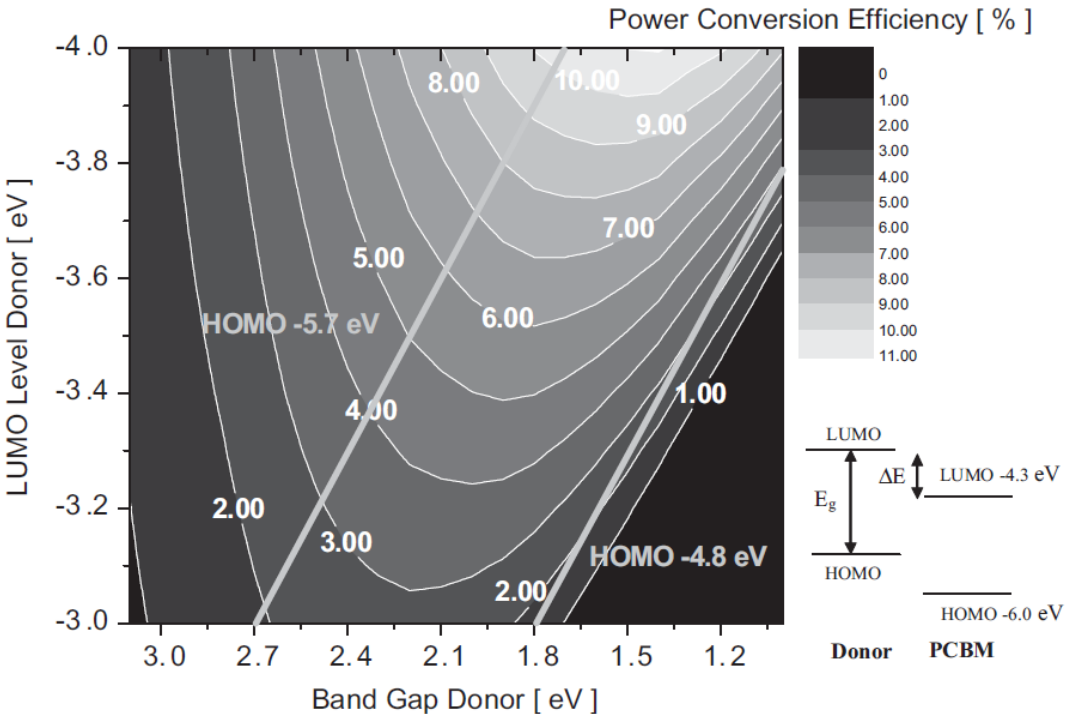

Figure 2.16 Dependence of the power conversion efficiency as a function of the LUMO level and band gap of the donor.

Hence, although an optimized open-circuit voltage is a prerequisite to achieve certain device efficiencies; it is not sufficient.

References

1. H. Shirakawa, E.J. Louis, A.G. Macdiarmid, C.K. Chiang, A.J. Heeger, "Synthesis of Electrically Conducting Organic Polymers: Halogen Derivatives of Polyacetylene", **Chem Communications**, 578, (1977).

2. H.Spanggaard, F.C. Krebs, "A Brief History of the Development of Organic and Polymeric Photovoltaics", **Solar Energy Materials and Solar cells**, 83, 125-146, (2004).

3. T.L Benanti, D.Venkataraman, "Organic Solar Cells: An Overview Focusing on Active Layer Morphology", **Solar Cells**, 73-81, (2006).

4. H. Shirakawa, *et al*., "Synthesis of Electrically Conducting Organic Polymers: Halogen Derivatives of Polyacetylene", **J. Chem. Soc., Chem. Commun.**, 578-580, (1977).

5. S. Glenis, G. Horowitz, G. Tourillon, F. Garner, "Electrochemically Grown Polythiophene and Poly(3-methylthiophene) Organic Photovoltaic Cells" **Thin Solid Films,** 111, 93-103, (1984).

6. J.H. Burroughes, *et al*., "Light-Emitting Diodes Based on Conjugated Polymers" **Nature** 347, 539-541, (1990).

7. Y. Cao, P. Smith, A.J. Heeger, "Counter-Ion Induced Processibility of Conducting Polyaniline and of Conducting Polyblends of Polyaniline in Bulk Polymers", **Synth. Met.** 48, 91-97, (1992).

8. C. Brabec, V. Dyakonov, J. Parisi, N. S. Sariciftci (Eds.), "Organic Photovoltiacs, Concepts and Realization", Springer Series in Material Science, Vol 60, Springer-Berlin, Heidelberg, (2003).

9. http://cnx.org/content/m25670/latest/

10. W. R. Salaneck, R. H. Friend, and J. L. Brédas, "Electronic structure of conjugated polymers: consequences of electron–lattice coupling**", Phys. Rep. -Rev. Sec. Phys. Lett.** 319, 231-251, (1999).

11. J.L. Brédas, G. B. Street, "Polarons, Bipolarons and Solitons in Conducting Polymers", **Acc. Chem. Res.**18, 309-315, (1985).

12. N.S. Sariciftci, L. Smilowitz, A.J. Heeger, F. Wudl, " Photoinduced Electron Transfer from a Conducting Polymer to Buckminsterfullerene", **Science,** 258, 1474-1476, (1992).

13. D. Vacar, E. S. Maniloff, D. W. McBranch, A. J. Heeger, "Charge-transfer range for photoexcitations in conjugated polymer/fullerene bilayers and blends", **Phys. Rev. B**, 56(8), 4573-4577, (1997).

14. B. Kraabel, *et al*., "Ultrafast spectroscopic studies of photoinduced electron transfer from semiconducting polymers to C_{60}", Phys. Rev. B, 50 (24), 18543-18552, (1994).

15. J.J.M. Halls *et al*., «Exciton diffusion and dissociation in a poly(p - phenylenevinylene)/C_{60} heterojunction photovoltaic cell, **Appl. Phys. Lett.** 68(22), 3120-3122, (1996).

16. J.L. Brédas, J.P. Calbert, D.A. da Silva Filho, J. Cornil, "Organic semiconductors: A theoretical characterization of the basic parameters governing charge transport", **PNAS** 99(9), 5804-5809, (2002).

17. B.H. Cumpton, K.F. Jensen, "Photo-oxidation of Polymers Used in Electroluminescent Devices", **Synth.Met.** 73, 195-199, (1995).

18. S. Holdcroft, "A photochemical study of poly(3-hexylthiophene)", **Macromolecules** 24, 4834-4838, (1991).

19. A. K. Ghosh and T. Feng, "Merocynanine organic solar cells", **J. Appl. Phys.** 49, 5982, (1978).

20. R.N. Marks, J.J.M. Halls, D.D.C. Bradley, R.H. Friend, and A.B. Holmes, " The photovoltaic response in poly(p-phenylene vinylene) thin-film devices", **J. Phys.: Condens. Matter.**, 6, 1379, (1994).

21. N.S. Sariciftci, L. Smilowitz, A.J. Heeger, and F. Wudl, "Photoinduced Electron Transfer from a Conducting Polymer to Buckminsterfullerene", **Science** 258, 1474, 1992.

22. C.W. Tang *et al.*, "Two-Layer Organic Photovoltaic Cell", **Appl. Phys. Lett.** 48, 183, (1986).

23. Sariciftci, N. D.; Braun, D.; Zhang, C.; Srdanov, V. I.; Heeger, A. J.; Stucky, G.; Wudl, F., Semiconducting polymer buckminsterfullerene heterojunctions: Diodes, photodiodes, and photovoltaic cells, **Appl. Phys. Lett.**, 62, 585, (1993).

24. G. Yu, J. Gao, J.C. Hummelen, F. Wudl, A.J. Heeger, "Polymer Photovoltaic Cells: Enhanced Efficiencies via a Network of Internal Donor-Acceptor Heterojunctions", **Science**, 1995, 270, 1789.

25. S.E. Shaheen, C.J. Brabec, N. S. Sariciftci, F. Padinger, T. Fromherz, C. J. Hummelen, "2.5% Efficient Organic Plastic Solar Cells", **Appl. Phys. Lett.**, 78, 841, (2001).

26. F. Padinger, R. S. Rittberger, N. S. Sariciftci, "Effects of Postproduction Treatment on Plastic Solar Cells", **Adv. Funct. Mater.**, 13, 85, (2003).

27. W. Ma, C. Yang, X. Gong, K. Lee, A. J. Heeger, "Thermally Stable, Efficient Polymer Solar Cells with Nanoscale Control of the Interpenetrating Network Morphology", **Adv. Funct. Mater.**, 15, 1617 – 1622, (2005).

28. G. Li, V. Shrotriya, J. Huang, Y. Yao, T. Moriarty, K. Emery, Y. Yang, "Investigation of annealing effects and film thickness dependence of polymer solar cells based on poly „ 3-hexylthiophene", **Nat. Mater.** 4, 864 – 868, (2005).

29. Y. Liang, Z. Xu, J. Xia, S.Tsai, Y Wu, G. Li, C.Ray, L.Yu, "For the Bright Future — Bulk Heterojunction Polymer Solar Cells with Power Conversion Efficiency of 7.4%", **Adv. Mat**, 22, E135-E138, (2010).

30. M. Granstrom, K. Petritsch, A.C. Arias, A. Lux, M.R. Andersson, and R.H. Friend, "Laminated fabrication of polymeric photovoltaic diodes"**Nature** 395, 257, (1998).

31. M. Kaur, A.Gopal, R.M.Davis, J.R.Heflin, "Concentration Gradient P3OT/PCBM Photovoltaic Devices Fabricated by Thermal Interdiffusion of Separately Spin-Cast Organic Layers", **Solar Energy Materials & Solar Cells**, 93, 1779–1784, (2009).

32. Wang, D. H., Lee, H. K., Choi, D.-G., Park, J. H., & Park, O. Ok, "Solution-processable polymer solar cells from a poly 3-hexylthiophene/ 6 , 6 -phenyl C_{61} -butyric acidmethyl ester concentration graded bilayers, **Applied Physics Letters**, 95(4), 043505, (2009).

33. F.P.Incropera, D.P.Dewitt, T.L. Bergman, A.S. Lavine, "Introduction to heat transfer," John Wiley& Sons, New York, (1981).

34. F.P. Incropera, D.P. De Witt, "Fundamentals of Heat Transfer," John Wiley& Sons, New York (2007).

35. W.R. Veith, "Diffusion In and Through Polymers – Principles and Applications," Oxford Univeristy Press, (1991).

36. C. J. Brabec, A. Cravino, D. Meissner, N.S. Sariciftci, T. Fromherz, M. T. Rispens, L. Sanchez, and J. C. Hummelen, "Origin of the Open Circuit Voltage of Plastic Solar Cells", **Adv. Funct. Mater.**, 11(5), 374-80, (2001).

37. S. Günes, H. Neugebauer, and N.S. Sariciftci, "Conjugated Polymer-Based Organic Solar Cells", **Chemical reviews**, 107(4), 1324-1338, (2007).

38. A. Gadisa, M. Svensson, M. R. Andersson and O. Inganas, "Correlation Between Oxidation Potential and Open-Circuit Voltage of Composite Solar Cells Based on Blends of Polythiophenes/ Fullerene Derivative," **Applied Physics letters**, 84 (9), 1609-11, (2004).

39. M. C. Scharber, D. Mühlbacher, M. Koppe, P. Denk, C. Waldauf, A.J. Heeger, "Design Rules for Donors in Bulk-Heterojunction Solar Cells—Towards 10 % Energy-Conversion Efficiency" , **Advanced Materials**, 18(6), 789-794, (2006).
40. K. Vandewal, K. Tvingstedt, A. Gadisa, O. Inganäs and J. V. Manca," On the origin of the open-circuit voltage of polymer-fullerene solar cells", **Nature Materials**, 8, 904-09, (2009).
41. I. Riedel, *et al.*,"Effect of Temperature and Illumination on the Electrical Characteristics of Polymer–Fullerene Bulk-Heterojunction Solar Cells", **Adv. Funct. Mater**. 14(1), 38-44, (2004).

Chapter 3

Experimental Methods and Materials

This chapter explains the experimental set ups and methods used in this thesis. The materials that are used for the fabrication of photovoltaic devices in this thesis are also discussed in detail.

3.1 Experimental Setups

This section provides information on the different setups used in this experiment for the fabrication of photovoltaic devices.

3.1.1 Spin coater

A spin coater from Chemat technologies (KW-4A) is used to spin cast the films onto the indium tin oxide (ITO)-coated glass substrates. In this thesis, most of the layers in the multilayer photovoltaic device are deposited by spin casting. A few drops of the solution are dropped onto the substrate which is then spun at a particular speed. The speed can be varied from 800 rpm to 4000 rpm. As the solution is spun off from the slide, the solvent evaporates leading to a uniform film. There are two parameters that affect the thickness of the spin coated film.

- Concentration of the solution: The higher concentration of the solution leads to the thicker films. Hence by varying the concentration, the thickness can be controlled.
- Spin speed used for spin casting: The higher is the spin speed, the thinner will be the film. However, it has been found that varying the spin speed at a particular concentration does not produce a large difference in the thickness.

The poly (3,4-ethylenedioxythiophene): poly(styrenesulfonate) complex (PEDOT: PSS) layer is spin cast at 1500 rpm from an aqueous solution. The donor and acceptor layers are spin cast from volatile organic solvents such as chloroform, chlorobenzene and dichlorobenzene. Volatile organic solvents evaporate faster and hence lead to faster formation of the film. In this thesis, concentration as well as spin speed is varied to achieve varied thickness of the different layers.

3.1.2 Vacuum Evaporator

A vacuum evaporator from Ladd Inc (#30000) is used for the evaporation of electrodes. Figure 3.1 shows the schematic of the evaporator with the boat for aluminum electrode deposition. Aluminum electrodes are deposited under vacuum of the range of 4-6 μTorr. The deposition of the aluminum layer is carried out by evaporating aluminum granules (purchased from Alfa Aesar, 8-12 mm) from tungsten wire boats (purchased from R.D. Mathis Co. part #: ME17-3X.025W). This system also has a setup for heating the substrates. A thermocouple and heater interfaced with an Omega CN9000A temperature controller are connected to the stage holding the substrate, which allows for the controlled heating of the substrate under vacuum. This step is used for annealing of the donor layer prior to acceptor deposition, annealing the bulk heterojunction devices and for the interdiffusion of the bilayer devices under vacuum. The films deposited by this method are not quite uniform. The thickness is highest at the center and decreases towards the edge of the slide.

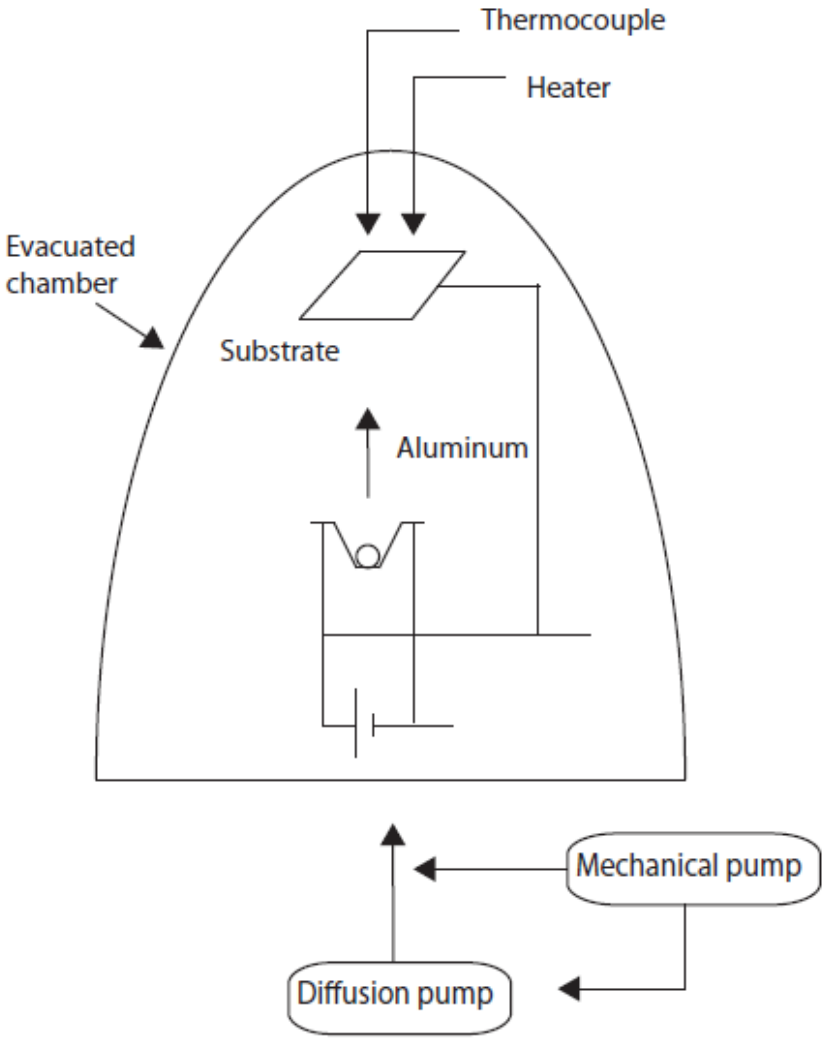

Figure 3.1 Schematic of the vacuum sublimation unit with the set up for electrode deposition.

3.1.3 Transmission-Reflection Measurements, Optical Density and Thickness

A Filmetrics F20-UV thin film spectrometer system, which can run in transmission as well as reflection mode, is used for obtaining transmission and reflection data for the devices. A Deuterium Halogen lamp source, DH2000 from Ocean Optics Inc. is used for illumination. The transmission and reflection data is used to calculate the optical density, which is directly proportional to the thickness. Hence, this method can be used for the determination of thickness. Equation [1] describes the relation of the optical density at a particular wavelength to the transmission and reflection values at that wavelength [1].

$$OD = -\log\frac{T}{1-R} \qquad [1]$$

According to Beer-Lambert's law, the transmission (T) through a film can be described in terms of the absorption coefficient of the film (α) and thickness of the film (d) by,

$$T = \frac{I}{I_0} = e^{-\alpha d} \quad . \qquad [2]$$

Here I_0 is the initial intensity of the light and I is the transmitted light intensity. Optical density (OD) defines the amount of light that is absorbed in the sample and is related to the transmission by,

$$T = 10^{-OD} \quad . \qquad [3]$$

From equation 2 and 3, the thickness of a film can be expressed in terms of the optical density and absorption coefficient by,

$$d = \frac{OD}{\alpha * \log(e)} \quad . \qquad [4]$$

Hence, the optical density values can be used to deduce the thickness of the film if the value of α is known. This is the method that is primarily used in this thesis for thickness calculation unless otherwise specified. The optical density and absorption coefficient are wavelength dependent so all values used must be at the same wavelength in order to calculate the thickness. The photovoltaic devices studied in this thesis are multilayer devices and thickness of each layer is calculated using this method. The Filmetrics is used to collect the optical density of each layer after the subsequent deposition of each layer. Figure 3.2 shows a typical plot of the additive optical densities as each layer is added onto the ITO-coated glass substrate.

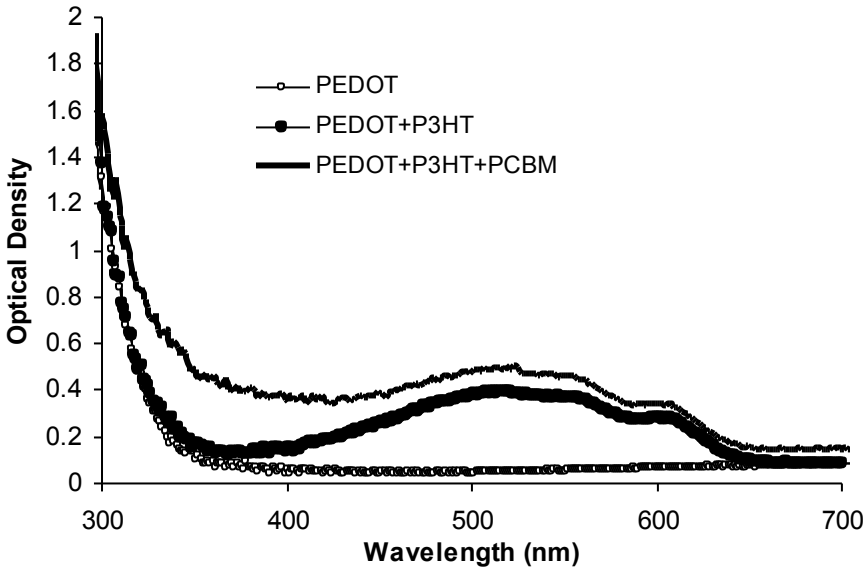

Figure 3.2 Typical plot of the additive optical densities of PEDOT, P3HT and PCBM as each layer is added to ITO coated glass substrate.

In order to calculate the thickness of each layer, it is assumed that there is no ground state interaction between the subsequent layers. Hence, the thickness of n^{th} layer can be calculated by subtracting the OD of $(n-1)^{th}$ layer from n^{th} layer. Figure 3.3 shows a example of the optical density curve of individual layers as is obtained by subtracting the OD of $(n-1)^{th}$ layer from n^{th} layer.

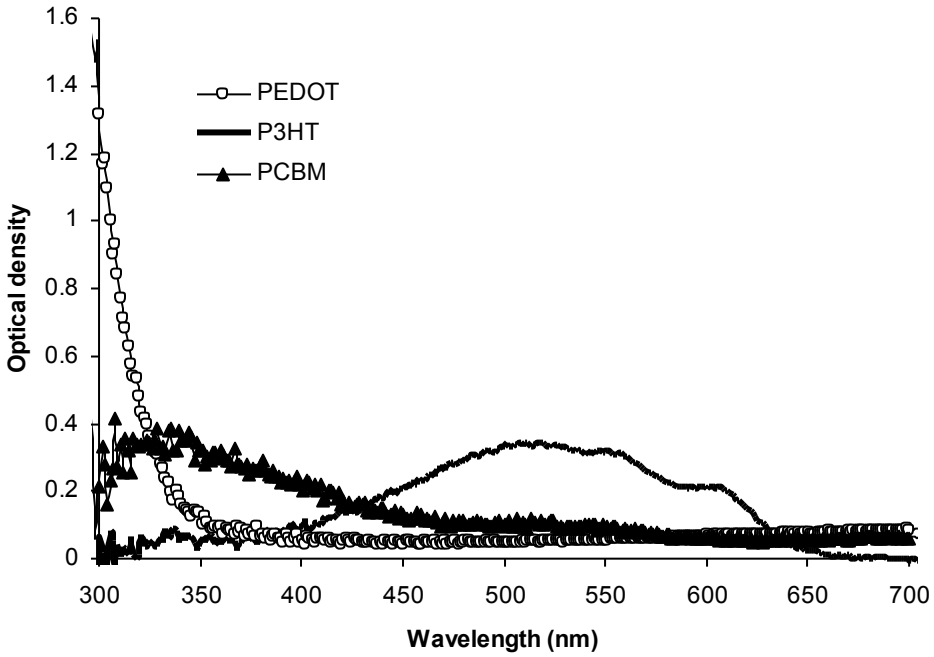

Figure 3.3 Typical plot of the separate optical densities of PEDOT, P3HT and PCBM as optical density of each subsequent layer is subtracted from the previous layers.

3.1.4 Photocurrent and I-V Curve Measurements

A. Measurements Under Monochromatic Lamp Source

The schematic of the setup used to obtain I-V curves and short circuit current is shown in Figure 3.4. A 300 W Xe lamp from Oriel Instruments, combined with a CVI CM 110 monochromator, serves as the optical source. The monochromator with 2400 grooves/mm is used to select the wavelength to be used, which is then focused on the device. A silicon photodiode from Oriel Instruments, of calibrated photoresponsivity, is used to measure lamp intensity. The diode is used to calibrate the intensity on regular basis in order to account for the changes in the power output of the light sources which can be due to wear of the cathode in the Xe lamp. The $P_{source}(\lambda)$ at each selected wavelength can be determined using the known photoresponsivity spectrum of the diode. A Keithley 485 picoammeter is used to collect the unbiased photocurrents (I_{SC}), the current measured under no external bias applied. By measuring the $P_{source}(\lambda)$ and I_{SC} at each wavelength, the photoresponsivity and EQE can be calculated by using,

$$\text{PR}= \frac{I_{sc}(\lambda)}{P_{source}(\lambda)} \quad ; \quad EQE(\lambda) = \frac{hc}{e} * \frac{PR(\lambda)}{\lambda} \quad .$$

The average intensity of the source at the sample is found to be ~4mW/cm^2 at 470 nm illumination. The current-voltage curves are measured under dark and the monochromatic illumination by using a Keithley 236 source measurement unit along with the monochromator. The source measurement unit is used to supply the varying external bias and measure the resulting currents through the device to yield I-V characteristics. The monochromator combined with the source measurement unit is used to select the wavelength at which the I-V curves are

measured. The FF values and the power conversion efficiency (η) values are calculated from this data by using,

$$\mathrm{FF} = \frac{V_{\max} * I_{\max}}{V_{OC} * I_{SC}} \quad ; \quad \eta = \frac{FF * V_{OC} * I_{SC}}{P_{source}(\lambda)} \quad .$$

All the measurements are done in the box filled with Argon in order to avoid the photo-oxidation.

B. Measurements Under AM1.5 Solar Simulator Lamp

The photocurrent and I-V measurements are also done under simulated AM1.5 solar spectrum. AM0 and AM 1.5 filters were purchased from Oriel Instruments and calibrated for a 300 W Xe lamp to produce the simulated solar spectrum. This setup is quite identical to the setup used for the monochromatic measurements; however there is no monochromator here. The schematic of the setup is identical to Figure 3.4, with the monochromator replaced by AM0 and AM1.5 filters. The filters are placed in front of the lamp to produce the solar spectrum intensity of 100 mW/cm^2, which is the intensity of one sun and it corresponds to a current of 0.118 mA in our calibration diode.

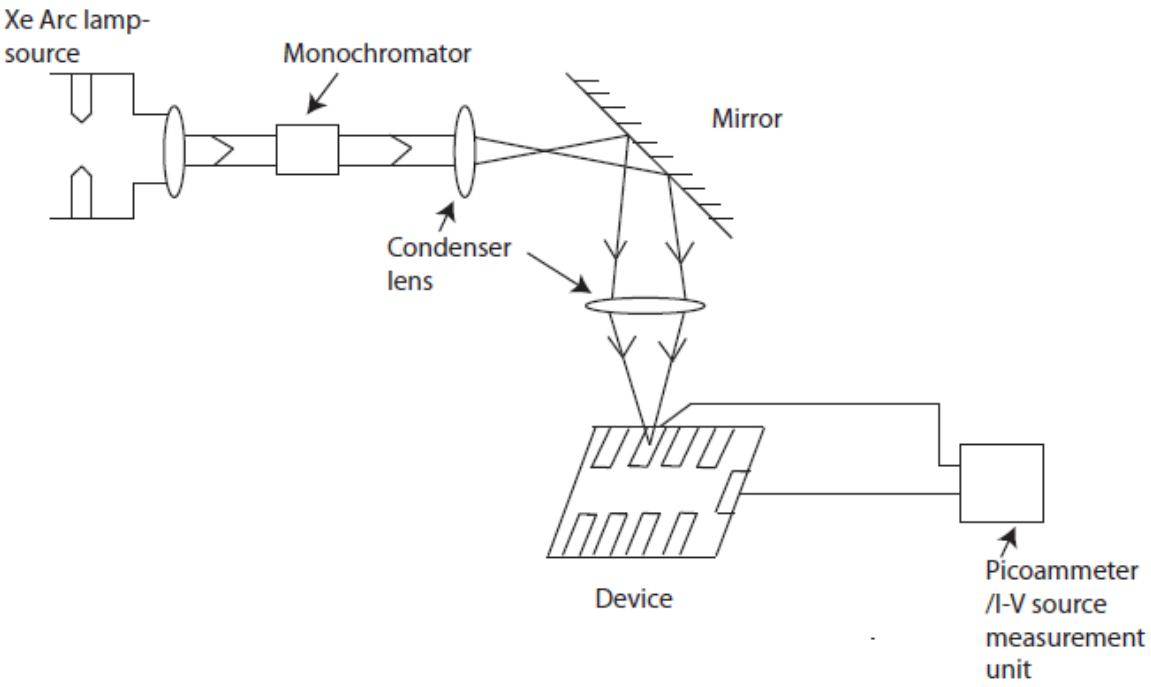

Figure 3.4 Experimental setup to obtain I-V characteristics and photocurrent measurements under monochromatic lamp.

3.1.5 Hot Stage for Heat Treatment

Two methods were used to heat the samples in this thesis. The heating of the sample at higher temperature is done to induce diffusion of donor and acceptor materials in a bilayer device. In one method, the heating is done in the vacuum chamber by using a 1" by 1" kapton heater placed in contact with the sample device. Hence, in this case, the temperature of the heater is essentially the same as that of the slide. The temperature of the heater is controlled by a CN9000A controller.

The other method involves heating the sample on a hot plate which is placed in the inert environment in the plexiglass box. The inert atmosphere is maintained by continuous flow of argon into the plexiglass box. The temperature on the hot stage is controlled by a CNi1622-C24 temperature controller by Omega Engineering Inc., enabling constant heat rates for the heating process. As the temperature controller controls the temperature of the hot plate, it is necessary to determine the temperature difference between the hot plate and the surface of the sample. As stated in section 2.7, the temperature at the surface of the sample or film is given by,

$$T_{film} = \frac{k_{glass} T_{hp} + h * L_{glass} * T_{gas}}{k_{glass} + h * L_{glass}} \quad .$$

The following parameters are assumed in the calculation of the temperature at the sample surface. Here, k_{glass} is the thermal conductivity of glass (1W/(K.m)), A is the surface area of the slide (6.25×10^{-4} m^2), T_{hp} is the hot plate temperature, T_{film} is the temperature of the film, L_{glass} is the thickness of the glass slide (9×10^{-4}m), h is the convection heat transfer coefficient (upper limit of 25K.W/m^2 for free convection) and T_{gas} is the ambient temperature (293K). T_{film} can be calculated using this formula. The plot of the temperature difference of the film with respect to temperature of the hot plate is shown in Figure 3.5. A temperature difference of 5 °C is found between the temperature of the hot plate and the film when the temperature of the hot plate is ~300 °C. This is a quite small difference and hence can be considered insignificant.

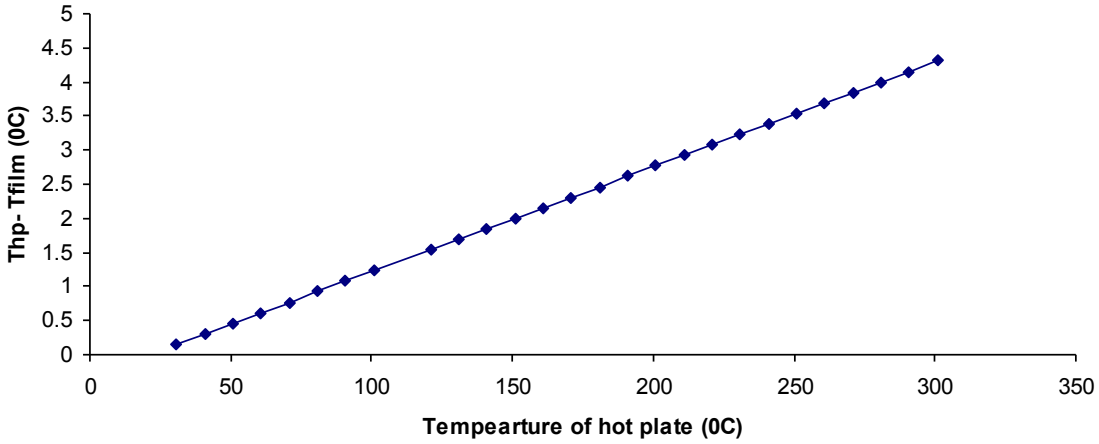

Figure 3.5 Plot of the temperature difference of the hot plate and the film versus the temperature of hot plate.

3.1.6 Auger Spectroscopy with Ion Beam Milling

Auger spectroscopy with ion beam milling is used to study the atomic composition of the materials as a function of depth in the device. In this thesis, most of the work is focused on the interdiffused bilayer devices. Auger spectroscopy combined with ion beam milling is used to scan the concentration depth profile of various atoms. Auger spectroscopy is a powerful tool as it can provide information on the depth profiles of devices produced under different conditions and hence can be related to its performance. An energetic electron beam (1KeV-20 KeV) bombards the sample surface, resulting in the multi-step ejection of an Auger electron. The energetic electron beam leads to the removal of an inner shell electron to form a vacancy [Figure 3.6A]. There are two possible processes that can be used to fill this vacancy.

- An electron from higher shell falls to the inner shell, emitting an x-ray photon of energy $h\nu = E_{low} - E_{high}$, [Figure 3.6B].
- An electron falls from higher shell to inner shell, and the excess energy is used to release another electron called an Auger electron [Figure 3.6C]. The characteristic kinetic energy of the Auger electron is given by,

$$E_{kin} = (E_{low} - E_{high}) - E_{high} \quad .$$

The measured kinetic energy of secondary electrons is unique for each element and hence can provide information on the type of atoms present [2]. This method when used with ion beam milling, gives the compositional analysis of the sample as a function of the depth. The elements that can be detected by this method are Lithium to Uranium with the detection limit of 0.1%-1% atomic concentration. Figure 3.6 shows the schematic of process of the emission of the Auger electron. The scanning auger spectroscopy system (model # 610 Perkin-Elmer) is used to study the surface layer of the sample. Ion beam milling, which is done by sputtering the surface with ions, is combined with the surface scan to do the depth profiling. After each surface scan, a part of layer is removed by sputtering followed by the next surface scan. In this thesis, the etch rate is maintained at 5 nm/cycle. The polymers used in this work are P3OT and P3HT which have sulfur in addition to the carbon which is present in the fullerenes. Hence, the trace of the sulfur in the depth profile of interdiffused devices provides information on the extent of interdiffusion which can be related to the performance of the devices.

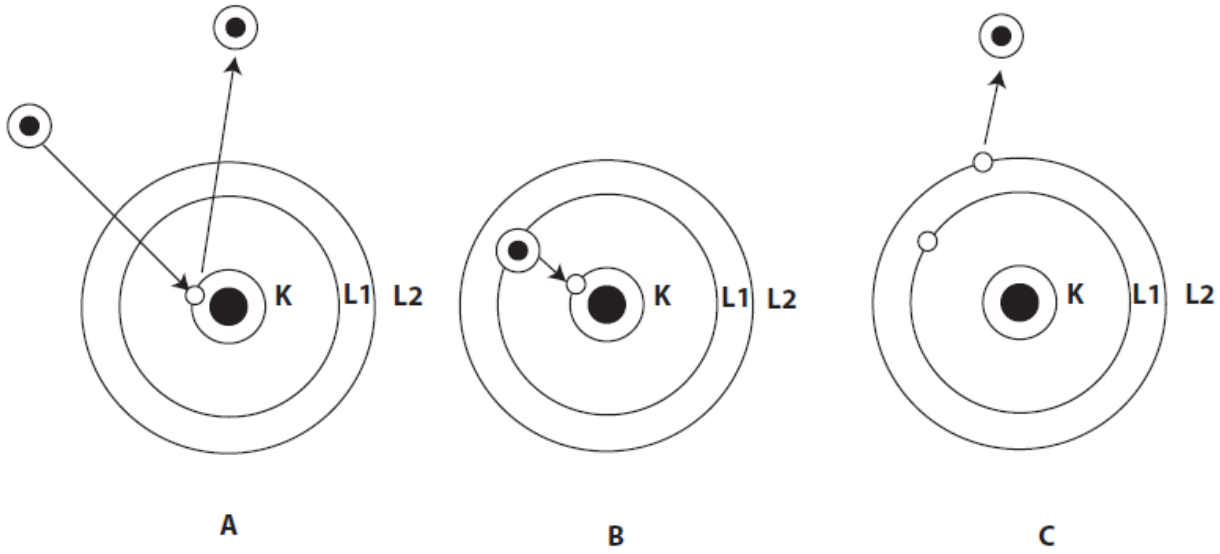

Figure 3.6 Schematic of the Auger electron emission process, **A.** Incident of electron, **B.** Electron moves from higher shell to inner shell vacancy, **C.** Release of an Auger electron.

3.1.7 X-ray photoelectron spectroscopy (XPS)

X-ray photoelectron spectroscopy is a quantitative spectroscopic tool that can measure the elemental composition in the material. X-ray photoelectron spectroscopy combined with sputtering is another method used in this thesis, in order to study the atomic concentrations of the materials as a function of the depth of the device. An X-ray beam is used to irradiate the sample surface which results in the ejection of core level electrons. A photon of energy (hν) is used to bombard the material and is absorbed by an electron with binding energy E_b. The photoelectrons are ejected with the kinetic energy given by,

$$E_k = h\nu - E_b - \phi \quad .$$

Here, ϕ is the work function required to remove the electron from the surface. The photoelectrons studied are core electrons as the core electrons carry precise information about individual atoms. The electrons that are far from the nucleus as are not bound very strongly, does not carry information about the precise atoms. The ejected photoelectrons are separated with respect to the energy of the elements as the energy of the core electrons from each element is different. XPS is based on the photoelectric effect as explained by Einstein in 1905. Figure 3.7 shows the schematic of the photoelectric effect.

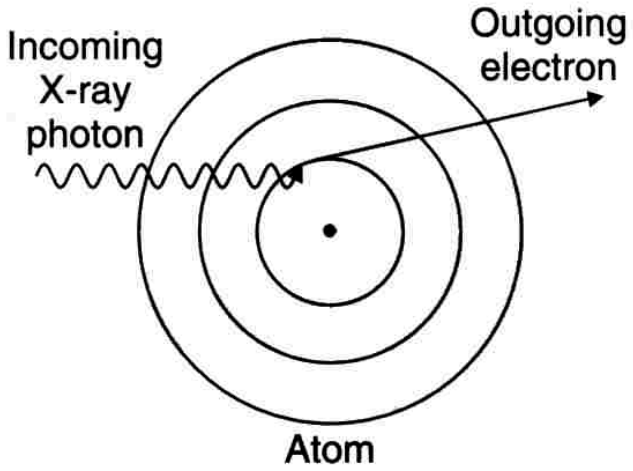

Figure 3.7 Schematic of the photoelectric process

In 1960, Dr. Siegbahn and his research group invented the XPS technique for which he was awarded Nobel Prize in 1981. The ejected electrons that are studied at each surface scan come from the top 1-10 nm of the sample. In order to study concentration gradients in the interdiffused devices, sputtering is done at the rate of 10 nm/cycle after each surface scan so that sulfur can be traced as a function of the depth. The elements that can be detected with this method are Lithium to Uranium with the detection limit of 0.1-1% atomic concentration.

3.2 Device Structure

The general device structure of the organic photovoltaic bilayer device studied in this work is shown in Figure 3.8. The active device layer is sandwiched between the anode and cathode. Here ITO-coated glass along with poly (3,4-ethylenedioxythiophene) poly(styrenesulfonate) (PEDOT: PSS) serve as an anode and Aluminum serves as the cathode. The light enters the device through the glass substrate and is absorbed in the first pass, absorbed in a second pass after reflecting off the cathode or exits again through the glass surface.

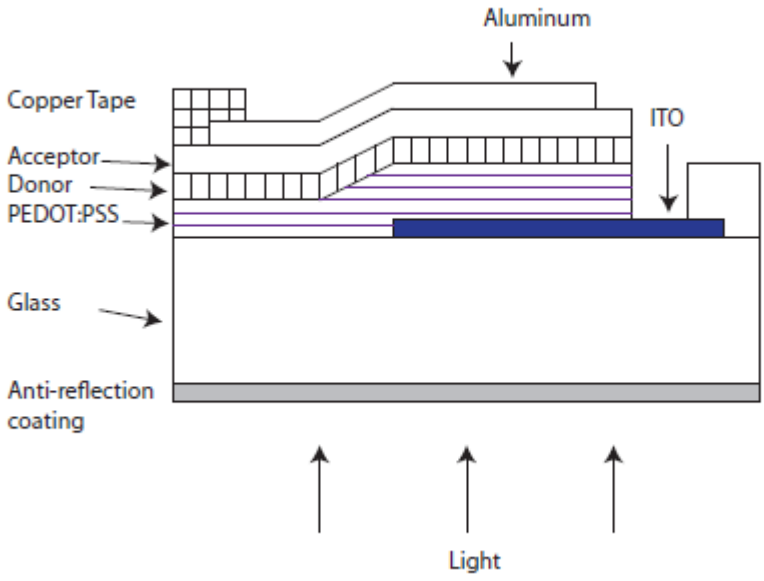

Figure 3.8 Schematic of bilayer device structure

The ITO-coated glass substrate is first etched so that ITO is present at the central ½ of the slide, and hence contacts can be made at the non-ITO surface in order to avoid shorting of the device. Etching is done by masking the regions which are not to be etched with electric insulation tape. The slide with electric tape is immersed in a 1:1 solution of 12.1 M HCl and de-ionized water for one hour, in order to dissolve the exposed ITO. After the etching process, the slide is rinsed and cleaned with acetone in order to get rid of any tape. These slides are further sonicated in 30% NH_4OH:H_2O_2 solution. The etched ITO glass slide is first spin coated with a layer of PEDOT:PSS which serves as the transparent anode through which light is incident on the device. The PEDOT: PSS is followed by a layer of donor and then acceptor material, on top of which aluminum is evaporated to form the cathode. The thickness of the donor and acceptor layer is maintained in the range of tens of nanometers. Bilayer devices further can be heated on the hot plate so that a concentration gradient is achieved in the devices. Adhesive tape of copper is used as contacts; these contacts are placed on the aluminum electrode in a region where the ITO layer is removed in order to prevent shorting through the film. The effective area of the device is the region in the middle that is sandwiched by both the ITO and Al electrodes.

The devices are made on 1" by 1" ITO glass substrates. Figure 3.9 shows the schematic of the final structure of the completed device. There are 8 devices with approximate active area of 0.12 cm^2 each on a 1" by 1" substrate. This is achieved by using a mask during aluminum deposition so that the slide is divided into 8 parts. The devices are labeled A through H.

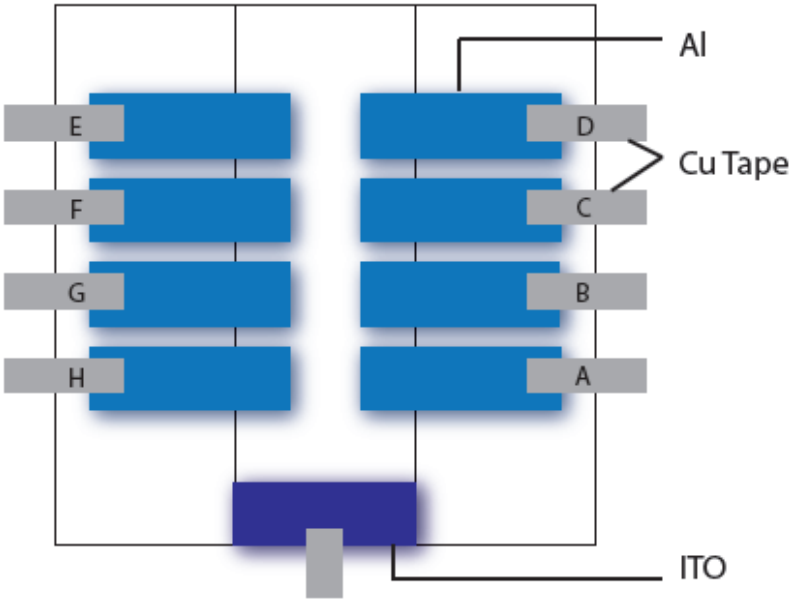

Figure 3.9 Schematic of the final layout of the device.

3.3 Donor Materials

This section provides details on the donor materials studied in this thesis.

3.3.1 Donor - P3OT

Poly (3-octylthiophene-2,5-diyl) semiconducting polymer that is hereafter referred to as P3OT has been intensely studied as a donor material in this thesis. The chemical structure of P3OT is shown in Figure 3.10. P3OT was purchased from Rieke Metals (4003 E, lot number BS12-49) with a molecular weight of (~142,000) in a regioregular structure (Typical results are between 90% and 94% regioregularity).

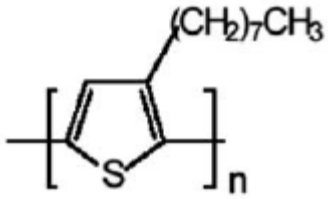

P3OT

Figure 3.10
Structure of P3OT.

The regioregular structure imparts crystallinity and hence P3OT is micro-crystalline, therefore exhibiting a melting point T_m (melting point temperature) as well as a T_g (glass transition temperature). T_m was determined to be 187 ^oC by DSC, however T_g could not be determined but is expected to be below 100 ^oC [3]. The crystallinity of P3OT increases upon annealing which can be used to improve the device performance. At temperatures above the glass transition, the polymer becomes soft and hence enables the diffusion of the acceptor into the polymer easier. Cyclic voltammetry is often used to find the HOMO and LUMO values of the polymer. Different research groups have reported different values for the HOMO and LUMO levels of P3OT. The band gap is in the range of 1.6 eV to 2.1 eV, which is in visible wavelength spectrum range. In 2003, Sensfuss *et al.* reported a HOMO value of -5.25 eV and LUMO of -3.55 eV for P3OT [4, 5, and 7]. In 2002, Gebeyehu *et al*. reported a HOMO of -4.9 eV and LUMO of -2.8 eV [6]. The absorption maximum for P3OT is observed at 512 nm and the α (absorbance per unit length) value for P3OT, as reported from previous work, is 1.38×10^5 cm^{-1}, measured at 512 nm [7].

3.3.2 Donor - P3HT

Poly (3-hexylthiophene) is another conducting polymer which has been studied extensively in this thesis, and hereafter is referred to as P3HT. Bulk as well as bilayer interdiffused devices have been made from P3HT with PCBM as an acceptor material. Figure 3.11 shows the chemical structure of P3HT.

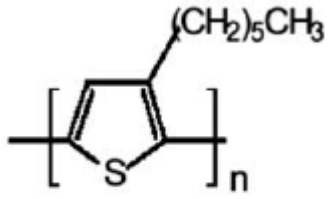

P3HT

Figure 3.11
Structure of P3HT.

Cyclic voltammetry experiments done on films of P3HT have also been used to find the HOMO and LUMO levels of P3HT [4,7]. The HOMO level value is at -5.20 eV and LUMO level is at -3.53 eV. It has been found the oxidation potential, which relates to the HOMO level, and the reduction potential, which relates to the LUMO level, are slightly dependent on the length of alkyl chains. As the length of the side chain decreases, there is an increase in the density of π electrons due to improved interchain coupling which enhances the electron donation character and hence favors the oxidation. The oxidation potential shows a direct dependence on the alkyl chain length whereas the reduction potential shows inverse dependence [7]. The absorption maximum for P3HT is observed at 500 nm as is evident from Figure 3.3 and the value of the

absorption coefficient is $1.75x10^5 cm^{-1}$ at 500 nm. It has been observed that with the decrease in the length of side chain, the value of the absorption coefficient increases [7].

It has been found that regioregular P3HT have higher values of hole mobilities compared to other conducting polymers and values of the order of 0.1-0.3 $cm^2V^{-1}s^{-1}$ has been observed [8, 18]. However these values are observed in FET configuration. The mobility values observed in diode configuration are much lower in the range of 10^{-4} $cm^2V^{-1}s^{-1}$. Coakley *et al*. demonstrated that hole mobility in P3HT can be increased to the range of 10^{-3} $cm^2V^{-1}s^{-1}$ by aligning the polymer chains in the direction perpendicular to the substrate in vertically oriented nanopores. The mobility values observed for P3HT depend not only on the regioregularity but also on the process of film formation. It has been found that thin films of P3HT can adopt microcrystalline and anisotropic lamellar microstructures with stronger π-π chain interactions.

3.3.3 Donor - Porphyrins

Porphyrin is another donor material which is investigated in this thesis. Porphyrins have been found to possess good thermal and photo stabilities. They also exhibit some intriguing electrical and optical properties, so that there is extensive research into their application in optical and optoelectronic devices such as photovoltaic cells, OLED's and OFET's [9]. Porphyrins are macrocyclic aromatic compounds which are similar to chlorophyll and are p-type organic semiconductors [10]. Porphyrins have been investigated in the past as the light absorber donor material in photovoltaic devices [11, 12]. However, the lack of solubility of porphyrins in most of the organic solvents limits its potential application in bulk heterojunction photovoltaic devices. However, the derivatives of porphyrins which can be soluble in various organic solvents can be sought as the active materials. 5,10,15,20-Tetraphenyl-21H,23H-porphine zinc (ZnTPP) is

porphyrin derivative that is used in this thesis as the p-type donor in Porphyrin:PCBM devices. ZnTPP has strong optical absorption in the visible spectrum [14] and is expected to form co-crystallites with PCBM [14, 15].

3.4 Acceptor materials

This section discusses the acceptor materials used in this thesis.

3.4.1 Acceptor – PCBM

[6,6] phenyl C_{61} butyric acid methyl ester, hereafter referred as PCBM is a derivative of C_{60}-fullerene which is solution processable and hence is a highly investigated acceptor material. PCBM was purchased from Nano-C (99.5% purity) for all the work in this thesis. In this thesis, PCBM is mostly used as an acceptor material with P3OT, P3HT as well with Porphyrins. Figure 3.13 shows the structure of the PCBM molecule. The addition of the side chain to C_{60} renders the PCBM molecule solubility in various solvents as well higher LUMO levels compared to C_{60}. HOMO and LUMO values as calculated by cyclic voltammetry are -6.1 eV and -3.83 eV [9]. The higher value of the LUMO leads to the better V_{oc} of devices made with PCBM compared to C_{60}. The electron mobility in PCBM has been found to be in the range of $10^{-3}cm^2V^{-1}s^{-1}$ and hence qualifies PCBM as an ideal candidate as n-type material. The mobility calculation done by different methods such as time of flight method as well as by SCLC regime methods have been found to be in quite agreement with the values of electron mobility at $2x10^{-3}$ $cm^2V^{-1}s^{-1}$[16].

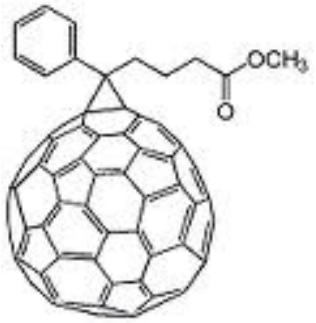

Figure 3.12
Structure of PCBM.

3.5 Electrode materials

The electrodes are used to collect the charges created by photon absorption. Electrodes are chosen with different work functions so as to create an internal field that can provide the path for the charge carriers to the electrodes. The work function of the anode is higher than the cathode so that band bending gives a preferred direction to the flow of electrons and holes. One of the electrodes has to be transparent so that light can be absorbed, the other electrode has to be reflecting so that photons that were not absorbed will be reflected and can be absorbed in the active layer.

3.5.1 Positive electrode

The two-layer system, consisting of indium tin oxide (ITO)-coated glass slide followed by the coating of conducting polymer poly (3,4-ethylenedioxythiophene): poly(styrenesulfonate) complex hereafter referred as PEDOT:PSS, serves as the positive electrode. ITO-coated glass slides were ordered from Delta Technologies, part #: CH-50IN-S109. These were 1 x 3 x 0.036

inch unpolished float glass slides, SiO_2 passivated with ITO coated on one surface with a sheet resistance of 8 Ω to 12 Ω and an anti-reflection coating on the other side. These slides had minimal absorption in the visible region of the spectrum and hence light can penetrate to the active layer of the device. PEDOT was obtained as an aqueous dispersion purchased from Bayer Corp. Baytron PH was used initially followed by Clevios PH as the conducting layer from the same supplier and the properties of the two were exactly same. The dispersion was filtered through 0.45 micron nylon syringe filter (Pall Life Sciences (AP-4438T)) before spin casting onto the ITO slide. PEDOT serves the two functions. First it reduces the roughness of the ITO surface so that the risk of pinhole shorts can be reduced. Also, it provides better alignment between the work function of ITO and the active layer [4]. Hence, it acts as the buffer layer, as the work function of ITO is at -4.7 eV and of PEDOT: PSS is at -5.2 eV and hence it can provide better band alignment of ITO to active layer [17].

3.5.2 Negative electrode

Aluminum (Al), with a work function of 4.3 eV [14] serves as the negative electrode. This negative electrode also serves a dual function. It is highly reflective and reflects the photons that are not absorbed in the active layer so that they will be absorbed once they are reflected. Also, the suitable work function provides the effective band bending.

The Al electrodes were evaporated from 99.9% pure Al granules purchased from Alfa Aesar. This evaporation is done in the vacuum evaporator from Ladd Research at pressure in the range of $4x10^{-6}$ Torr. The Al granules are placed in tungsten basket (ME17-3x.025W from R.D. Mathis Company). The Al thickness is controlled with a STM-100 thickness monitor from Sycon instruments and the thickness is in the range of ~100 nm. The deposition rates are maintained at 1-3 nm/second. In this thesis, Al is mainly used as the negative electrode.

References

1. http://en.wikipedia.org/wiki/Beer-Lambert_law

2. http://en.wikipedia.org/wiki/Auger_electron_spectroscopy.

3. S. Malik, A.K. Nandi, "Crystallization mechanism of regioregular poly(3-alkyl thiophene)s" , **J. Polym. Phys**. 40 (18), 2073-2085, (2002).

4. Sam-Shajing Sun, N. S. Sariciftci, "Organic Photovoltaics, Mechanisms, Materials and Devices," CRC print, Taylor & Francis Group, Boca Raton,. Chapter 23, (2005).

5. S. Sensfuss, *et al*., "Characterisation of Potential Donor Acceptor Pairs for Polymer Solar Cells by ESR, Optical and Electrochemical Investigations", **Proc. of SPIE**, 5215, 129-140, (2004).

6. D. Gebeyehu, *et al*., "Hybrid Solar Cells Based on Dye – Sensitized Nanoporous TiO2 Electrodes and Conjugated Polymers as Hole Transport Materials", **Synth. Met.** 125, 279-287, (2002).

7. M. Al-Ibrahim , H.K Roth, M. Schroedner, A. Konkin, U. Zhokhavets , G. Gobsch, P. Scharff, S. Sensfuss, "The Influence of the Optoelectronic Properties of Poly(3-Alkylthiophenes) on the Device Parameters in Flexible Polymer Solar Cells",**Organic Electronics,** 6 65–77, (2005).

8. H. Sirringhaus, N. Tessler, and R. Friend, "Integrated optoelectronic devices based on conjugated polymers", **Science** (New York, N.Y.), 280 (5370), 1741-4, (1998).

9. H. Mao, Y. Sun, H. Li, Q. Zhou, X. Zhang, J. Shen, H. Xu, Sci. China, **Ser. B: Chem.**, 41,449-454, (1998).

10. Y. Harima, K. Takeda, K. Yamashita, "Molecular solid of zinc tetraphenylporphyrin as a model organic semiconductor with a well-defined depletion layer", **J. Phys. Chem. Solids,** 56, 1223-1229, (1995).

11. C.W. Tang, A.C. Albrecht," Chlorophyll-***a*** photovoltaic cells", **Nature**, 254, 507-509, (1975).

12. D. Gust, T.A. Moore, A.L. Moore, "Mimicking Photosynthetic Solar Energy Transduction" **Acc. Chem. Res.**, 34, 40-48, (2001).

13. Q. Sun, L. Dai, X. Zhou, L. Li, Q. Li, **Appl. Phys. Lett.**, 91, 253505-253501-253503, (2007).

14. T. Oku, T. Noma, A. Suzuki, K. Kikuchi, S. Kikuchi,"Fabrication and characterization of fullerene/porphyrin bulk heterojunction solar cells" **J. Phys. Chem. Solids**, 71, 551-555, (2010).
15. W.J. Belcher, K.I. Wagner, P.C. Dastoor, "The effect of porphyrin inclusion on the spectral response of ternary P3HT:porphyrin:PCBM bulk heterojunction solar cells", **Sol. Energy Mater. Sol. Cells**, 91, 447–452, (2007).
16. C. Waldauf, P. Schilinsky, M. Perisutti, J. Hauch, and C. J. Brabec, "Solution-Processed Organic n-Type Thin-Film Transistors", **Advanced Materials**, 15(24), 2084-2088, (2003).
17. T. M. Brown, J. S. Kim, R. H. Friend,F. Caciallia, R. Daik and W. J. Feast, "Built-in Field Electroabsorption Spectroscopy of Polymer Light-Emitting Diodes Incorporating a Doped Poly(3,4-ethylene dioxythiophene) Hole Injection Layer", **Appl. Phys. Lett**.,75,12, 1679-81, (1999).
18. Coakley *et al*., "Enhanced Hole Mobility in regioregular Polythiophene infiltrated in Straight Nanopores", **Advanced Functional Materials**, 15, 1927-1932, (2005).

Chapter 4

P3OT Donor and PCBM Acceptor

- ***Blends and Concentration gradient devices***

In this chapter, devices with P3OT as donor and PCBM as acceptor material are studied in detail. Different morphologies of device architecture such as bulk heterojunction, bilayer and thermally interdiffused devices are investigated at length. In bulk heterojunction devices, the thickness of the active layer and the annealing conditions are the two parameters that are studied. However, the focus of this chapter is on the bilayer and concentration gradient devices made with P3OT as donor and PCBM as acceptor. The parameters that are studied in detail for interdiffused devices are the thickness of the each layer and interdiffusion conditions [1].

4.1 P3OT: PCBM Blend/ Bulk Heterojunction

The bulk heterojunction or blend devices are the most common device architecture used for the fabrication of organic solar cell devices. Here, work is done on blend devices made by the dissolving the donor and acceptor materials in a common solvent and then by spin casting onto the ITO-coated glass substrate. The devices are made on 1" by 1" ITO glass substrates. Indium tin oxide (ITO) coated glass slides were spin-coated with poly (3,4-ethylenedioxythiophene): poly(styrenesulfonate) (PEDOT: PSS) complex (Bayer Corp.) at 1400 rpm. P3OT (Rieke metals, Inc) and PCBM (Nano-C) are co-dissolved in 1:1 ratio in chloroform to make a 3.0% wt/vol solution. The thickness of the active area of the devices is varied by changing the spin speed from 1000 to 1750 rpm. The devices are further annealed either before the deposition of electrodes, referred to as pre-annealing or after the electrode deposition, referred to as post-annealing. In

these devices, annealing is done by using the 1" by 1" kapton heater under vacuum ($4x10^{-6}$ Torr) to remove residual water and solvents and to increase the P3OT crystallinity for improved hole mobility [2]. Thermal evaporation of aluminum electrodes is carried out under high vacuum. The two parameters that are varied in these devices are the thickness of the active layer and the annealing conditions.

4.1.1 Effect of Variation of Active Layer Thickness

The thickness of the active layer is calculated by using the reflection and transmission date obtained using the Filmetrics instrument as explained in Chapter 3. A typical optical density plot of each layer is shown in Figure 4.1. The absorption peak at 340-350 nm corresponds to PCBM and the bulge around 500 nm to P3OT. The thickness can be calculated by using the value of the absorption coefficient at a particular wavelength.

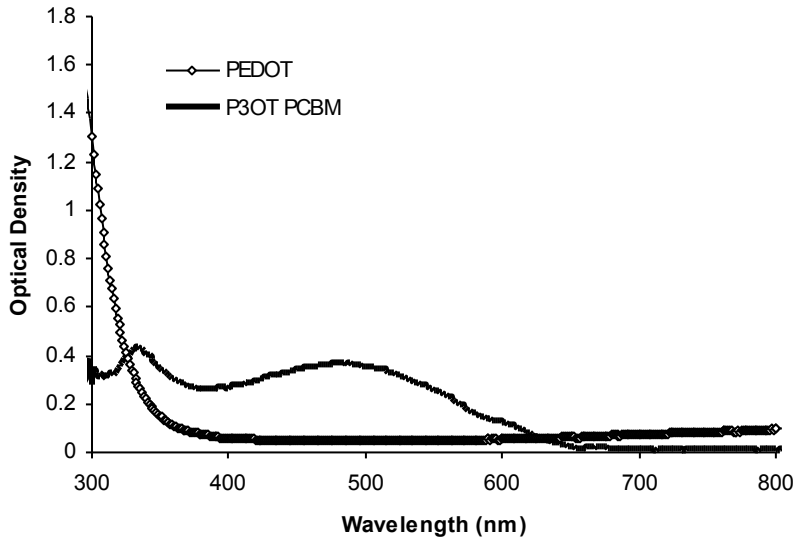

Figure 4.1 Optical density plot of separate layers of PEDOT and P3OT: PCBM.

Devices with active layer thicknesses of 50 nm, 80 nm and 110 nm were studied in detail. In these devices, similar annealing conditions were maintained. The annealing was done at 140 °C for 10 minutes. Figure 4.2 shows the EQE plot of the P3OT: PCBM blend devices with varied thickness. It has been found that devices with the active layer thickness of the order of 80 nm have better performance. The device with 50 nm active layer thickness has low active volume where charge separation can take place and hence lower efficiency. Devices with very high thickness have low efficiency because of the increase in the series resistance as is evident from Table 4.1.

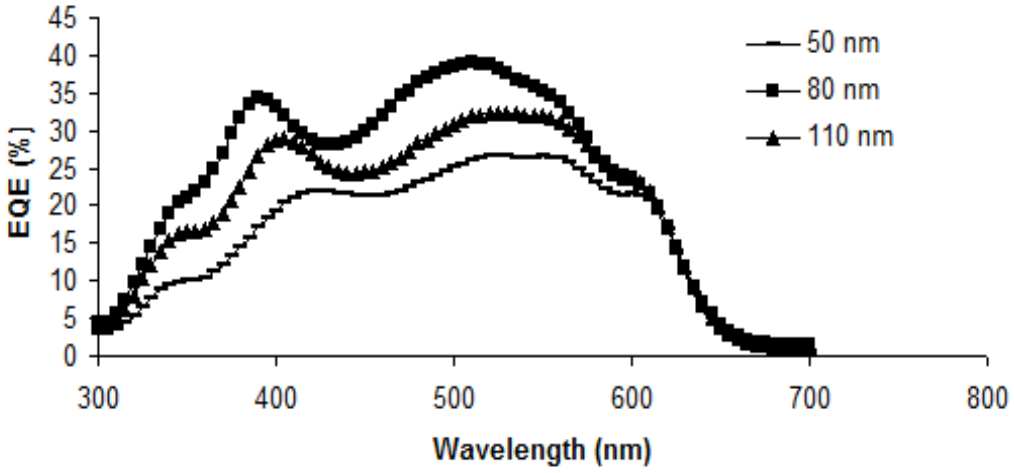

Figure 4.2 EQE spectra of the P3OT: PCBM blends with varied thickness annealed at 140 °C for 10 minutes.

The various parameters that are associated with the performance of solar cells are defined in Chapter 2. The values of the various parameters such as efficiency (under 470 nm as well as AM1.5), FF (470 nm and AM1.5), rectification ratio (RR), series resistance and shunt resistance for these devices are given in Table 4.1.

Table 4.1 Power conversion efficiency (470 nm, AM1.5), fill factor (470 nm, AM1.5), RR, Series resistance and shunt resistance for P3OT-PCBM bilayer devices with varied thickness.

Thickness	**50 nm**	**80 nm**	**110 nm**
Efficiency 470 nm (%)	1.4	2.4	1.3
Efficiency AM1.5 (%)	0.43	0.9	0.3
FF (470 NM)	0.45	0.54	0.4
FF(AM1.5)	0.29	0.27	0.23
RR	861	2942	167
Series resistance (ohm)	35	35	856
Shunt resistance (ohm)	$6.1x10^5$	$1.15x10^6$	$6.7x10^5$

As is evident from Table 4.1, the rectification ratio (RR) increases as the active layer thickness is increased from 50 to 80 nm and beyond that there is drop in the RR. The higher the RR, the better is the performance of the device. The series resistance increases abruptly with the increase in the thickness of the device in general. The increase in series resistance can be directly related to the drop in the device performance.

4.1.2 Effect of Variation of Annealing Conditions (Temperature and Time)

In order to study the effect of varied annealing conditions, the thickness of the active layer was maintained at 80 nm and the annealing conditions were varied. Figure 4.3 shows the EQE spectra of P3OT: PCBM blends annealed at different temperatures for varied amounts of

time. It has been found that annealing done beyond 5 minutes leads to the degradation in device performance. As it is evident from Figure 4.3, the devices that are annealed at 140 °C have better performance compared to the devices annealed at 130 °C or 150 °C. Also for the same thickness, increase of time of annealing from 5 minutes to 10 minutes, at 140 °C leads to degradation of device performance. Annealing for longer amounts of time or at higher temperatures beyond the T_g of the blend leads to the increased mixing of the two components leading to the degradation of the transport properties and device performance [7]. Also, annealing done for longer period of time or at higher temperatures leads to the formation of voluminous PCBM clusters that can damage the absorber-metal interface and hence degradation in the device performance [8].

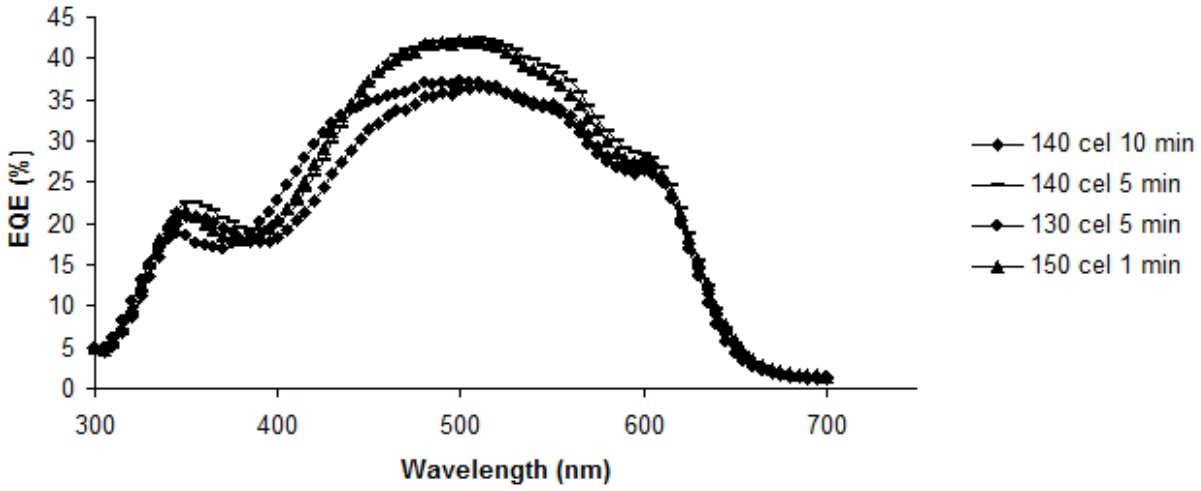

Figure 4.3 EQE spectra of P3OT: PCBM blends of thickness 80 nm annealed under different conditions.

Table 4.2 shows the various parameters studied for the P3OT: PCBM blends annealed under different conditions. As is evident from Table 4.2, the best performance is achieved for

devices annealed at 140 °C. The highest efficiency is obtained for devices annealed at 140 °C for 5 minutes. Efficiency of the order of 1.5% is obtained under AM1.5 solar simulated conditions for the devices with active layer thickness of 80 nm.

Table 4.2 Power conversion efficiency (470 nm, AM1.5), fill factor (470 nm, AM1.5), RR, Series resistance and shunt resistance for P3OT-PCBM blend devices with varied annealing conditions.

Annealing conditions	**130 °C 5 minutes**	**140 °C 5 minutes**	**140 °C 10 minutes**	**150 °C 1 minutes**
Efficiency 470 nm (%)	2.4	3.5	2.4	2.1
Efficiency AM1.5 (%)	1.1	1.5	0.9	0.3
FF (470 NM)	0.49	0.57	0.54	0.37
FF(AM1.5)	0.23	0.42	0.27	0.15
RR	1555	9253	2942	988
Series resistance (ohm)	73	32	35	240
Shunt resistance (ohm)	$9.87x10^5$	$3.1x10^6$	$1.15x10^6$	$3.6x10^6$

Although there are large number of studies reported on blend bulk heterojunction devices of P3HT and PCBM, there are very few reports on P3OT: PCBM devices. One study reports a V_{oc} of 0.635 V and AM1.5G power conversion efficiency of 1.1% for 1:3 concentrations of P3OT and PCBM [3] Another publication reports a V_{oc} of 0.60 V under 20 mW/cm^2 monochromatic illumination at 488 nm, but no results were given for simulated solar spectrum [4]. In this study done on P3OT: PCBM blend devices, efficiency of the order of 1.5% is achieved for devices annealed at 140 °C for 5 minutes.

4.2 P3OT/PCBM Bilayer Devices

Blend/ bulk heterojunction devices, in which the semiconducting polymer donor and fullerene acceptor are co-dissolved in an organic solvent and spin-cast into a single film, provide good charge transfer from electron donor to acceptor, but charge transport is potentially limited due to discontinuous pathways of the donor and acceptor materials to their respective electrodes. In contrast, bilayer devices provide optimized charge transport while the charge transfer is severely compromised as the charge transfer can occur only at the interface of the two layers. We have been developing an approach wherein a concentration gradient of the two components is achieved to maximize the concentration of the majority carrier component in the vicinity of each respective electrode while still providing proximity of the donors and acceptors to enable charge transfer [1,5,6]. In this thesis, some of the devices made using the bilayer approach are discussed first, followed by concentration gradient interdiffused devices.

PCBM is chosen as a preferred acceptor material to C_{60} for organic photovoltaic devices because the presence of the side chain enhances the solubility and the higher lowest unoccupied molecular orbital (LUMO) energy level relative to C_{60} leads to a higher open circuit voltage, V_{oc}. However, PCBM does not survive sublimation without substantial decomposition. Hence, a new approach for the fabrication of the bilayer device was developed in which the two layers are sequentially spin cast. *The spin-coating of a PCBM layer on a previously spin-cast layer of P3OT is critical to this work.* In contrast to C_{60}, which is not very soluble but is easily sublimed, PCBM is quite soluble in a number of organic solvents. In order to avoid dissolution of the P3OT layer during spin-coating of PCBM, it was necessary to find a solvent in which PCBM is well-soluble but which is a poor solvent is for P3OT. A variety of solvents were tested to see which can dissolve PCBM well compared to P3OT. It was found that pyridine dissolves PCBM fairly well

but does not wash off a layer of P3OT spin-cast from chloroform. To test this, 7-8 drops of pure pyridine were dropped onto a substrate having a P3OT layer and spinning at 2000 rpm. Optical density measurements were made on the P3OT layer before and after the pyridine wash as shown in Figure 4.4. It is evident from the figure that the thickness is essentially the same before and after pyridine washing. On the other hand, pyridine can dissolve PCBM at better than 25 mg/ml. *Hence Pyridine was used as the solvent for PCBM and chloroform for P3OT for P3OT/PCBM bilayer devices.*

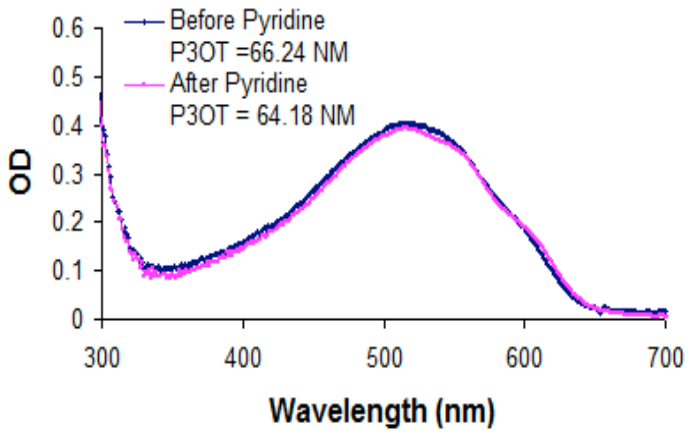

Figure 4.4 Optical density of a P3OT film on glass before and after washing with 7-8 drops of pyridine while spinning at 2000 rpm.

Indium tin oxide (ITO) coated glass slides were spin coated with poly (3,4-ethylenedioxythiophene): poly(styrenesulfonate) (PEDOT: PSS) complex (Bayer Corp.) at 1400 rpm. P3OT (Rieke Metals Inc.) was spin coated from 0.8% wt/vol solution in chloroform at 2750 rpm followed, in some cases, by annealing of the device at 120 ºC for 10 minutes. Annealing was

done under vacuum ($4x10^{-6}$ Torr) to remove residual water and solvents and to increase the P3OT crystallinity for improved hole mobility. PCBM was then spin cast from a 2.0% wt/vol solution in pyridine at 2450 rpm. The P3OT thickness was varied by changing the spin speed in the range 2000 rpm to 2750 rpm, while the concentration was maintained at 0.8% wt/vol. It was found that the PCBM thickness is quite independent of spin speed and is instead highly dependent on the amount of solution dropped onto the substrate. The PCBM thickness was thus controlled by varying the number of drops from 6 to 15 while the substrate spun at 2450 rpm. Pyridine was used as a wetting layer between P3OT and PCBM. About 10-15 drops of pyridine were applied to the substrate while it was spinning at 2450 rpm followed by PCBM immediately, without letting the pyridine dry. Aluminum electrodes were thermally evaporated after the deposition of the PCBM.

The bilayer P3OT-PCBM devices were found to have a monochromatic (470 nm) power conversion efficiency of ~0.2%. The 470 nm monochromatic power conversion efficiencies fill factors (FF), open circuit voltages (V_{oc}), short circuit current densities (J_{sc}), RR, series resistance and shunt resistance values are shown in Table 4.3 for a couple of devices with different thickness combinations.

Table 4.3 Monochromatic power conversion efficiency, fill factor, open circuit voltage, short circuit current density, RR, Series resistance and shunt resistance for P3OT-PCBM bilayer devices (*no annealing, no interdiffusion*)

Thickness	P3OT(85nm)/PCBM(62 nm)	P3OT(64 nm)/PCBM(45 nm)
Efficiency 470 nm (%)	0.16	0.23
FF 470 nm	0.43	0.42
V_{oc} 470 nm (Volts)	0.255	0.345
J_{sc} 470 nm (mA/cm^2)	-0.05	-0.06
RR	3800	156
Series resistance (ohm)	350	520
Shunt resistance (ohm)	$3.5x10^7$	$1.6x10^6$

As is evident from Table 4.3, the performance of the P3OT/PCBM device with thickness 64/45 nm is better to with 85/62 nm. In order to provide better interfacial area for the charge transfer, interdiffusion of the bilayer devices is done at varied temperatures for different amounts of time which is discussed in the next sections. The thickness of each layer and the annealing conditions are also varied to find the optimum thickness and the annealing conditions.

4.3 P3OT/PCBM Concentration Gradient Interdiffused Devices

The P3OT layer was annealed, in some cases, followed by spin casting the PCBM layer. P3OT/PCBM bilayer devices are then further heated so as to induce interdiffusion which can enhance the interfacial area for the charge transfer. The thickness of each layer and interdiffusion temperature and time were varied in order to optimize the efficiency of the devices. The thickness of the P3OT and PCBM films was determined from the optical density obtained from reflection and transmission measurements by the Filmetrics F20-UV thin film spectrometer system as described in Chapter 3. The absorption coefficient used for P3OT is 14 x 10^4 cm^{-1} at 512 nm and for PCBM is 2 x 10^4 cm^{-1} at 512 nm. Photocurrent spectra were measured using a 300 W Xe lamp in combination with a CVI CM 100 monochromator as the illumination source and a Keithley 485 picoammeter to record the short circuit currents I_{sc}. Photoresponsivity (*PR*) and EQE were evaluated from these measurements as explained in Chapter 3. *I–V* curves were measured with a Keithley 236 source measure unit in the dark, using the 470-nm monochromatic light of the Xe lamp and using the AM1.5G simulated solar spectrum described in Chapter 3.

It has been found with optimized parameters that P3OT-PCBM interdiffused devices can achieve a monochromatic power efficiency of ~2% at 470 nm and AM1.5G simulated solar spectrum efficiency of 1.0%. The devices were studied at different interdiffusion temperatures, with a primary focus on 140 ºC and 150 ºC. P3OT is a semicrystalline polymer with a melting point (T_m) of 187 ºC and a glass transition temperature (T_g) of the order of ~100 ºC [5]. Hence, annealing and interdiffusion were both carried out at temperatures above T_g but below T_m. In order to determine whether the increased polymer crystallinity caused by annealing would hinder diffusion of PCBM into the polymer film, devices were fabricated both with and without annealing of the P3OT film prior to the interdiffusion step.

4.3.1 Non-annealed P3OT/PCBM Interdiffused Devices

First, several interdiffused devices were made without annealing the P3OT layer prior to deposition of PCBM and interdiffusion. Figure 4.5 shows the EQE spectra of P3OT-PCBM devices with and without interdiffusion and without prior annealing. Here interdiffusion is carried out at 150ºC for 10 minutes. The interdiffused devices consisted of P3OT/PCBM thicknesses of 61 nm / 54 nm and 73 nm / 51 nm. These devices had the highest efficiencies of ten devices of varying thicknesses made without P3OT annealing prior to interdiffusion. The EQE spectra show the enhanced performance of the devices which are interdiffused compared to the bilayer devices. The better performance is due to the increased interfacial area provided by interdiffusion so that charge transfer is more pronounced.

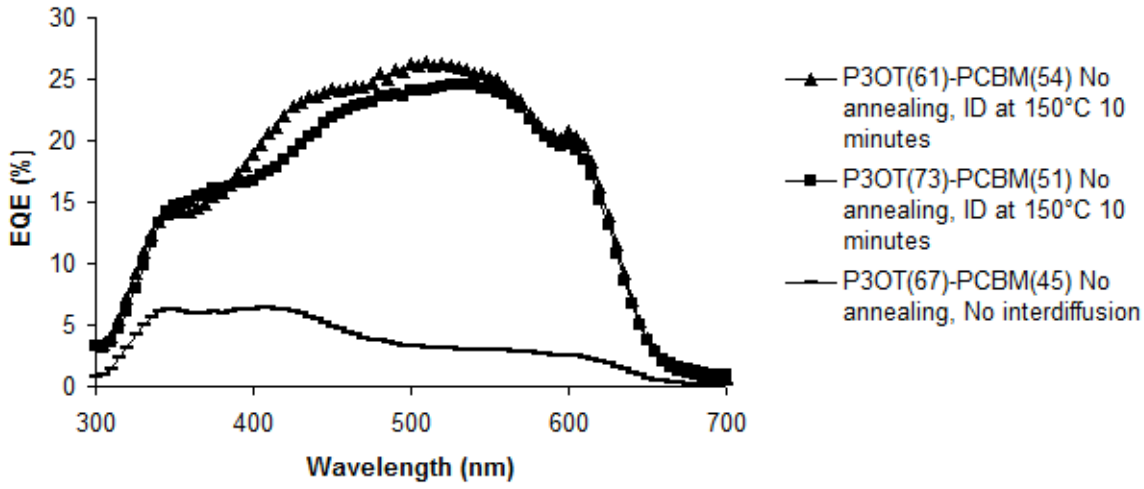

Figure 4.5 EQE spectra for P3OT-PCBM devices with and without interdiffusion. Interdiffusion is carried out at 150 ºC for 10 minutes without prior annealing. Individual film thicknesses (nm) prior to interdiffusion are indicated in parentheses.

The 470 nm monochromatic and AM1.5G power conversion efficiencies fill factors (FF), open circuit voltages (V_{oc}), short circuit current densities (J_{sc}), RR, series resistance and shunt resistance values for the non-annealed interdiffused devices are shown in Table 4.4. The highest AM1.5G power conversion efficiency obtained was 0.38%. It can be seen by comparison with Table 4.3 that interdiffusion results in an order of magnitude increase in the monochromatic power conversion efficiencies compared to the bilayer devices which is due to more interfacial area for the charge transfer in interdiffused devices.

Table 4.4 Monochromatic and AM1.5 power conversion efficiency fill factor, open circuit voltage, and short circuit current density for interdiffusion done at 150 ºC for 10 minutes without prior annealing (*Interdiffused, Non –annealed*)

Thickness	P3OT(61 nm)/PCBM(54 nm)	P3OT(73nm)/PCBM(51 nm)
Efficiency 470 nm (%)	1.45	1.5
Efficiency AM1.5 (%)	0.28	0.38
FF 470 nm	0.44	0.47
FF AM1.5	0.33	0.32
V_{oc} 470nm (Volts)	0.385	0.385
V_{oc} AM1.5 (Volts)	0.395	0.485
J_{sc} 470 nm (mA/cm^2)	-0.34	-0.32
J_{sc} AM1.5 (mA/cm^2)	-2.65	-3.7
RR	900	740
Series resistance (ohm)	60	124
Shunt resistance (ohm)	2.5×10^6	1.7×10^6

4.3.2 Annealed P3OT/PCBM Interdiffused Devices

In this section, annealed P3OT/PCBM devices are studied. Here, P3OT is annealed prior to sequential PCBM deposition. The thickness and annealing conditions are first varied to find

the optimum conditions for the best device performance. Then the effect of interdiffusion temperature and time is studied on the device performance.

A. Effect of Variation of Thickness of Individual Layer

A series of experiments were done on P3OT/PCBM interdiffused devices. The thickness of each layer was varied to find the optimum thickness of each layer for the best device performance. The thickness was calculated from the optical density measurements calculated from the Filmetrics data collected for each subsequent layer. Figure 4.6 shows the typical optical density plot of separate layers of PEDOT, P3OT and PCBM.

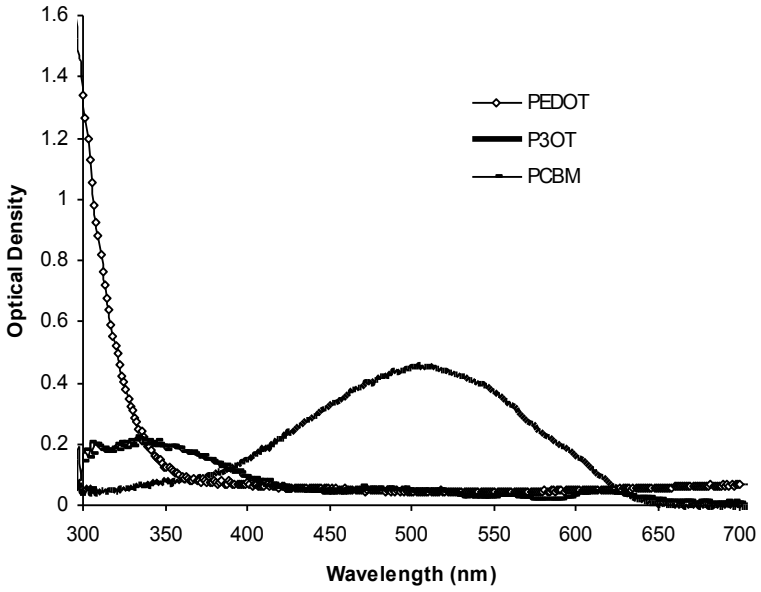

Figure 4.6 A typical optical density plot of separate layers of PEDOT, P3OT and PCBM.

Figure 4.7 shows the plot of the monochromatic efficiency (470 nm) for interdiffused devices with varied thickness. Here, the annealing conditions were maintained at 120 °C for 10

minutes. Interdiffusion was done at 150 °C for 10, 20, 30 and 40 minutes. At each particular interdiffusion condition, devices with varied thickness of each layer are studied.

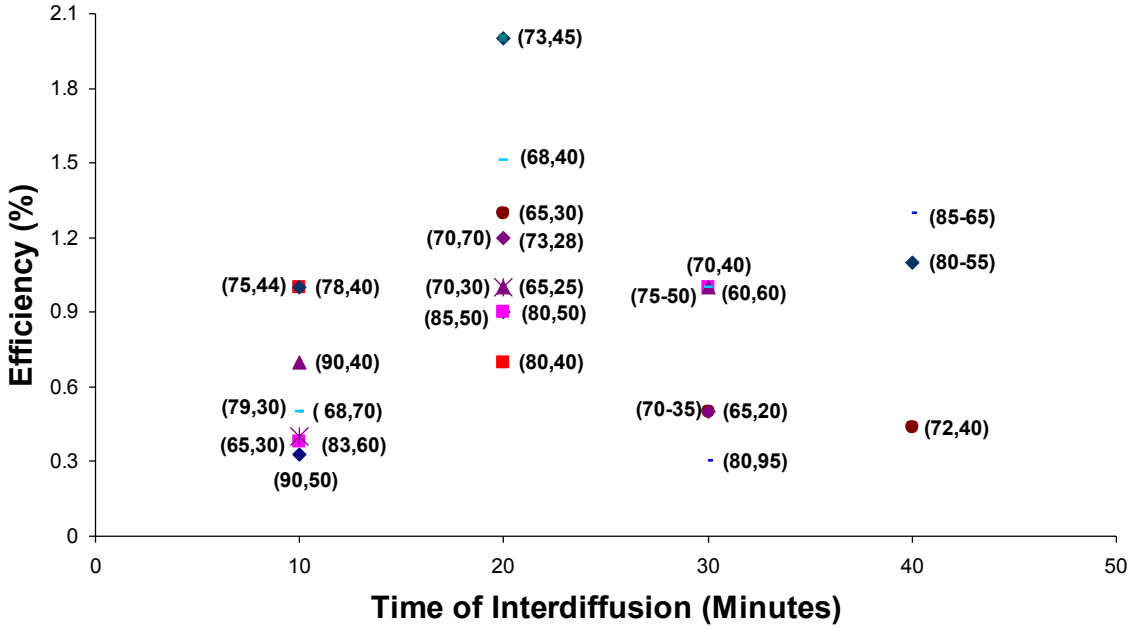

Figure 4.7 Monochromatic (470 nm) power conversion efficiency vs. time of interdiffusion for varied device (P3OT, PCBM) thickness for interdiffusion at 150 ºC and with annealing at 120 ºC for 10 minutes.

It is evident from Figure 4.7 that devices with a thickness of the order of 70 nm of P3OT and 40-50 nm PCBM have better efficiency compared to the others. Furthermore, the devices which are interdiffused at 150 °C for 20 minutes have the highest efficiency.

B. Effect of Variation of Annealing Conditions (Temperature)

In all of the next devices, the P3OT layer was annealed prior to spin-casting of PCBM and interdiffusion. It was found that the performance of the devices with prior annealing was better than devices without prior annealing. It was thus concluded that the increased P3OT crystallinity induced by annealing does not interfere with the interdiffusion process. Annealing is done under different conditions while keeping the thickness of each layer and interdiffusion conditions the same so as to find out the optimum annealing conditions. Figure 4.8 shows EQE spectra of the devices annealed at 110 ºC, 120 ºC, 130 ºC, and 140 ºC for devices with P3OT thickness of 70 nm and PCBM thickness of 40-50 nm. The interdiffusion conditions were maintained at 150 ºC for 20 minutes for these devices. It is evident from Figure 4.8 that the EQE of the devices annealed at 120 ºC is higher than the ones annealed at 110 ºC, 130 ºC and 140 ºC.

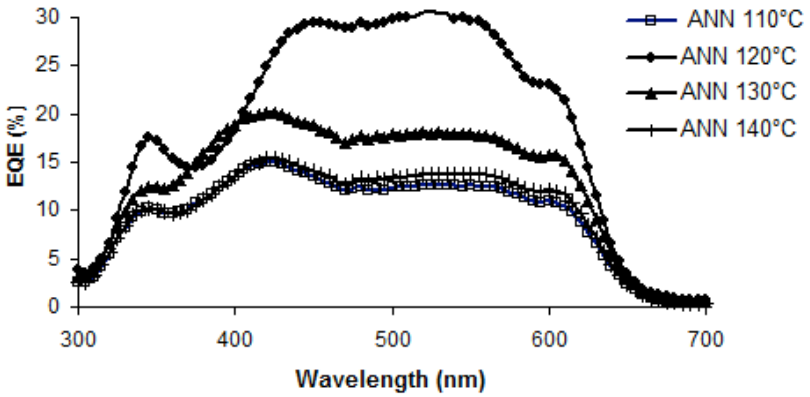

Figure 4.8 EQE spectra for annealing for 10 minutes at temperatures of 110 ºC, 120 ºC, 130 ºC, and 140 ºC with the interdiffusion carried out at 150 ºC for 20 min. The thicknesses were maintained constant at 70 nm for P3OT and 40-50 nm for PCBM.

Tables 4.5 shows the power conversion efficiency, fill factor, open circuit voltage and short circuit current density of the P3OT-PCBM interdiffused devices under monochromatic (470 nm) as well as AM 1.5 illuminations, for the devices annealed under different conditions while maintaining the thickness of each layer and interdiffusion conditions constant. As is evident, devices which are annealed at 120 °C for 10 minutes show the better performance compared to the devices which are annealed at other temperatures.

Hence, in the rest of the experiments, the annealing conditions for the P3OT layer are maintained at 120 °C for 10 minutes prior to PCBM deposition and the thickness of P3OT/PCBM were maintained at 70/ (40-50) nm.

Table 4.5 Monochromatic and AM1.5 power conversion efficiency, fill factor, open circuit voltage and short circuit current density for interdiffusion with varied annealing temperatures and interdiffusion done at 150 ºC for 20 minutes.

Annealing temperature (10 minutes)	Efficiency 470 nm (%)	Efficiency AM 1.5G (%)	FF 470 nm	FF AM 1.5G	V_{oc} 470nm (Volts)	V_{oc} AM1.5G (Volts)	J_{sc} 470 nm (mA/cm^2)	J_{sc} AM 1.5G (mA/cm^2)
110 ºC	0.75	0.3	0.4	0.36	0.395	0.515	-0.185	-1.6
120 ºC	2.0	1.0	0.5	0.44	0.385	0.525	-0.395	-4.1
130 ºC	0.9	0.3	0.39	0.32	0.365	0.515	-0.228	-1.73
140 ºC	0.7	0.3	0.41	0.33	0.375	0.555	-0.171	-1.49

C. Effect of Variation of Interdiffusion Conditions (Temperature and Time)

The interdiffusion temperature and time are two major factors that affect the performance of P3OT-PCBM devices by determining the extent of interdiffusion of the two layers at a particular thickness of each layer. Hence in this section, the interdiffusion temperature and time are the two parameters that are studied in detail while maintaining the constant annealing and thickness conditions. Interdiffusion was done at 140 °C and 150 ºC for varied amounts of time for devices with constant thickness of 70 nm for P3OT and 40-50 nm for PCBM. In these devices, the annealing is maintained at 120 ºC for 10 minutes. The EQE spectra for these devices

are shown in Figure 4.9 and Figure 4.10. Figure 4.9 shows the EQE spectra of the P3OT/PCBM devices which are interdiffused at 140 °C for 10, 20, 30 and 40 minutes. It is evident that the device which was interdiffused for 20 minutes shows the best device performance.

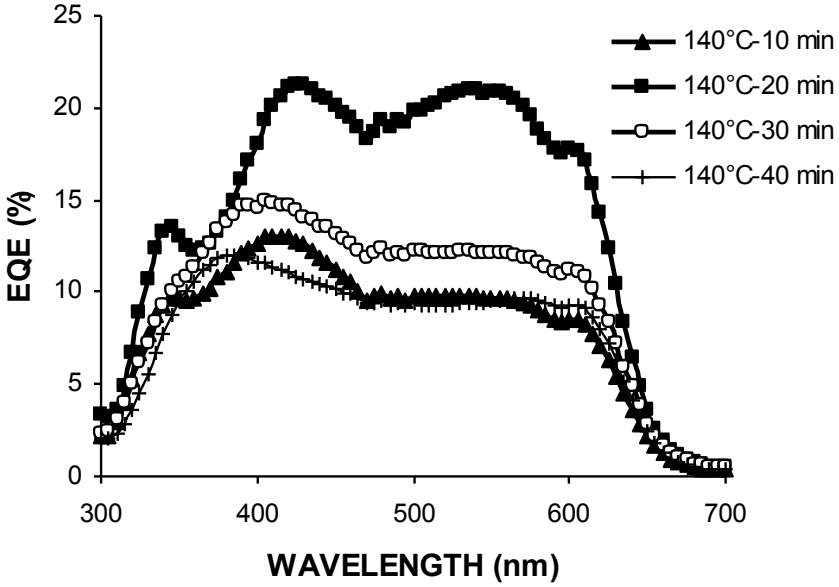

Figure 4.9 EQE spectra for P3OT (70 nm)-PCBM (40-50 nm) devices interdiffused at 140 ºC for 10, 20, 30 and 40 minutes.

Figure 4.10 shows the EQE plot of the P3OT/PCBM devices which were interdiffused at 150 °C for 10, 20, 30 and 40 minutes. The devices which were interdiffused at 150 °C for 20 minutes showed highest efficiency. Efficiency of the order of 2% under monochromatic lamp and 1% under AM1.5G solar simulator lamp is achieved for the devices interdiffused at 150 °C for 20 minutes.

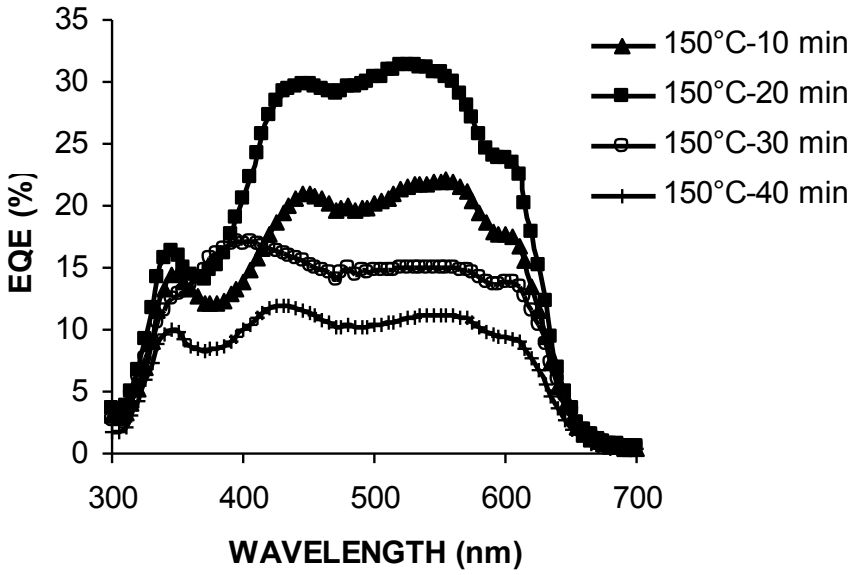

Figure 4.10 EQE spectra of P3OT/PCBM devices interdiffused at 150 °C for 10, 20, 30 and 40 minutes.

Figure 4.11 shows the overall trend of the monochromatic power conversion efficiency (470 nm, 4.2 mW/cm^2) values for P3OT(70) /PCBM (40-50) nm as the interdiffusion time is varied at 140 ºC and 150 ºC. Each data point is an average over 2-3 devices with the same thickness. As is evident from the Figure 4.11, the maximum efficiency occurs when the interdiffusion is done for 20 minutes, and there is a decrease in device performance for interdiffusion done beyond 20 minutes. Furthermore, the devices which are interdiffused at 150 °C have better performance compared to the devices interdiffused at 140 °C.

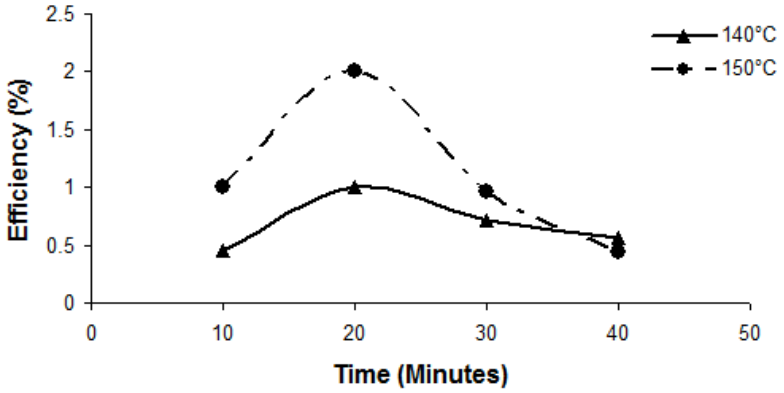

Figure 4.11 Averaged monochromatic power conversion efficiency (470 nm, 4.2 mW/cm^2) vs. time of interdiffusion at 140 ºC and 150 ºC for devices with P3OT and PCBM thickness of 70 nm and 40-50 nm, respectively.

The series resistance of the devices is calculated by plotting the differential resistance as a function of voltage. The series resistance is calculated using the formula,

In the high limit voltage, the value of the differential resistance is the series resistance. Figure 4.12 shows the series resistance as a function of the time of interdiffusion for devices interdiffused at different temperatures.

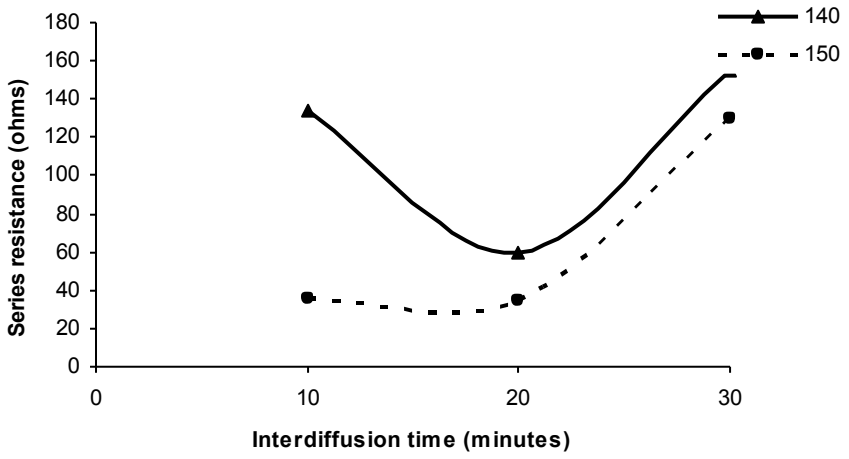

Figure 4.12 Series resistance vs. time of interdiffusion at 140 ºC and 150 ºC for devices with P3OT and PCBM thickness of 70 nm and 40-50 nm, respectively.

The series resistance is plotted as a function of time of interdiffusion in Figure 4.12. As is evident, the devices which are interdiffused for 20 minutes have the lowest series resistance and support the results of the better performance of the devices at these conditions. It indicates that devices with P3OT thickness (70 nm) and PCBM thickness (40-50 nm) when interdiffused at 150 °C for 20 minutes lead to the interpenetrating network with lowest series resistance. For interdiffusion done for longer period, there is an increased intermixing of the polymer and fullerene components which leads to the degradation in the transport properties and hence contributes to the increase in series resistance [7].

Table 4.6 shows the power conversion efficiency, fill factor, V_{oc} and J_{sc} of the P3OT-PCBM interdiffused devices under monochromatic (470 nm) as well as AM 1.5 illuminations. The interdiffusion was done at 150 ºC for varied periods of time and the thicknesses of the P3OT and PCBM were maintained at 70 nm and 40-50 nm, respectively. The short circuit current

density is maximized for 20 minutes of interdiffusion, while the open circuit voltage values are similar for 20 and 30 minutes of interdiffusion and the fill factor exhibits relatively modest variation. Efficiency of the order of 1.0% under AM1.5 illumination is achieved for devices interdiffused at 150 °C for 20 minutes.

Table 4.6 Monochromatic and AM1.5 power conversion efficiency, fill factor, open circuit voltage, and short circuit current density for interdiffusion done at 150 ºC for varying time interval.

Interdiffusion Time	Efficiency 470 nm (%)	Efficiency AM 1.5 (%)	FF 470 nm	FF AM 1.5	V_{oc} 470nm (Volts)	V_{oc} AM1.5 (Volts)	J_{sc} 470 nm (mA/cm^2)	J_{sc} AM 1.5 (mA/cm^2)
10 min	1.0	0.6	0.41	0.38	0.355	0.515	-0.272	-3.2
20 min	2.0	1.0	0.5	0.44	0.385	0.525	-0.395	-4.1
30 min	1.0	0.55	0.39	0.36	0.395	0.565	-0.247	-2.76
40 min	0.44	0.3	0.42	0.43	0.285	0.435	-0.141	-1.67

Table 4.7 shows the RR, series resistance and shunt resistance calculated for the devices interdiffused at 140 °C and 150 °C for various amounts of time.

Table 4.7 RR, series resistance and shunt resistance parameters for devices interdiffused at 140 ºC and 150 ºC for varied amounts of time

Device	RR	Series resistance (ohm)	Shunt resistance (ohm)
150 °C/10 minutes	2463	36.6	$7.1x10^5$
150 °C/20 minutes	2934	35.5	$1.8x10^6$
150 °C/30 minutes	2000	130	$4 x10^6$
150 °C/40 minutes	670	38	$5.8x10^5$
140 °C/10 minutes	1445	134	$3.5 x10^6$
140 °C/20 minutes	3825	49	$3.6 x10^6$
140 °C/30 minutes	2004	130	$4.11 x10^6$
140 °C/40 minutes	563	49	$2.4 x10^6$

As is evident from Table 4.7, the devices interdiffused for 20 minutes at a given temperature have higher rectification values compared to the ones interdiffused for 10, 30 or 40 minutes. Similarly, the series resistance values are lower for devices with 20 minutes interdiffusion and the shunt resistance values are higher for 20 minutes interdiffusion. Recall that, ideally the series resistance values should be low and the shunt resistance and rectification ratio should be higher for efficient device performance.

Figure 4.13 compares the J-V curves under AM1.5G illumination for the devices in which either the P3OT layer is not annealed or is annealed followed by interdiffusion. Both sets of devices were interdiffused after the sequential spin cast of PCBM at varied interdiffusion

conditions. The interdiffusion was done at 150 °C for 10, 20 and 30 minutes for the annealed P3OT/PCBM devices and was done at 150 °C for the non-annealed P3OT/PCBM devices. It is evident from the comparison of the performance of performance of annealed interdiffused devices to the non-annealed interdiffused devices that prior-annealing does not interfere with the interdiffusion of P3OT-PCBM bilayer. Further, the V_{oc} of the annealed interdiffused devices is higher than that of non-annealed interdiffused devices by 0.1/0.2 Volts. Along with that device efficiency of annealed interdiffused devices is higher to the non-annealed interdiffused devices.

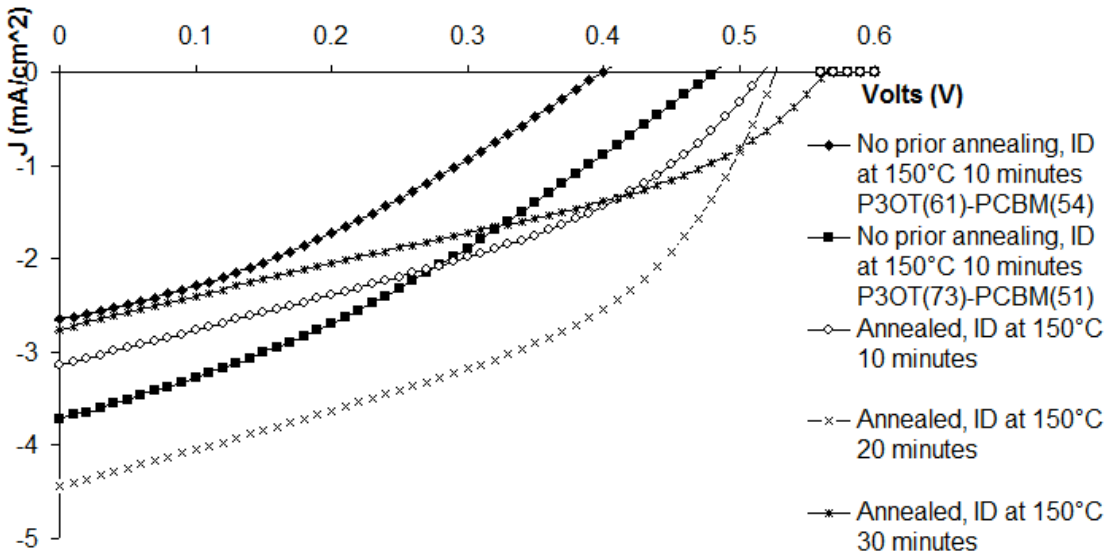

Figure 4.13 4th quadrant J-V characteristics for P3OT-PCBM devices interdiffused (ID) at 150 ºC for 10, 20 and 30 minutes under AM1.5G illumination.

It is evident from Figure 4.10 and 4.11 that the devices which are interdiffused at 150 °C for 20 minutes have the highest device performance which indicates that interdiffusion increases the interfacial area for charge transfer. However, the devices which are interdiffused beyond 20 minutes, there is a degradation in the device performance. In order to correlate the performance of the devices with the nanoscale control of the morphology, concentration gradient of the sulfur signal is studied as a function of the depth

In order to achieve the highest performance of the device, the concentration gradient should extend all the way across the film, ending right before the electrodes, so that the device has maximum interfacial area for the charge transfer and also has one kind of material at the electrodes. Figure 4.14 shows the expected concentration gradient curves for bilayer and interdiffused devices. Bilayer devices show a step in the sulfur signal since the top layer is pure fullerene (no sulfur) while the bottom layer is pure polymer (which contains sulfur). As charge transfer can only occur at the interface of the two layers, a quite small value of current is expected for bilayer devices. However, due to the presence of unobstructed pathways for the transport of charge carriers, the series resistance is expected to be fairly low.

However, for devices which are interdiffused by the ideal amount have a concentration gradient extending all the way through the device just ending right before the electrodes. These devices should have highest interfacial area for charge transfer and un-obstructed pathways for the charge transport. Hence, ideally interdiffused devices are expected to have highest short circuit current and lowest series resistance.

The devices which are highly interdiffused have a fairly homogeneous mixing of the polymer and fullerene. The photocurrent should be quite large since there is a donor/acceptor interface throughout the film. But the series resistance might be expected to be larger, since there is a smaller content of the material carrying the majority carrier at each respective electrode (holes at ITO and electrons at aluminum). These devices are expected to show decrease in the device performance due to the thermal degradation. Hence, in order to have the highest device performance, the concentration gradient of sulfur signal should be similar to the one achieved under ideal interdiffusion.

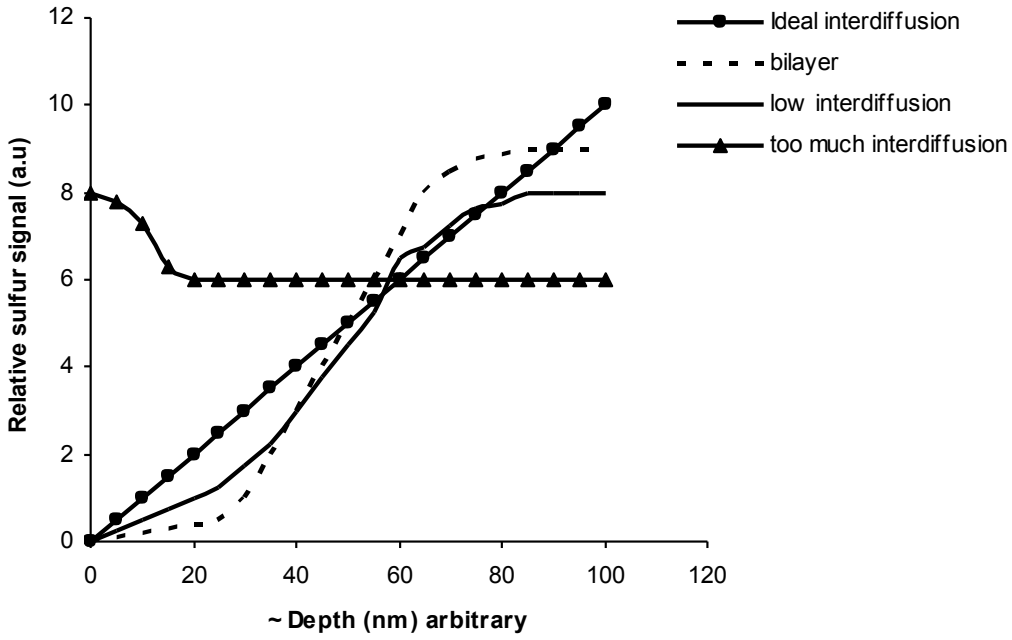

Figure 4.14 Plot of the expected concentration gradient of sulfur signals as a function of the depth for the device interdiffused under different conditions.

4.4 Studying the Concentration Gradient Profiles

The concentration gradient of the interdiffused devices was studied by using a 610 Perkin–Elmer scanning Auger spectroscopy system in combination with Ar-ion-beam milling as explained in Chapter 3. Since P3OT contains sulfur while PCBM does not, the sulfur signal indicates the relative amount of P3OT in the film as a function of depth. The absolute intensities of the sulfur signals vary from measurement to measurement depending on the settings and sensitivity of the apparatus. Hence, the intensity of the signals is meaningful only within each scan and the magnitudes of the different scans are arbitrary. Figure 4.15 shows the Auger spectroscopy depth profiles for a device that was not thermally interdiffused and devices interdiffused at 150 ºC for 10, 20, and 30 minutes. The device that was not thermally interdiffused indicates a fairly pure PCBM layer followed by a fairly pure P3OT layer with a gradient over roughly 20 nm in between.

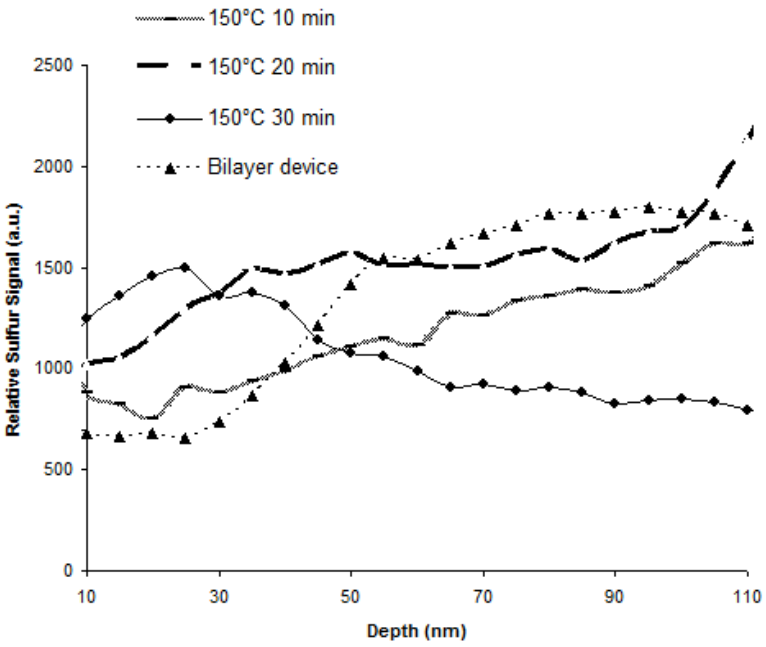

Figure 4.15 Auger spectroscopy depth profiles for P3OT-PCBM bilayer and interdiffused devices with interdiffusion carried out at 150 ºC for 10, 20 and 30 minutes.

The results of the Auger spectroscopy correlate fairly well with the performance of the devices. Concentration gradient profiles for the devices which are interdiffused at 150 °C for 10 and 20 minutes show an increasing gradient of sulfur (indicative of the presence of P3OT) as the device is scanned from the sulfur-free PCBM layer at the top to the sulfur-containing P3OT layer at the bottom. As the time of interdiffusion is increased further to 30 minutes, the concentration gradient tends to reverse which indicates that a high amount of polymer has moved to the surface and can lead to the degradation of the device performance. This is quite in agreement with the performance of the devices. As is evident from Table 4.6, there is an increase in the efficiency of the devices as the time of interdiffusion is increased from 10 to 20 minutes at 150 °C and beyond that there is degradation in the device performance. While this latter result suggests that the

surface energy is minimized when the polymer is at the surface, there are not any published results that allow comparison of the surface energies of P3OT and PCBM.

4.5 Summary of P3OT PCBM Devices

The performance of P3OT PCBM bulk heterojunction devices was studied by varying the active layer thickness and also by varying the annealing conditions. The devices with active layer thickness of 80 nm have better device performance than the device with active layer thickness of 50 nm or 110 nm. The devices with thickness of 110 nm have high series resistance so there is a drop in the performance. However, for devices with thickness ~ 50 nm, the active volume is quite small for efficient charge generation and hence there is a drop in performance. Furthermore, the thickness was maintained at 80 nm and the annealing conditions were varied to study the device performance. The devices that are annealed at 140 °C have better performance compared to the devices annealed at 130 °C or 150 °C. Also for the same thickness, increase of time of annealing from 5 minutes to 10 minutes, at 140 °C leads to degradation of device performance. The drop in the device performance as the annealing temperature and time are increased can be due to an increased intermixing of the two components which leads to the degradation in the transport properties.

Concentration gradient devices have been a success for P3OT PCBM system. A systematic study was done on the P3OT PCBM interdiffused devices and it was found that interdiffused devices have better performance than the bilayer devices. It was also concluded that annealing of the P3OT films before PCBM is spin cast, helps in increasing the crystallinity of the film and was not found to hinder the interdiffusion process. The devices which are interdiffused for 20 minutes at 150 ºC have the highest performance. The thickness, interdiffusion temperature and time of interdiffusion were the three parameters that were primarily studied for their effect

on the device performance. It was found that devices with 70 nm of P3OT and 40-50 nm of PCBM have better performance. Furthermore, the devices with 70 nm of P3OT and 40-50 nm of PCBM were interdiffused at 140 ºC and 150 ºC for various amounts of time. It was found that devices which are interdiffused for 20 minutes have better performance than the ones interdiffused for 10,30 and 40 minutes. Heat treatments done at higher temperature increase the interpenetrating network of polymer and fullerene and hence an increase in the efficiency of these devices. An AM1.5G power conversion efficiency of 1.0% was obtained for devices in which a 70 nm P3OT film is annealed at 120 ºC followed by spin-casting of 40-50 nm thick PCBM from pyridine and interdiffusion of the two films at 150 ºC for 20 minutes. The concentration gradient profiles obtained by Auger spectroscopy show that, for the devices with highest performance, gradients extend all the way just ending short of electrodes.

References

1. M. Kaur, A. Gopal , R.M. Davis , J.R. Heflin, "Concentration Gradient P3OT/PCBM Photovoltaic Devices Fabricated by Thermal Interdiffusion of Separately Spin-Cast Organic Layers", **Solar energy materials and solar cells,** 93, 1779-1784, (2009).

2. W. Ma, C. Yang, X. Gong, K. Lee, A.J. Heeger," Thermally Stable, Efficient Polymer Solar Cells with Nanoscale Control of the Interpenetrating Network Morphology", **Adv. Funct. Mater**. 15, 1617-1622, (2005).

3. M. Al-Ibrahim, H.-K. Roth, M. Schroedner, A. Konkin, U. Zhokhavets, G. Gobsch, P. Scharff, S. Sensfuss, "The Influence of the Optoelectronic Properties of Poly(3-Alkylthiophenes) on the Device Parameters in Flexible Polymer Solar Cells." **Org. Elec.** 6 , 65-77, (2005).

4. D. Gebeyehu, C.J. Brabec, F. Padinger, T. Fromherz, J.C. Hummelen, D. Badt, H. Schindler, N.S. Sariciftci, "Interplay of Efficiency and Morphology in Photovoltaic Devices Based on Interpenetrating Networks of Conjugated Polymers with Fullerenes", **Syn. Met**. 118, 1-9, (2001).

5. M. Drees, R.M. Davis, J.R. Heflin, "Improved Morphology of Polymer-Fullerene Photovoltaic Devices with Thermally-Induced Concentration Gradients" **J. Appl. Phys.** 97, 036103-036103-3, (2005).

6. M. Drees, K. Premaratne, W. Graupner, J.R. Heflin, R.M. Davis, D. Marciu, M. Miller, "Creation of a Gradient Polymer-Fullerene Interface in Photovoltaic Devices by Thermally Controlled Interdiffusion", **Applied Physics Letters** 81(24), 4607-4609 (2002).

7. Y. Kim *et al.*, "Device annealing effect in organic solar cells with blends of regioregular poly.3-hexylthiophene. and soluble fullerene", **Applied Physics Letters**, 86, 063502, (2005).

8. D. Chirvase, J. Parisi, J. C. Hummelen and V Dyakonov, "Influence of nanomorphology on the photovoltaic action of polymer–fullerene composites, **Nanotechnology**, 15 , 1317-1323 (2004).

Chapter 5

P3HT Donor and PCBM Acceptor

In this chapter, devices with P3HT as the donor and PCBM as the acceptor material are studied in detail. Different morphologies of device architecture such as bulk heterojunction, bilayer and thermally interdiffused devices are investigated at length. In bulk heterojunction devices, the thickness of the active layer and the annealing conditions are the two parameters that are studied. However, the focus of this chapter is on the bilayer and concentration gradient devices made with P3HT as donor and PCBM as acceptor. The parameters that are studied in detail for interdiffused devices are the thickness of each layer and interdiffusion conditions.

5.1 P3HT: PCBM Blends/Bulk Heterojunction

P3HT (poly (3-hexylthiophene)) was used in place of P3OT because of its higher hole mobility as well as due to its higher absorption coefficient. The bulk heterojunction or blend devices are the most common device architecture used for the synthesis of organic solar cell devices. Blend devices were made by dissolving the P3HT (Plextronics) and PCBM (Nano-C) in a 1:1 ratio in chlorobenzene to make a 3% wt/vol solution. 1" by 1" indium tin oxide (ITO) coated glass slides were spin-coated with poly (3,4-ethylenedioxythiophene): poly(styrenesulfonate) (PEDOT: PSS) complex (Bayer Corp.) at 1400 rpm. The P3HT: PCBM solution was spin cast onto the PEDOT: PSS-coated ITO substrate. The devices with the active layer were either annealed prior or post electrode deposition. Aluminum electrodes are deposited by the thermal evaporation under high vacuum.

5.1.1 Post Annealed P3HT: PCBM Blend Devices under Vacuum

P3HT: PCBM 3% wt/vol solutions was spin cast at varied spin speeds so as to vary the thickness of the active layer followed by thermal evaporation of the aluminum electrodes under high vacuum. The active layer thickness was calculated from the optical density measurements observed from Filmetrics. Figure 5.1 shows an example of the optical density plot of the separate layers of PEDOT and P3HT: PCBM. The thickness was calculated by using the absorption coefficient of 17.5x 10^4 cm^{-1} for P3HT and 2.5x10^4 cm^{-1} for PCBM at 512 nm.

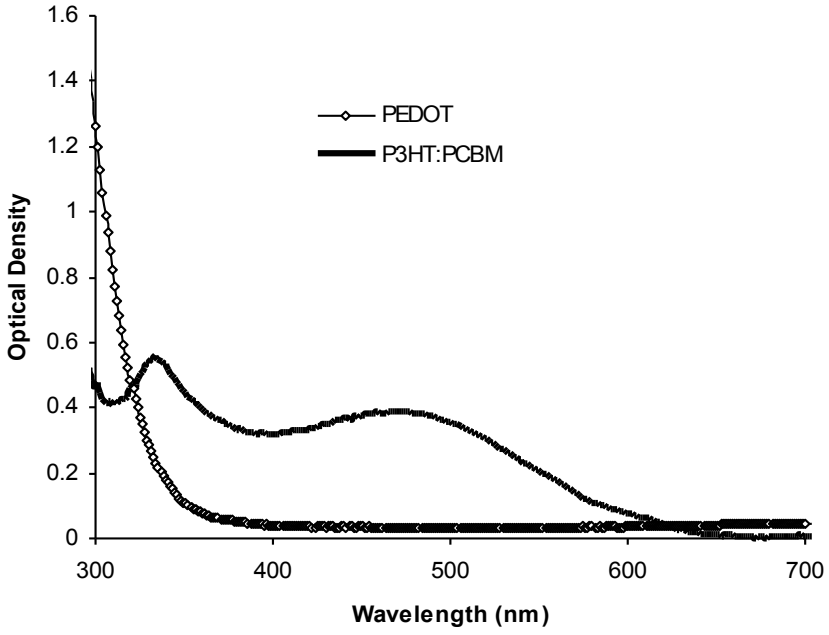

Figure 5.1 Optical density spectra of separate layers of PEDOT and P3HT: PCBM.

In these devices, annealing was done after the electrode deposition (post-annealing) under vacuum ($4x10^{-6}$ Torr). A 1" by 1" kapton heater was used to anneal the device, under vacuum ($4x10^{-6}$ Torr) to remove residual water and solvents and to increase the P3HT crystallinity for improved hole mobility. In these devices, the active layer thickness was maintained at 80-90 nm.

A. Effect of Variation of Annealing Conditions (Temperature and Time)

A very limited set of P3HT: PCBM blend devices were studied with annealing done under high vacuum. Annealing was done at 120 °C and 140 °C for varied amounts of time. Figure 5.2 shows the EQE spectra of the devices annealed at 120 °C and 140 °C for various amounts of time. It was found that as the time of annealing is increased beyond 10 minutes at 120 °C, there is a slight degradation in the performance of the devices. Also, with the increase of temperature of annealing from 120 °C to 140 °C, device performance decreases. It has been found that as the temperature and time of annealing is increased beyond T_g of the blend, increased intermixing of the two components leads to the degradation in the transport properties and hence can lead to the drop in the performance [10]. In all of the devices, the active layer was annealed after electrode deposition under vacuum. However, in most of these devices, there were some bursts or breaking of the aluminum electrodes films. It can be because of the rapid cooling of the devices when the annealing is done under vacuum conditions. Hence, this was not considered a preferred method of post-annealing.

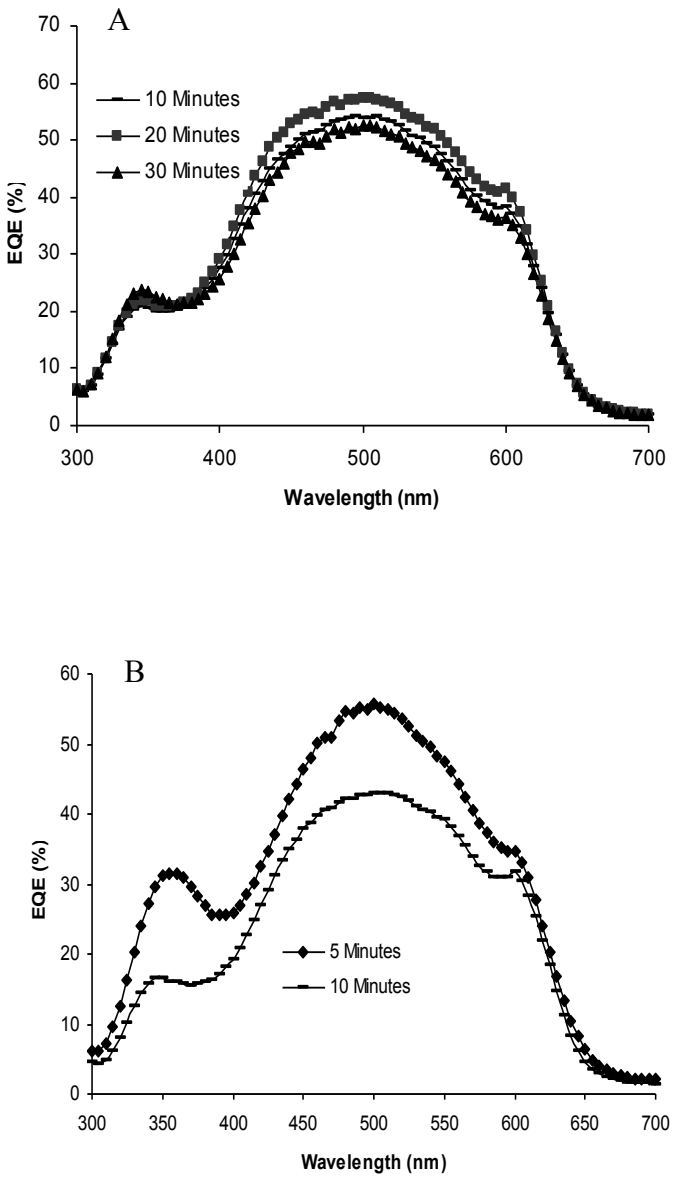

Figure 5.2 EQE plots of P3HT: PCBM blends annealed at 120 °C and 140 °C. Plot A shows EQE plots of devices annealed at 120 °C for 10, 20 and 30 minutes. Plot B shows the EQE plots of the devices annealed at 140 °C for 5 and 10 minutes.

Table 5.1 lists the efficiency, FF, V_{oc}, J_{sc}, RR, series and shunt resistance values obtained for the P3HT PCBM bulk heterojunction devices annealed under high vacuum, at 120 °C for 10, 20 and 30 minutes. As is evident, there is a decrease in the device efficiency as the time of post annealing is increased beyond 10 minutes. There is also an evident increase in series resistance as the annealing time is increased from 10 minutes to 30 minutes.

Table 5.1 Efficiency, FF, V_{oc}, J_{sc}, RR, series and shunt resistance values for devices post annealed at 120 °C for 10, 20 and 30 minutes under monochromatic and AM1.5G illuminations.

Post annealing conditions	120 °C 10 minutes	120 °C 20 minutes	120 °C 30 minutes
Efficiency 470 nm (%)	3.7	3.4	2.4
Efficiency AM1.5G (%)	1.1	0.65	0.4
FF 470 nm	0.49	0.43	0.32
FF AM1.5G	0.28	0.2	0.16
V_{oc} 470 nm (Volts)	0.425	0.415	0.415
V_{oc} AM1.5G (Volts)	0.565	0.565	0.565
J_{sc} 470 nm(mA/cm^2)	-0.66	-0.7	-0.6
J_{sc} AM1.5G (mA/cm^2)	-6.6	-5.8	-4.3
RR	51	60	309
Series resistance (Ω)	77	191	190
Shunt resistance (Ω)	1.00×10^6	2.8×10^5	1.20×10^6

Table 5.2 shows the efficiency, FF, V_{oc}, J_{sc}, RR, series resistance and shunt resistance values for the P3HT: PCBM bulk heterojunction devices post annealed at 140 °C for 5 and 10 minutes. There is a drastic decrease in the performance of the devices that are annealed for 10 minutes compared to 5 minutes at 140 °C. The rectification ratio of the devices annealed at 140 °C is much lower than for the devices annealed at 120 °C.

Table 5.2 Efficiency, FF, J_{sc}, $V_{oc,}$ RR, series and shunt resistance values under monochromatic lamp and AM1.5G lamp for devices post annealed at 140 °C for 5 and 10 minutes.

Post annealing conditions	140 °C/ 5 minutes	140 °C/ 10 minutes
Efficiency 470 nm (%)	2.5	1.85
Efficiency AM1.5G (%)	1.5	0.85
FF 470 nm	0.34	0.39
FF AM1.5G	0.34	0.25
V_{oc} 470 nm (Volts)	0.415	0.335
V_{oc} AM1.5G (Volts)	0.535	0.495
J_{sc} 470 nm(mA/cm^2)	-0.65	-0.53
J_{sc} AM1.5G (mA/cm^2)	-8.3	-6.92
RR	21	2.1
Series resistance (ohm)	66.4	119
Shunt resistance (ohm)	$1.1x10^5$	$9x10^4$

5.1.2 Pre-annealed P3HT: PCBM Blend Devices

- annealing is done on hot plate under continuous supply of argon

In these devices, the active layer is annealed on the hot plate described in Chapter 3. A P3HT: PCBM 3.0% wt/vol blend solution was made by co-dissolving P3HT (Rieke metals. Inc, 4002E) and PCBM (Nano-C) in 1:1 ratio in chlorobenzene. Annealing was done on a hot plate under the continuous flow of argon to remove residual water and solvents and to increase the P3HT crystallinity for improved hole mobility followed by the electrode deposition [12]. Some of the blend devices were fabricated without any annealing and it was found that annealed devices have better performance to the non-annealed devices which can be due to the increased hole mobility, conductivity and absorption spectrum range. Figure 5.3 shows the optical density spectra for annealed and non-annealed devices. Here, annealing was done at 140 °C for 5 minutes. It was found that in annealed devices, the absorption spectrum shifts towards the longer wavelengths allowing absorption of photons in that wavelength regime. Also, there is no degradation in the signal of the optical density after annealing indicating there is no photo-degradation in the devices. The thickness was calculated by using the absorption coefficient of 17.5x 10^4 cm^{-1} for P3HT and 2.5x10^4 cm^{-1} for PCBM at 512 nm. In all of these devices, active area thickness was maintained at 90 nm.

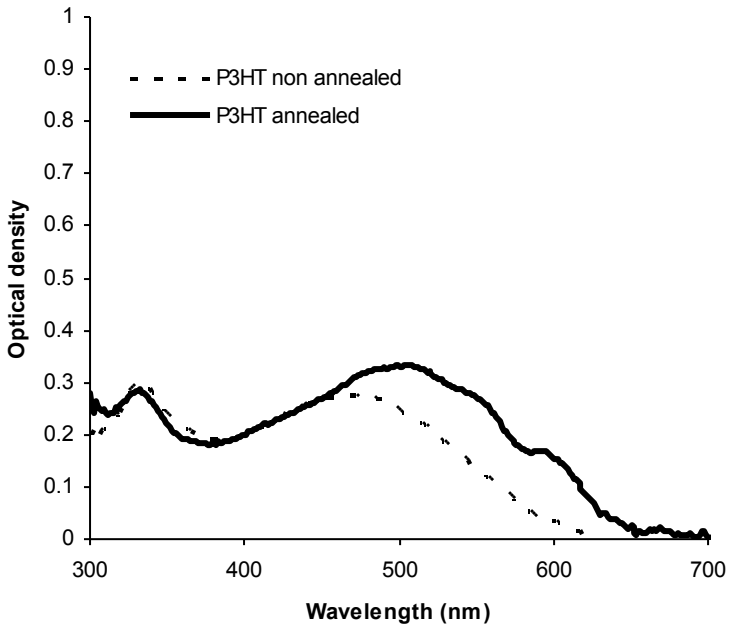

Figure 5.3 Optical density spectra of non-annealed and annealed P3HT:PCBM blend devices.

A. Effect of Variation of Annealing Conditions (Temperature and Time)

P3HT: PCBM blend devices were studied with and without annealing. Here annealing was done on hot plate under the continuous supply of argon. Annealing was done at 110 °C, 120 °C, 130 °C, 140 °C and 150 °C for varied amounts of time. It has been found that device performance of annealed devices were better than the non-annealed devices (0.4% under simulated AM 1.5). The better performance of the annealed devices can be attributed to the increased crystallinity in the P3HT as a result of annealing [12] and due to the formation of crystalline PCBM clusters [11]. It has also been found that as the temperature of annealing increased beyond 110 °C, there is degradation in device performance. Also for a particular temperature, increasing the time of annealing beyond 5 minutes, leads to the degradation in

device performance. Figure 5.4 shows the EQE plots of the P3HT: PCBM blend devices annealed for 5 and 10 minutes at 110 °C, 120 °C, 130 °C, 140 °C and 150 °C. It is evident from Figure 5.4 that EQE of the devices is not significantly different for the annealing done for 5 and 10 minutes at a particular temperature and in some cases, EQE of the devices annealed for 10 minutes is better than the devices annealed for 5 minutes. However, it is evident from Table 5.3 that as the time of annealing is increased from 5 to 10 minutes at a particular temperature; there is degradation in the overall device efficiency and also as the temperature is increased beyond 110 °C, there is degradation in the overall device efficiency. Table 5.3 shows the efficiency values under monochromatic 470 nm lamp and AM1.5G lamp. It is evident from this that as the time of annealing is increased beyond 5 minutes at a particular temperature; there is degradation in the device performance.

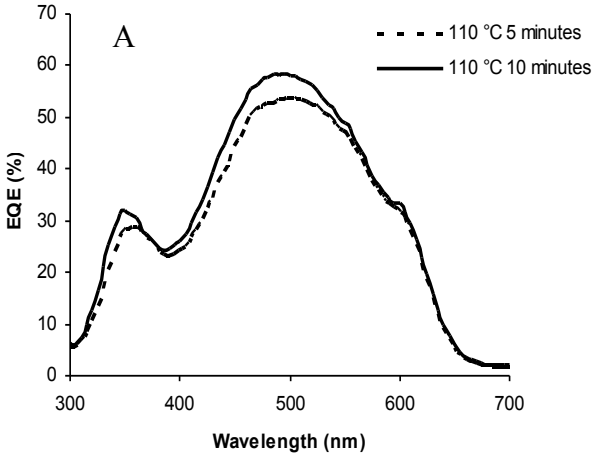
A
110 °C 5 minutes
110 °C 10 minutes
EQE (%)
Wavelength (nm)
0
10
20
30
40
50
60
70
300
400
500
600
700

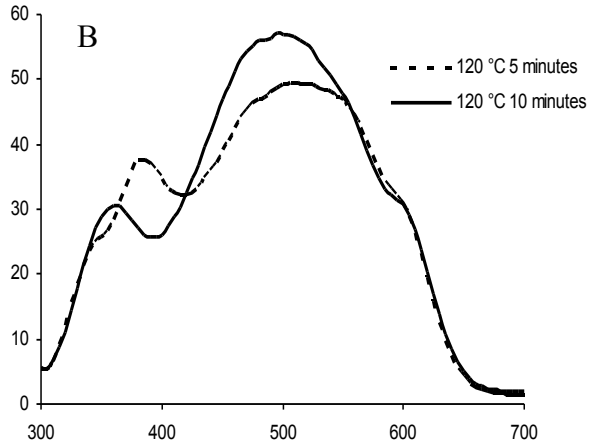
B
120 °C 5 minutes
120 °C 10 minutes
0
10
20
30
40
50
60
300
400
500
600
700

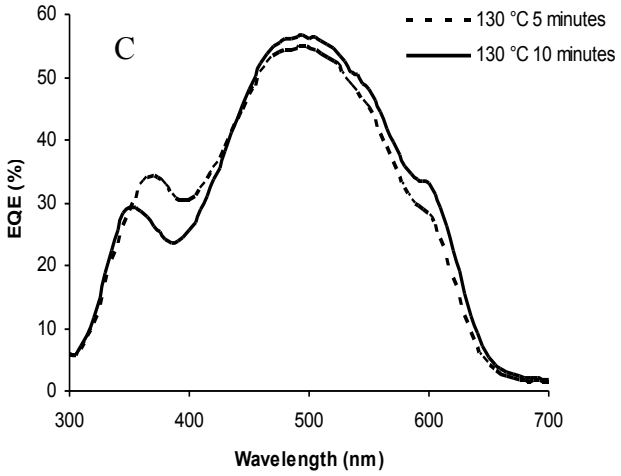
C
130 °C 5 minutes
130 °C 10 minutes
EQE (%)
Wavelength (nm)
0
10
20
30
40
50
60
300
400
500
600
700

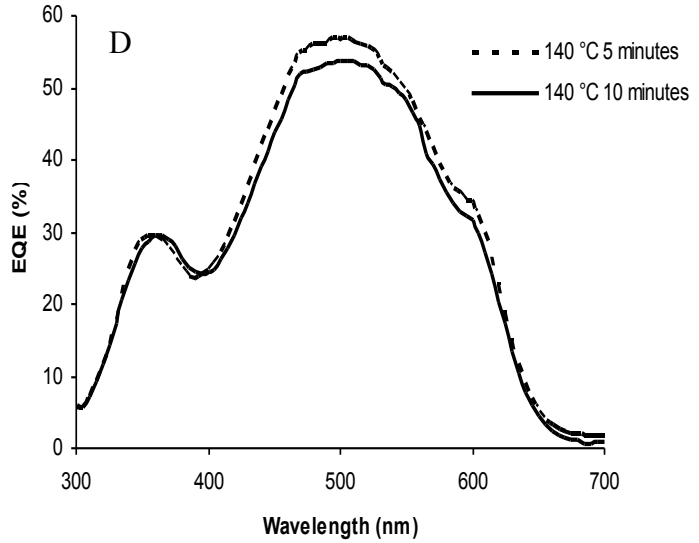

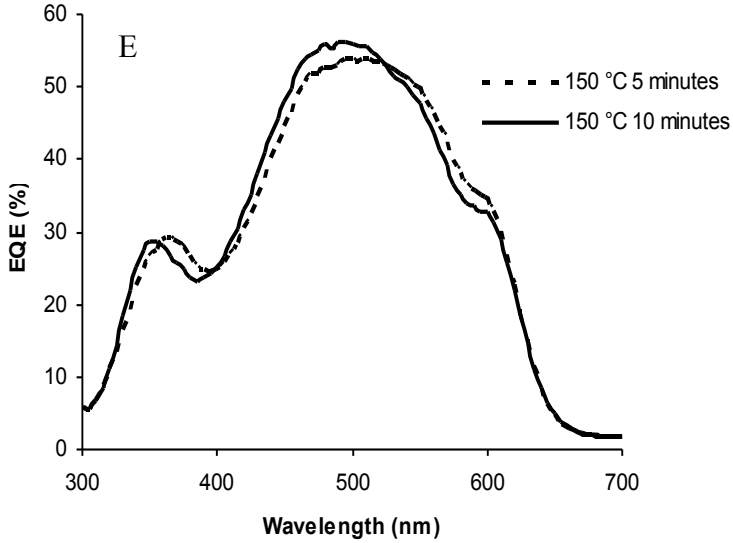

Figure 5.4 EQE plots of P3HT: PCBM blends. EQE plots of devices annealed for 5 and 10 minutes a (A) 110 °C, (B) 120 °C, (C) 130 °C, (D) 140 °C and (E) 150 °C.

Table 5.3 Efficiency values under monochromatic lamp (470 nm) and AM1.5G lamp for devices annealed at 110 °C, 120 °C, 130 °C, 140 °C and 150 °C for 5, 10 and 15 minutes.

Pre annealing temperature (°C)	Efficiency % under	5 minutes	10 minutes	15 minutes
110	AM1.5	3.3	2.2	2.1
	470 nm	5.6	6	5.3
120	AM1.5	2.7	2.3	1.2
	470 nm	5	6.6	4
130	AM1.5	2.1	1.84	1.6
	470 nm	6	6	5
140	AM 1.5	2.1	1.8	1.5
	470 nm	6	4	5.2
150	AM 1.5	1.1	1.7	NA
	470 nm	4.1	4.8	NA

As shown in Table 5.3, there is a drop in device efficiency from 3.3% to 1.1% under AM1.5G illumination as the temperature of annealing is increased from 110 °C to 150 °C for 5 minutes annealing time. Also, with the increase in the time of annealing at a particular temperature, there is a decrease in the efficiency of the devices. The devices which are pre-annealed at 110 °C for 5 minutes have been found to have the best device performance (~3.3% under AM1.5G illumination). Figure 5.5 shows the 4^{th} quadrant J-V characteristics for the P3HT: PCBM devices which are pre-annealed at various temperatures. In each plot, the time of

annealing is increased from 5 to 15 minutes. As is evident, there is a decrease in the V_{oc} and FF of the devices as the time of annealing is increased at a given temperature. The increase in time of annealing as well as annealing beyond the T_g of the blend leads to the increased intermixing of the two components and hence degradation in the transport properties and device performance [10]. Also, it has been found that crystallinity of P3HT and PCBM increases with annealing. Annealing acts as the driving force for the formation of PCBM clusters which are crystalline in nature and hence better performance of the annealed devices to the non-annealed devices. However, annealing for longer period of time or at higher temperatures leads to the formation of voluminous PCBM clusters that can damage the absorber-metal interface and hence degradation in the device performance [11].

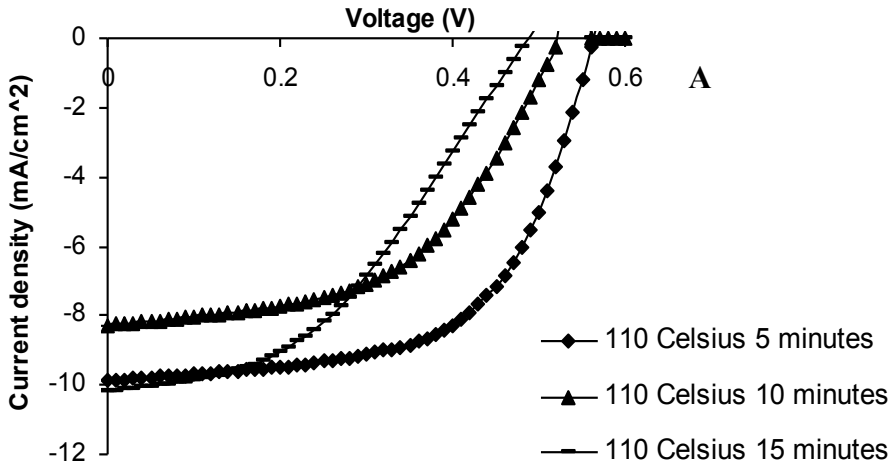
Voltage (V)
0
0.2
0.4
0.6
Current density (mA/cm^2)
0
-2
-4
-6
-8
-10
-12
110 Celsius 5 minutes
110 Celsius 10 minutes
110 Celsius 15 minutes

A

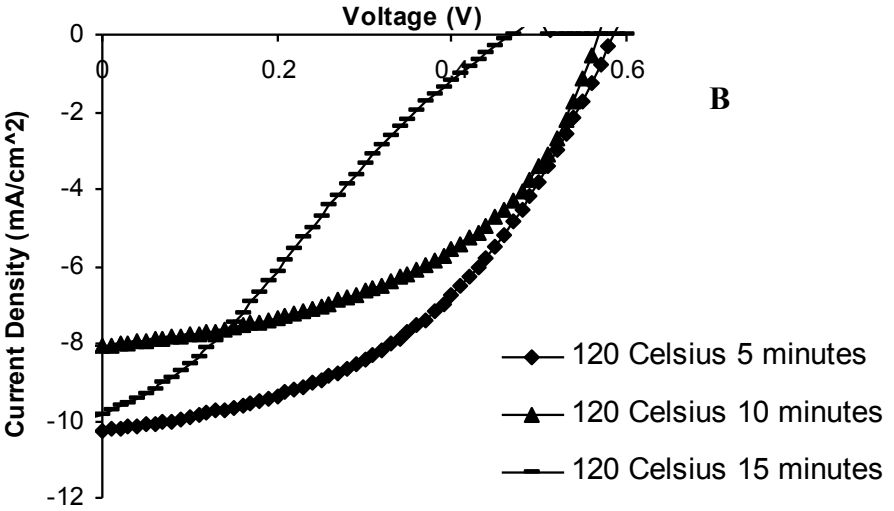
Voltage (V)
0
0.2
0.4
0.6
Current Density (mA/cm^2)
0
-2
-4
-6
-8
-10
-12
120 Celsius 5 minutes
120 Celsius 10 minutes
120 Celsius 15 minutes

B

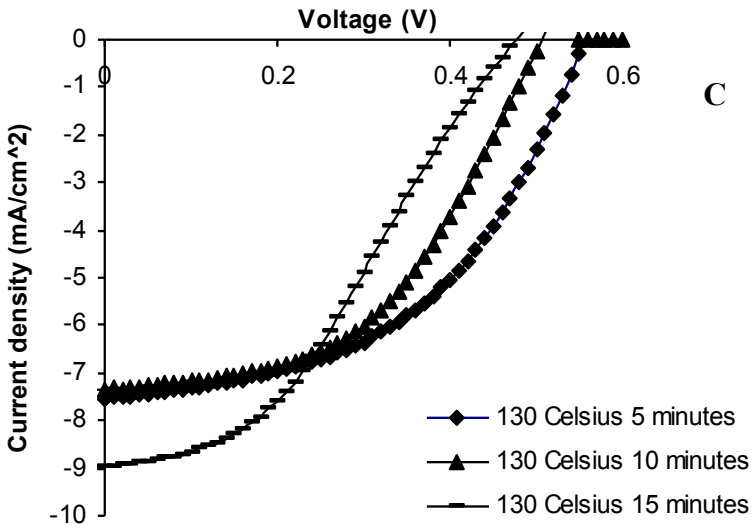

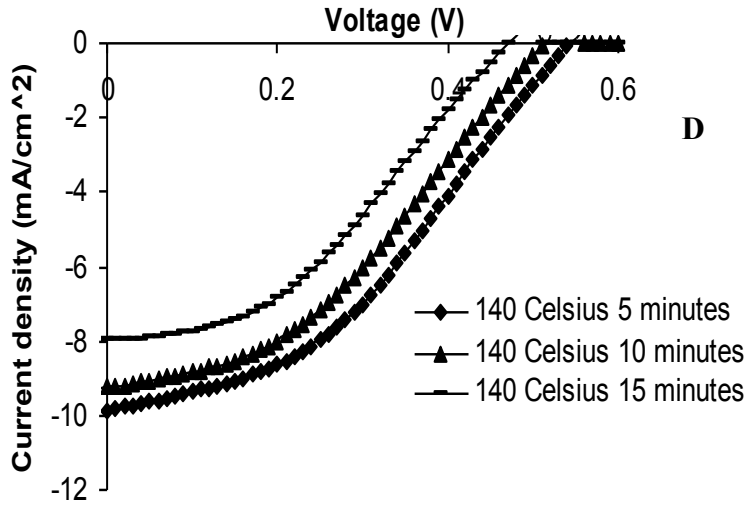

Figure 5.5 AM1.5 illumination 4th quadrant J-V characteristics for P3HT: PCBM blends annealed at (A) 110 °C, (B) 120 °C, (C) 130 °C and (D) 140 °C for 5, 10 and 15 minutes

This trend of the decrease in the device performance as the time of annealing is increased is present for the devices which are either annealed under the continuous supply of argon or

which are annealed in high vacuum conditions. Figure 5.6 shows the 4th quadrant J-V characteristics under AM1.5 illumination for devices which are annealed at 110 °C, 120 °C, 130 °C, 140 °C and 150 °C for 5 minutes. There is degradation in the device performance as the temperature of annealing is increased from 110 °C to 150 °C. As evident from Figure 5.6, there is drastic decrease in the V_{oc} and FF values as the temperature of annealing is increased beyond 110 °C.

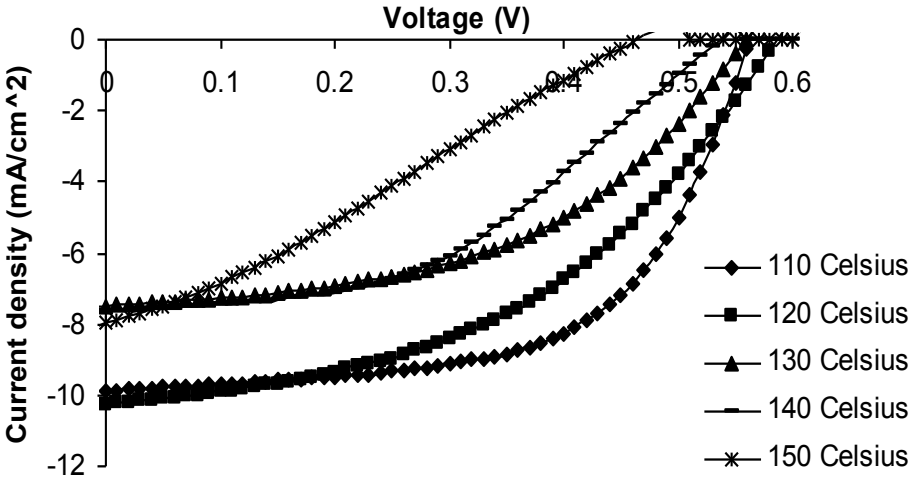

Figure 5.6 AM1.5 illumination 4th quadrant J-V characteristics for P3HT: PCBM blends annealed at 110 °C, 120 °C, 130 °C, 140 °C and 150 °C for 5 minutes

Table 5.4 gives the V_{oc}, FF and series resistance values for the pre annealed devices.

Table 5.4 V_{oc}, FF, series resistance values for P3HT: PCBM blends pre annealed at 110 °C, 120 °C, 130 °C and 140 °C for 5 and 15 minutes.

Pre annealing conditions	V_{oc} (AM1.5G)	FF (AM1.5G)	Series resistance (Ω)
110 °C/ 5 minutes	0.565	0.59	30
110 °C/ 15 minutes	0.425	0.43	46
120 °C/ 5 minutes	0.585	0.46	34
120 °C/ 15 minutes	0.465	0.27	60
130 °C/ 5 minutes	0.555	0.49	68
130 °C/ 15 minutes	0.475	0.38	49
140 °C/ 5 minutes	0.535	0.42	30
140 °C/ 15 minutes	0.475	0.40	43

As evident from Table 5.4, there is a drop in the FF and V_{oc} of the devices as the time of annealing is increased from 5 to 15 minutes at a given temperature. The devices which are annealed at 110 °C for 5 minutes have the FF value of the order of 0.6 under AM1.5G illuminations. The series resistances of the devices which are annealed for 5 minutes have the lowest series resistance and hence better device performance. With the increase in the time of annealing, polymers and PCBM tend to form clusters and hence offer the resistance to the charge propagation [11].

5.2 P3HT PCBM Concentration Gradient Interdiffused Devices

P3HT/PCBM concentration gradient devices are based on the same concept as for the P3OT /PCBM devices. The interdiffused device morphology provides enhanced interfacial area for the charge transfer compared to the bilayer devices and provide uninterrupted charge transport compared to the blend devices. This new approach is developed and studied extensively in this thesis. P3HT (Rieke Metals Inc (4002E), Plextronics. Inc (OS1100)/ PCBM (Nano-C) interdiffused devices are made by the dual spin casting process, similar to the process described for P3OT/PCBM devices. In the first set of experiments on P3HT/PCBM interdiffused devices, P3HT from Rieke metals (4002 E) was used which was replaced by P3HT from Plextronics (OS 1100) in the later set of experiments. The dual spin cast bilayer devices are further interdiffused at different temperatures for varied amounts of time so as to study the effect of heat treatment on the device performance. Here, pyridine is used as the solvent for PCBM as it dissolves PCBM fairly well and does not wash off P3HT. P3HT has been found to dissolve fairly well in chlorobenzene and 1,2 dichlorobenzene relative to chloroform. Hence, chlorobenzene or 1,2 dichlorobenzene is chosen as the solvent for P3HT. Heat treatment of these devices is either done in the vacuum by using the 1" by 1" kapton heater under high vacuum or by using the hot plate in argon box.

5.2.1 Interdiffused Devices with Heat Treatment under High Vacuum

Indium tin oxide (ITO) coated glass slides were spin-coated with poly (3,4-ethylenedioxythiophene): poly(styrenesulfonate) (PEDOT: PSS) complex (Bayer Corp.) at 1400 rpm. P3HT (Rieke Metals,Inc.) was spin-coated from 1.5% wt/vol solution in chlorobenzene (CB) at 1500 rpm followed by annealing of the device at 140 ºC for 10 minutes. Annealing was

done under vacuum ($4x10^{-6}$ Torr) to remove residual water and solvents and to increase the P3HT crystallinity for improved hole mobility. PCBM was then spin cast from a 2.0% wt/vol solution in pyridine. Interdiffusion is done after spin casting the PCBM layer followed by the electrode deposition. Here, annealing as well as interdiffusion is done under vacuum. In earlier experiments, the thickness of P3HT was maintained at 65 nm, however the thickness of PCBM was varied from 40 to 140 nm by changing the spin speeds. In this set of experiments, annealing and interdiffusion were maintained at constant conditions while varying the thickness of the PCBM layer. Annealing was done at the 140 °C for 10 minutes and interdiffusion was done at 150 °C for 10 minutes. The thickness of P3HT and PCBM films was determined from the optical density obtained from reflection and transmission measurements with a Filmetrics F20-UV thin film spectrometer system. The absorption coefficient used for P3HT is 17.5×10^4 cm^{-1} at 512 nm and for PCBM is 2×10^4 cm^{-1} at 512 nm.

Photocurrent spectra were measured using a 300 W Xe lamp in combination with a CVI CM 100 monochromator as the illumination source and a Keithley 485 picoammeter to record the short circuit currents I_{sc}. Photoresponsivity (*PR*) and EQE can be evaluated from photocurrent measurements as described in Chapter 3. In addition to measurements under monochromatic illumination, measurements were also taken under simulated AM1.5G solar spectrum as described in Chapter 3.

Figure 5.7 Shows the EQE spectra of P3HT-PCBM devices interdiffused at 150 °C for 10 minutes with varied thickness. The devices with thickness of the order P3HT (65)-PCBM (50) had the highest efficiency. As the thickness of the PCBM is increased from 40 nm to 55 nm, there is an improvement in the device performance. However, with the increase in the thickness of PCBM beyond 55 nm, there is degradation in the device performance at this interdiffusion

condition. With the increase in PCBM thickness beyond 55 nm, the interdiffusion done at 150 °C for 10 minutes does not increase the interfacial area for the charge transfer and there is an increase in the series resistance which can lead to the degradation in the device performance. The cause of these effects is believed to be that as the PCBM thickness is increased, the interdiffusion does not extend to the end of PCBM film. Thus, there is a large region of PCBM that is not utilized in the charge transfer process but adds to the series resistance.

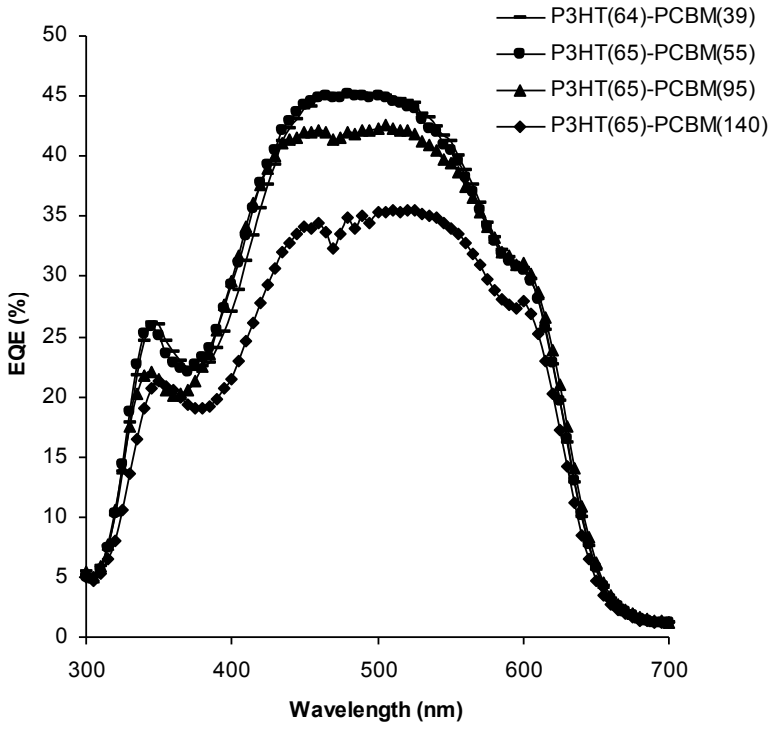

Figure 5.7 EQE spectra of the P3HT/PCBM interdiffused devices with varied PCBM thickness. Interdiffusion is done at 150 °C for 10 minutes.

Table 5.5 shows the efficiency, FF, V_{oc}, J_{sc}, RR, series resistance and shunt resistance values for P3HT-PCBM interdiffused devices. All of these devices were interdiffused at 150 °C for 10 minutes. In these devices P3HT thickness was maintained at 65 nm however PCBM thickness was varied from 40 to 140 nm. As is evident from Table 5.5, the RR is higher for devices with PCBM thickness of 55 nm. However the devices with PCBM thickness 40 nm, 95 nm and 140 nm have much lower RR and it supports the efficiency results obtained for these devices.

Table 5.5 Efficiency, FF, V_{oc}, J_{sc}, RR, series and shunt resistance of P3HT/PCBM interdiffused devices with varied PCBM thickness.

PCBM thickness (nm)	40 nm	55 nm	95 nm	140 nm
Efficiency 470 nm (%)	2.8	3.8	2.1	1.4
Efficiency AM1.5 (%)	0.77	2.0	0.58	0.3
FF 470 nm	0.42	0.59	0.39	0.26
FF AM1.5	0.25	0.46	0.22	0.18
V_{oc} 470 nm (Volts)	0.435	0.425	0.395	0.435
V_{oc} AM1.5 (Volts)	0.565	0.565	0.565	0.595
J_{sc} 470 nm (mA/cm^2)	0.589	0.57	0.52	0.335
J_{sc} AM 1.5 (mA/cm^2)	5.54	7.74	4.66	1.35
RR	260	6449	221	229
Series resistance (Ω)	65.2	22.7	84.7	145
Shunt resistance (Ω)	4.95×10^5	1.6×10^6	2.84×10^5	1.1×10^6

The values of series and shunt resistance values as shown in Table 5.2 also support the efficiency values obtained for these devices. The device with the highest efficiency has the lowest series resistance and highest shunt resistance. However as the thickness of PCBM is increased beyond 55 nm, there is an increase in the series resistance as expected. It is also interesting to note that, comparing the 40 nm and 55 nm devices, they have similar J_{sc} and V_{oc} but the FF is significantly larger in the 55 nm thickness case. This is most likely due to a concentration gradient that extends across the entire film without having pileup of the P3HT at the aluminum surface and thus resulting in better electrical characteristics.

5.2.2 Interdiffused Devices with Heat Treatment done under Continuous flow of Argon

In this set of experiments, annealing as well as interdiffusion was carried out on the hot plate under the continuous flow of argon. A series of experiments were done under these conditions to study the P3HT/PCBM interdiffused devices. P3HT and PCBM were obtained from Plextronics and Nano-C, respectively, and were used without further purification. Interdiffusion was carried out at different temperatures in order to obtain concentration gradients in the initial bilayer of P3HT/ PCBM. Devices with thickness (45-40) nm each layer were studied in particular and interdiffusion was done at various temperatures and for varied periods of time in order to obtain concentration gradient. For these devices, interdiffusion done for 20 minutes has been found to show the maximum efficiency. The ideal interdiffusion time is dependent on the thickness of the device. The thickness and interdiffusion conditions were optimized to achieve the best performance of the devices. An AM1.5 efficiency of the order of ~3.0% has been obtained with this structure of devices. Auger spectroscopy and XPS studies were done to support the evidence of concentration gradient.

Indium tin oxide (ITO) coated glass slides were spin-coated with poly (3,4-ethylenedioxythiophene): poly(styrenesulfonate) (PEDOT: PSS) complex (Bayer Corp.) at 1400 rpm. PEDOT:PSS has a high electrical conductivity in the range of 400-600 S/cm and high optical transparency [9]. P3HT (Plextronics.) was spin-coated from 1.0% wt/vol solution in ortho-dichlorobenzene (ODCB) at 1200 rpm followed by annealing of the device at 120 ºC for 10 minutes. Annealing was done on the calibrated hot plate under the continuous supply of argon to remove residual water and solvents and to increase the P3HT crystallinity for improved mobility of hole carriers. PCBM was then spin cast from a 1.5% wt/vol solution in pyridine. Interdiffusion was done after spin casting the PCBM layer followed by the electrode deposition. Here, annealing as well as interdiffusion was done under the continuous supply of argon on the hot plate. Aluminum cathodes were then thermally evaporated onto the film after interdiffusion was complete. Figure 5.8 shows the architecture of P3HT/PCBM interdiffused device.

The thickness of the P3HT and PCBM films was determined from the optical density obtained from reflection and transmission measurements with the Filmetrics F20-UV thin film spectrometer system. The absorption coefficient used for P3HT is 17.5×10^4 at 512 nm and for PCBM is 17×10^4 at 350 nm. In earlier experiments, the thickness of P3HT was maintained at 45 nm, however, the thickness of PCBM was varied from 30 to 50 nm in this set of experiments by changing the spin speeds. Interdiffusion of the bilayer devices was done at different temperatures for varied amounts of time.

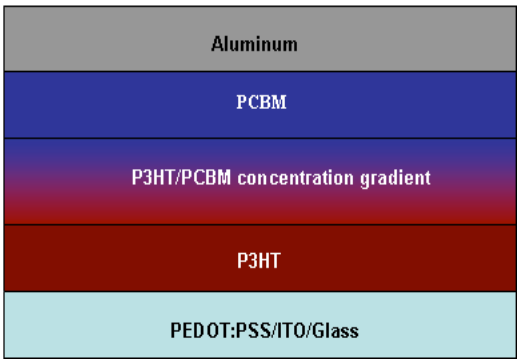

Figure 5.8 Architecture of the P3HT/PCBM interdiffused device.

Photocurrent spectra were measured using a 300 W Xe lamp in combination with a CVI CM 100 monochromator as the illumination source and a Keithley 485 picoammeter to record the short circuit currents (I_{sc}). Photoresponsivity (*PR*) and EQE were evaluated from the I_{sc} values recorded. Measurements were also taken under simulated AM1.5G solar spectrum. The AM1.5G solar spectrum was set to an intensity of 100 mW/cm^2 (1 sun) using a calibrated silicon photodiode and the results were uncorrected for spectral mismatch. Concentration gradient in P3HT/PCBM interdiffused devices was also studied by using 610 Perkin–Elmer scanning Auger spectroscopy system in combination with Ar-ion-beam milling. In this system, the surface layer of a film can be tested for its atomic constituents. After the Auger scan, the surface layer is milled off with an Ar-ion beam, and the new surface layer can be tested.

P3HT is annealed at 120 °C for 10 minutes on the hot plate under the continuous supply of argon, prior to the spin casting the PCBM layer. The interdiffusion conditions are varied to study its effect on the performance of the devices.

A. Effect of Variation of Interdiffusion Conditions (Temperature and Time)

Interdiffusion temperature and time are the major factors that effect dual Spin cast P3HT-PCBM devices as it will determine the extent of interdiffusion in the two layers. Here, in this study, interdiffusion was done at 120 °C, 130 °C, 140 °C, 150 °C and 160 °C for varied amounts of time for the devices with varied thickness of P3HT-PCBM. The best device performance is achieved for the devices interdiffused at 150 °C for 20 minutes. This is evident from the EQE plots of the P3HT/PCBM devices in Figure 5.9.

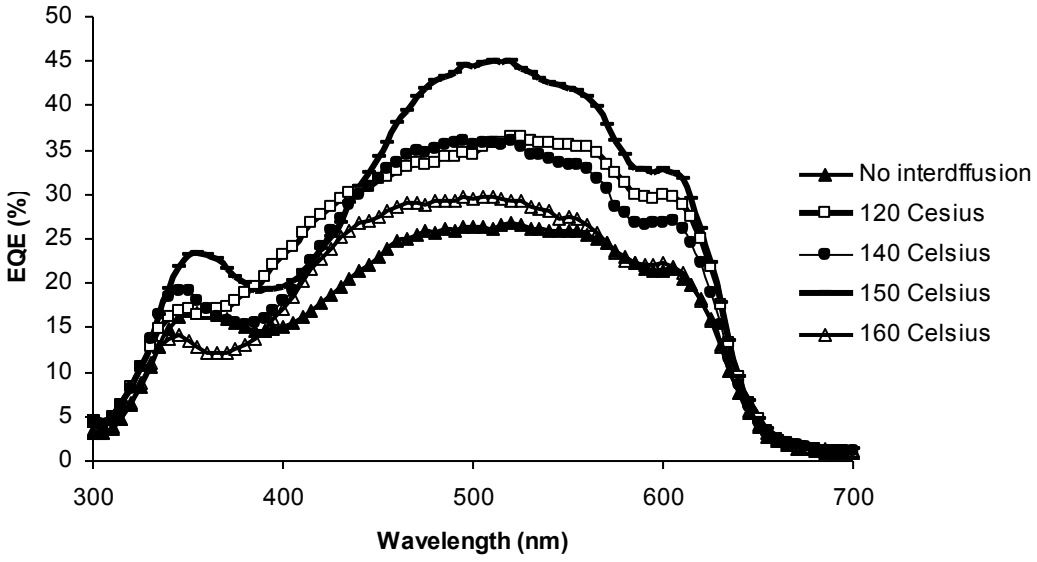

Figure 5.9 EQE spectra of P3HT/PCBM devices bilayer and interdiffused. Here, interdiffusion is done at 120 °C, 140 °C, 150 °C and 160 °C for 20 minutes

Figure 5.9 shows the EQE spectra of a bilayer device and the devices interdiffused at different temperatures. The time of interdiffusion was maintained at 20 minutes for these devices and in these devices thickness of the devices was maintained at 45(P3HT)/40 (PCBM). There is an evident increase in EQE for interdiffused devices compared to the bilayer device. As the temperature of interdiffusion is increased from 120 °C to 150 °C, there is a pronounced increase in the EQE values and then there is a sudden drop in the performance as the temperature is increased further to 160 °C.

Table 5.6 shows the efficiency, FF, V_{oc}, J_{sc}, RR, series and shunt resistance for the bilayer as well as interdiffused devices. The interdiffused devices are heated under the continuous supply of argon at 120 °C, 130 °C, 140 °C, 150 °C and 160 °C for 20 minutes. As is evident from Table 5.6, there is a consistent increase in the AM1.5 efficiency of the interdiffused devices compared to the bilayer devices. The device performance becomes better as the temperature of the interdiffusion is increased, up to the case of devices interdiffused at 150 °C for 20 minutes. As the temperature of interdiffusion is increased beyond 150 °C, there is a decrease in the device efficiency. The rectification ratio is highest for bilayer devices and there is drastic decrease in the RR values for the interdiffused devices. This is as expected, since the bilayer is more representative of the conventional p-n junction.

Table 5.6 Efficiency, FF, V_{oc}, J_{sc}, RR, series and shunt resistance values under 470 nm and AM1.5 illuminations for bilayer and interdiffused devices where the interdiffusion is done at different temperatures for 20 minutes.

	Bilayer	ID 120 °C 20 minutes	ID 130 °C 20 minutes	140 °C 20 minutes	150 °C 20 minutes	160 °C 20 minutes
Efficiency 470 nm (%)	1.5	3.1	4.1	3.7	4.2	3.0
Efficiency AM1.5 (%)	0.35	1.8	2.0	2.1	2.7	2.1
FF 470 nm	0.48	0.59	0.59	0.64	0.62	0.59
FF AM1.5	0.31	0.49	0.45	0.47	0.43	0.48
V_{OC} 470 nm (V)	0.345	0.415	0.435	0.435	0.435	0.455
V_{OC} AM1.5 (V)	0.495	0.545	0.535	0.575	0.555	0.605
J_{SC} (mA/cm^2) 470nm	-0.32	-0.43	-0.54	-0.45	-0.53	-0.38
J_{SC} (mA/cm^2) AM1.5	-2.3	-6.63	-8.35	-7.37	-11.1	-7.54
RR	11149	3437	1479	3171	1663	2215
Series (ohm) resistance	25.3	37.3	43.3	42.3	42	37.9
Shunt (ohm) resistance	2.7×10^6	8.4×10^5	3.84×10^5	1.1×10^6	5.1×10^5	5.27×10^5

Figure 5.10 shows the plot of efficiency under AM1.5G solar spectrum versus temperature of interdiffusion for a set of devices interdiffused for 10, 20 and 30 minutes. In this set of devices, the P3HT thickness was maintained at 45 nm and the PCBM thickness was kept 40-45 nm. The plot shows that at all temperatures, the device performance becomes better as the time of interdiffusion is increased from 10 to 20 minutes at a particular temperature and then as the time of interdiffusion is increased to 30 minutes, there is degradation in the device performance. Hence, the best performance is achieved when the interdiffusion is done for 20 minutes at a particular temperature. As the temperature of the interdiffusion is increased from 120 °C to 160 °C in steps of 10 °C, there is a consistent increase in the efficiency till the 150 °C is attained and then there is a drop in the performance of the devices interdiffused at 160 °C.

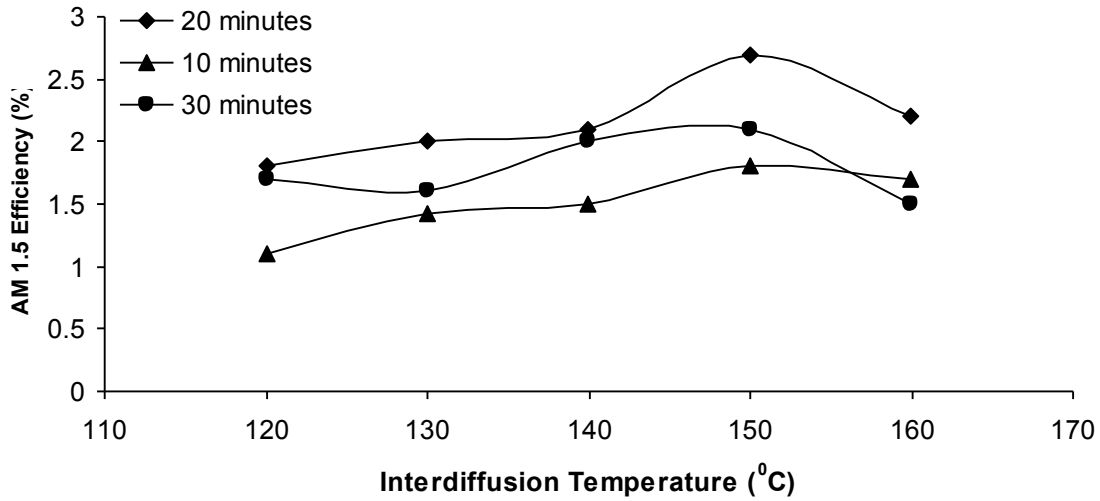

Figure 5.10 AM1.5 efficiency as a function of interdiffusion temperature for 10, 20 and 30 minutes. The temperatures studied are 120 °C, 130 °C, 140 °C, 150 °C and 160 °C.

Figure 5.11 shows the J-V curves under AM1.5 illumination for the devices interdiffused at 120 °C, 130 °C, 140 °C, 150 °C and 160 °C for 20 minutes. The J-V curve shows that there is pronounced increase in the J_{sc} value of the devices interdiffused at 150 °C for 20 minutes. There is degradation in the FF values as the devices are interdiffused at a temperature beyond 150 °C.

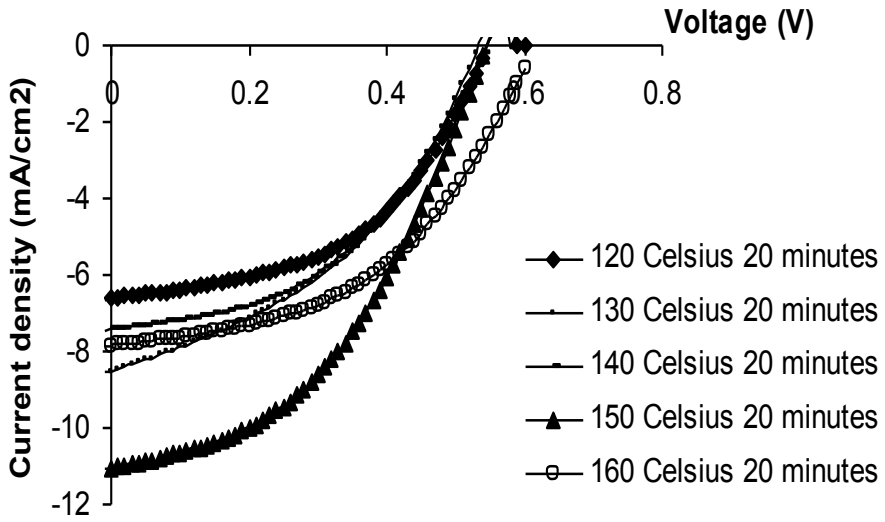

Figure 5.11 AM1.5G illumination 4th quadrant J-V characteristics for P3HT-PCBM devices interdiffused at 120 ºC, 130 ºC, 140 ºC, 150 ºC and 160 ºC for 20 minutes.

Table 5.7 shows the power conversion efficiency, fill factor (FF), V_{oc} and J_{sc} of the P3HT-PCBM interdiffused devices under monochromatic (470 nm) as well as AM 1.5 illuminations for the interdiffusion done for varied periods of time at 150 °C. In these devices, the thickness is maintained at 45 nm of P3HT and 40-45 nm of PCBM.

Table 5.7 Power conversion efficiency, FF, V_{oc}, J_{sc}, RR, series and shunt resistance values under monochromatic and AM 1.5 illuminations for devices interdiffused at 150 °C for varying time intervals.

Interdiffusion Time	10 minutes	20 minutes	30 minutes
Efficiency 470 nm (%)	4.4	4.2	4.1
Efficiency AM1.5G (%)	1.8	2.7	2.1
FF 470 nm	0.63	0.62	0.63
FF AM 1.5G	0.45	0.43	0.45
V_{oc} 470nm (Volts)	0.445	0.435	0.445
V_{oc} AM1.5G (Volts)	0.555	0.555	0.555
J_{sc} 470 nm (mA/cm^2)	-0.52	-0.53	-0.43
J_{sc} AM 1.5G (mA/cm^2)	-7.3	-11.1	-8.3
RR	2667	1663	2116
Series resistance (ohm)	73	42	48
Shunt resistance (ohm)	1.4×10^6	5.1×10^5	8.85×10^5

As the time of interdiffusion is increased from 10 minutes to 20 minutes at 150 °C, there is an increase in the device efficiency. Efficiency of the order of 2.7% for AM1.5 illumination is achieved for devices interdiffused at 150 °C for 20 minutes. The current densities of the devices interdiffused at 150 °C for 20 minutes have been found to be highest and also the series resistance of these devices is the lowest.

The series resistance of the devices is calculated by plotting the differential resistance as a function of voltage. The series resistance is calculated using the formula,

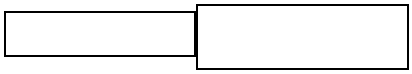

In the high voltage limit, the value of the differential resistance is the series resistance. Figure 5.12 (A) shows the plot of series resistance as a function of time of interdiffusion at different temperatures used for interdiffusion. As is evident from Figure 5.12 (A), there is a drop in the series resistance of the devices interdiffused for 20 minutes, which can explain better performance of the devices interdiffused for 20 minutes at a given temperature. Figure 5.12 (B) shows the plot of AM1.5 efficiency as function of time of interdiffusion for different temperatures. The efficiency is higher for devices interdiffused for 20 minutes at any temperature and there is drop in series resistance for the devices interdiffused for 20 minutes. The highest efficiency (2.7%) is obtained for the devices interdiffused at 150 °C for 20 minutes.

The behavior of the series resistance is not yet fully understood. One might expect that the series resistance would be smallest for the bilayer (which is indeed observed in Table 5.6) and would then increase as the interdiffusion increases as less of the material that carries the majority carriers is present at each electrode. The clear decrease in the series resistance for

devices interdiffused at 20 minutes compared to those at 10 minutes is somewhat surprising. One possibility is that, in addition to interdiffusion, the crystalline fractions of P3HT and PCBM are also being further increased during that elevated temperature cycle [10,11,12]. This would increase the electron and hole mobilities in PCBM and/or PCBM respectively, and therefore lower the series resistance. However, with further increase in the time and temperature of interdiffusion, PCBM clusters become voluminous and can destroy the metal-absorber interface [11]. This can be the reason for the increased series resistance and drop in the performance of the device for interdiffusion done beyond 20 minutes and at temperatures beyond 150 °C. In any case, the clear correlation between the series resistance and power conversion efficiencies intriguing and warrants further study.

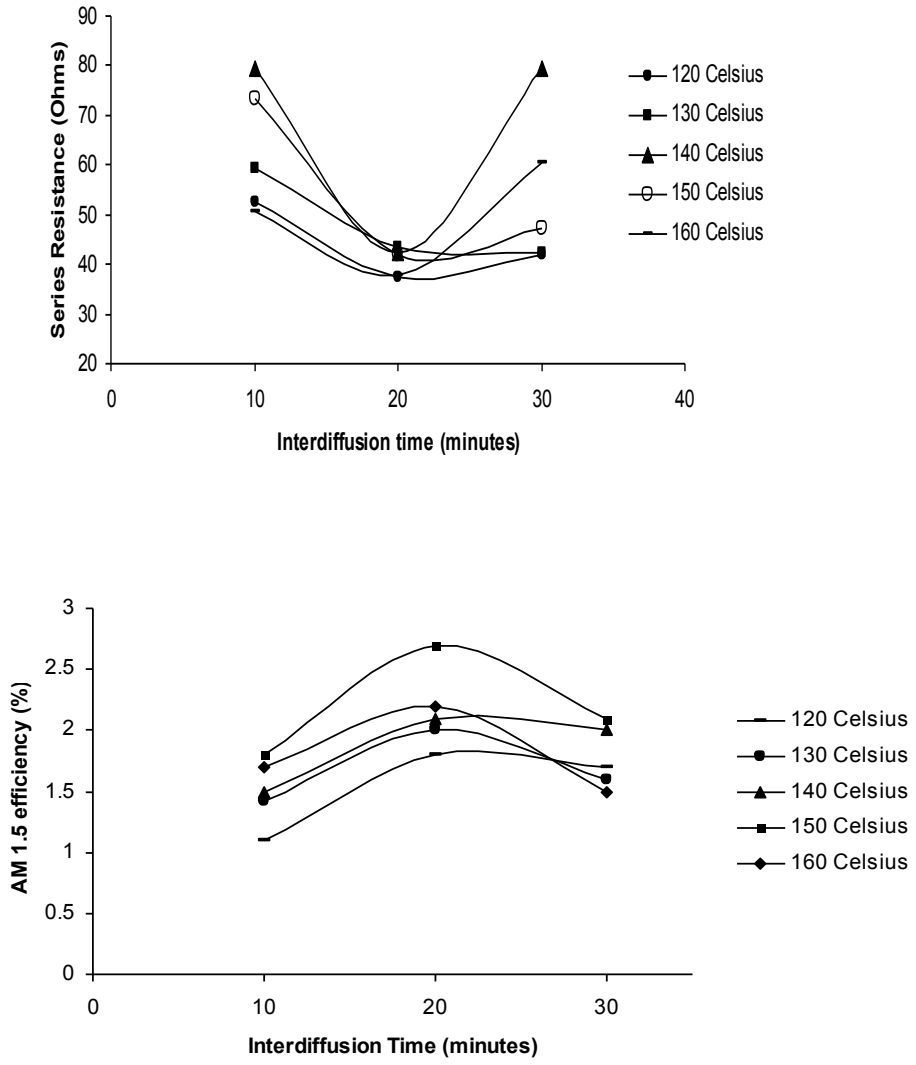

Figure 5.12 (A) Plot of series resistances as a function of time of interdiffusion at different temperatures, **5.12** (B) shows the plot of AM1.5 efficiency as a function of time of interdiffusion.

It is evident from Figure 5.12(B), the devices which are interdiffused at 150 °C for 20 minutes have the highest device performance which indicates that interdiffusion increases the interfacial area for charge transfer. The devices which are interdiffused beyond 20 minutes, there is a degradation in the device performance. In order to correlate the performance of the devices with the nanoscale control of the morphology, concentration gradient of the sulfur signal is studied as a function of the depth

In order to achieve the highest performance of the device, the concentration gradient should extend all the way across the film, ending right before the electrodes, so that device have maximum interfacial are for the charge transfer and also have one kind of material at the electrodes. Bilayer devices show a step in the sulfur signal. However, for devices which are ideally interdiffused have concentration gradient extending all the way through the device just ending right before the electrodes. The devices which are highly interdiffused have the sulfur signal moving to the surface, resulting in the decrease in the device performance.

5.3 Studying the Concentration Gradient Profiles

Concentration depth profiles of P3HT/PCBM devices were studied using the Auger spectroscopy system and x-ray photoelectron spectroscopy (XPS) system which are both combined with ion beam milling. Ion beam milling is used to sputter the surface so that depth profiling can be done. As P3HT contains sulfur and PCBM does not, the detected sulfur signal provides information on the relative amount of P3HT present as a function of depth. As the absolute intensity of the sulfur signals vary from measurement to measurement depending on the settings and sensitivity of the apparatus, the intensity of the signals is meaningful only within each scan and the magnitudes of different scans are arbitrary.

Figure 5.13 shows the Auger spectroscopy depth profiles for interdiffused devices which are interdiffused under different conditions. The results of the Auger spectroscopy correlate fairly well with the performance of the devices. Concentration gradient profiles for the devices which are interdiffused at 150 °C for 10 and 20 minutes show an increasing gradient of sulfur (indicative of the presence of P3OT) as the device is scanned from the sulfur-free PCBM layer at the top to the sulfur-containing P3HT layer at the bottom. As is evident from Figure 5.13, that with the increase in time and temperature of interdiffusion, concentration gradient eventually reverses which indicates that a high amount of polymer has moved to the surface which can lead to the degradation of the device performance. This is quite in agreement with the performance of the devices. Devices which are interdiffused at 160 °C for 20 and 30 minutes show an increased sulfur signal at the surface of the sample which can explain the degradation of the device performance.

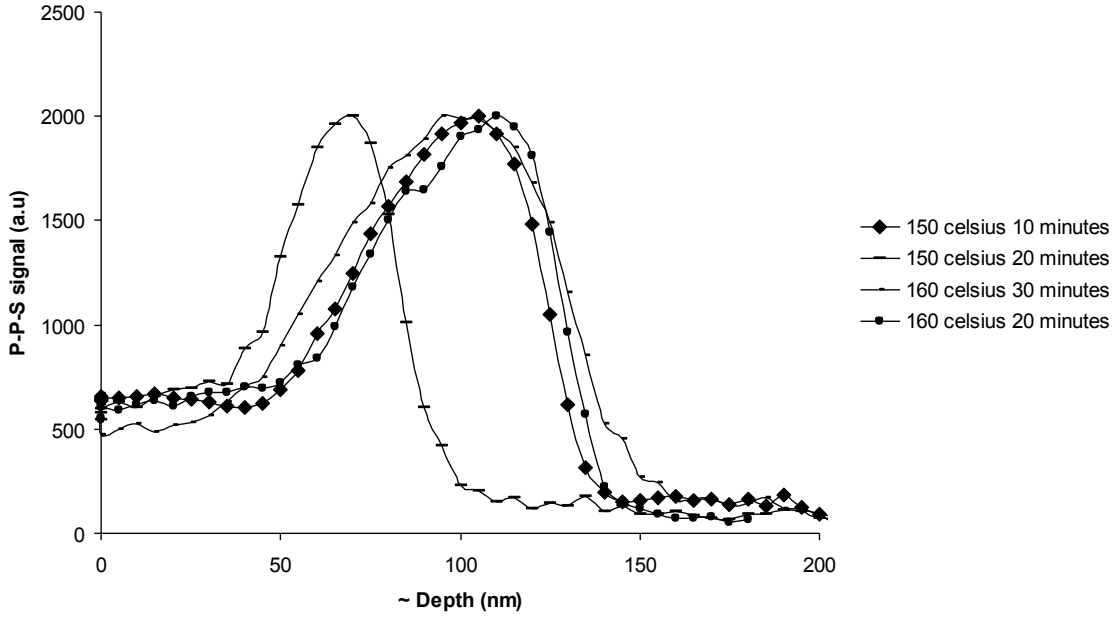

Figure 5.13 Auger spectroscopy plot of sulfur signals as a function of the depth for the device interdiffused under different conditions.

X-ray photoelectron spectroscopy (XPS) along with sputtering is another method used to investigate the depth profiles in the interdiffused P3HT/PCBM devices. This method was primarily used to confirm the results of Auger spectroscopy, and in addition bilayer devices were studied using XPS. XPS is a better technique to study polymer surfaces as x ray beam does less damage to the surface compared to the e-beam as well as it has better signal to noise ratio. Figure 5.14 shows the depth profile of relative sulfur signal obtained for P3HT/PCBM bilayer and interdiffused devices by using XPS. As is evident from Table 5.6 and Table 5.7, the interdiffused devices have better performance than bilayer devices which is due to the increased interfacial area for the charge transfer. Furthermore, the devices that are interdiffused beyond 20 minutes at 150 °C lead to the degradation of the performance. As is evident from Figure 5.14, the degradation of device performance for interdiffusion done beyond 20 minutes can be attributed to the increased sulfur signal at the surface. The devices which are interdiffused at 110 °C and 150 °C for 10 minutes show an increasing sulfur signal through the depth of the device. The first bump in the sulfur signal shows the profile of P3HT and second bump shows the presence of PEDOT:PSS. The devices which are interdiffused at 150 °C for 30 minutes show an increased sulfur signal at the surface.

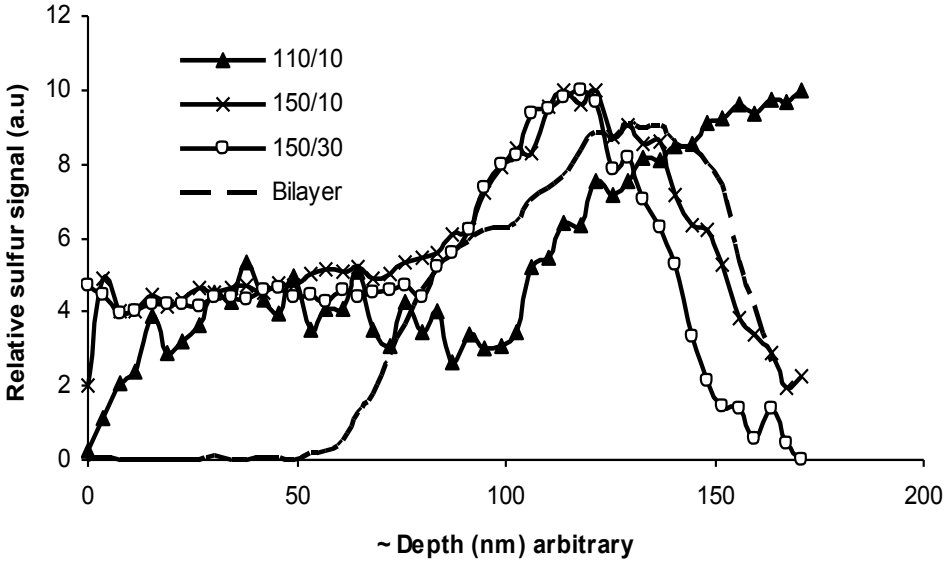

Figure 5.14 X-ray spectroscopy plot of sulfur signals as a function of the depth for the bilayer and interdiffused devices

As is evident from Figure 5.14, the bilayer devices show a fairly sharp interface indicating the presence of pure PCBM layer followed by the P3HT layer and is very close in behavior to the expected signal (Figure 4.14). The devices which are interdiffused show the concentration gradient of sulfur signal. Also, the devices which are interdiffused for a longer period of time show a pronounced amount of sulfur at the surface of the sample. The depth profile results by XPS and Auger spectroscopy correlate fairly with the device performance. Table 5.6 and Table 5.7 show that interdiffused device have better performance to the bilayer devices. Also, the devices those are interdiffused beyond 20 minutes at 150 °C lead to the degradation in the device performance due to an increase in P3HT concentration at the cathode.

5.4 Summary of P3HT PCBM Devices

Blend / bulk heterojunction device performance is best when the devices are pre-annealed at 110 °C for 5 minutes and the active device thickness is maintained at 90 nm. Table 5.3 lists the efficiency values for the bulk heterojunction devices which are annealed under different conditions. As is evident from Table 5.3, there is a drop in devices efficiency from 3.3% to 1.1% under AM1.5G illumination as the temperature of annealing is increased from 110 °C to 150 °C. Also, with the increase in the time of annealing at a particular temperature, there is a decrease in the efficiency of the devices.

Interdiffused devices with the same active layer thickness were also studied. The interdiffused devices have better performance as the temperature of the interdiffusion is increased from 120 °C to 150 °C as it will lead to the more active area where charge separation can take place. However, heating the bilayer, beyond 150 °C and for a time period beyond 20 minutes, leads to the degradation in the device performance which can be attributed to the accumulation of P3HT at the surface.

In order to compare the blends and bilayer interdiffused devices, devices with the same thickness and under similar heat treatments were compared. For the heat treatments which were done at 120 °C, the device performance of the blends is better than the interdiffused devices. However, as the temperature of heat treatment is increased, the device performance of interdiffused devices becomes better than the blends heated at similar temperature. Figure 5.15 and Figure 5.16 shows the efficiency and FF plots for the blends and interdiffused devices as the temperature of pre-annealing or interdiffusion is varied under AM1.5G illumination. The active layer thickness is maintained at 90 nm.

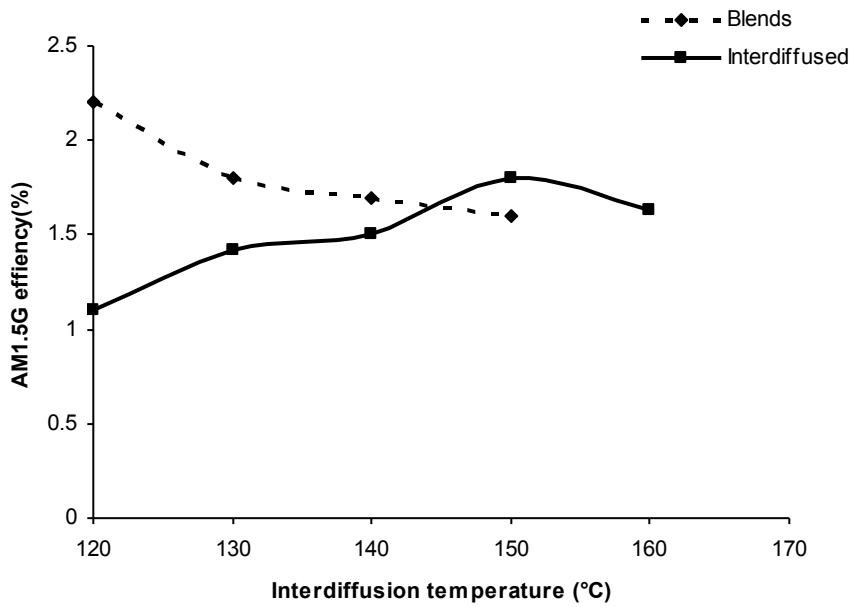

Figure 5.15 Comparison of AM1.5 efficiency of blend and interdiffused devices under varied conditions.

Figure 5.15 shows the comparison of AM1.5 efficiency under simulated solar conditions of blends and interdiffused devices. Here, the thickness of the blend device is maintained at 90 nm and of bilayer devices is at 45 nm of P3HT and 40 nm of PCBM. The efficiency and FF under AM1.5G is plotted for blends which are annealed at 120 °C, 130 °C, 140 °C and 150 °C for 10 minutes and the bilayers which are interdiffused at the respective temperatures for 10 minutes and also at 160 °C. The device performance of the blends starts degrading as the annealing temperature is increased beyond 120 °C, however for interdiffused devices the performance improves as the temperature of interdiffusion is increased from 120 °C to 150 °C. As is evident from Figure 5.15 and Figure 5.16, as the interdiffusion temperature is increased beyond 150 °C, there is a decrease in the device performance. Figure 5.16 show that the power

conversion efficiency correlates well with the fill factor suggesting that the optimization of the electrical characteristics of the devices is one of the most critical factors.

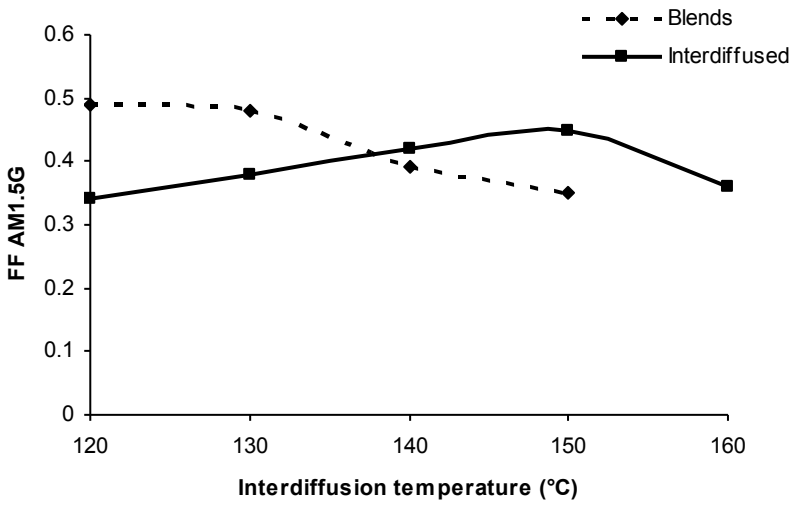

Figure 5.16 Comparison of FF AM1.5 of the blends and interdiffused devices.

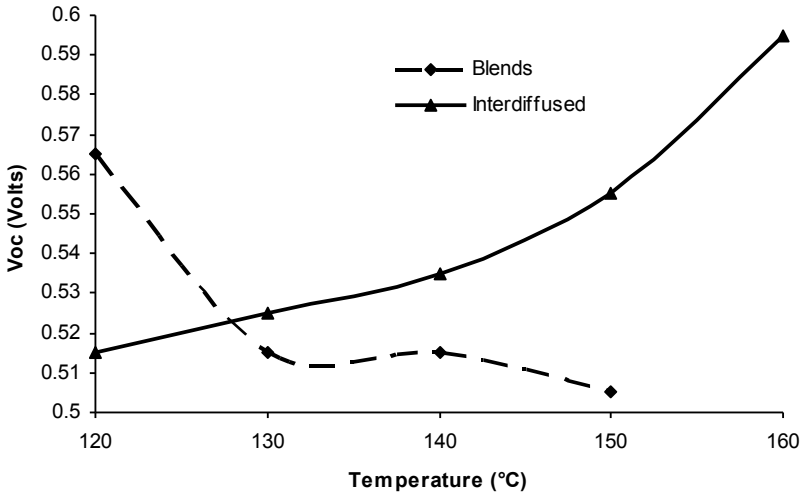

Figure 5.17 Comparison of V_{oc} under AM1.5 of the blends and interdiffused devices.

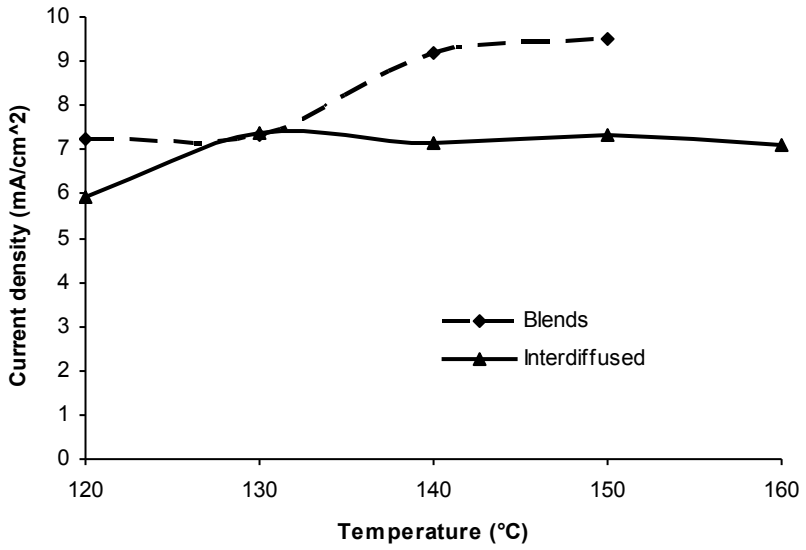

Figure 5.18 Comparison of J_{sc} under AM1.5 of the blends and interdiffused devices.

Figure 5.17 and Figure 5.18 show the plot of open circuit voltage (V_{oc}) and current density (J_{sc}) for the blends and interdiffused devices. The V_{oc} and J_{sc} under AM1.5G is plotted for blends which are annealed at 120 °C, 130 °C, 140 °C and 150 °C for 10 minutes and the bilayers which are interdiffused at the respective temperatures for 10 minutes and also at 160 °C. There is decrease in V_{oc} in blends as the temperature of annealing is increased which can be due to the increased intermixing of two components and there is increase in the J_{sc} which can be due to the increased mobility of charge carriers. There is a significant increase in the V_{oc} of interdiffused devices however there is just a slight increase in the J_{sc} with the increase in the interdiffusion temperature.

References

1. C. W. Tang, “Two-layer organic photovoltaic cell”, **Appl. Phys. Lett.**, 48(2), 183, (1986).

2. D. Vacar, E. S. Maniloff, D. W. McBranch, and A. J. Heeger, “Charge-transfer range for photoexcitations in conjugated polymer/fullerene bilayers and blends”, **Phys. Rev. B** 56, 4573, (1997).

3. J.J.M. Halls, K.Pichler, R.H.Friend, S.C.Morrati and A.B.Holmes, “Exciton diffusion and dissociation in a poly(p‐phenylenevinylene)/C60 heterojunction photovoltaic cell”, **Appl. Phys. Lett**. 68, 3120, (1996).

4. A. Haugeneder *et al*., **Phys. Rev. B**, “Exciton diffusion and dissociation in conjugated polymer/fullerene blends and heterostructures”, 59, 15346, (1999).

5. G. Dennler, M. C. Scharber, and C. J. Brabec,“Polymer-Fullerene Bulk-Heterojunction Solar Cells”, **Adv. Mater.** 21, 1323, (2009).

6. P. W. M. Blom, V. D.Mihailetchi, L. J. A. Koster, and D. E. Markov, “Device Physics of Polymer:Fullerene Bulk Heterojunction Solar Cells”,**Adv. Mater.** 19, 1551, (2007).

7. D. H. Wang, H. K. Lee, Dae-Geun Choi, J. H. Park, O. O. Park, “Solution-processable polymer solar cells from a poly(3-hexylthiophene)/[6,6]-phenyl C[sub 61]-butyric acidmethyl ester concentration graded bilayers.”, **Appl. Phys. Lett.** 95(4), 043505, (2009).

8. M. Kaur, A. Gopal , R.M. Davis , J.R. Heflin, “Concentration Gradient P3OT/PCBM Photovoltaic Devices Fabricated by Thermal Interdiffusion of Separately Spin-Cast Organic Layers”, **Solar energy materials and solar cells,** 93,1779-1784, (2009).

9. M. Hiramoto, H. Fujiwara, and M.Yokoyama, “Three‐layered organic solar cell with a photoactive interlayer of codeposited pigments”, **Appl. Phys. Lett.**, 58(10), 1062, (1991).

10. Y. Kim *et al.*, “Device annealing effect in organic solar cells with blends of regioregular poly.3-hexylthiophene. and soluble fullerene”, **Applied Physics Letters**, 86, 063502, (2005).

11. D. Chirvase, J. Parisi, J. C. Hummelen and V Dyakonov, “Influence of nanomorphology on the photovoltaic action of polymer–fullerene composites, **Nanotechnology**, 15, 1317-1323 (2004).

12. Y. Zhao *et al.*, “A calorimetric study of the phase transitions in poly(3-hexylthiophene), **Polymer**,36,11,2211-2214,(1995).

Chapter 6

Porphyrins PCBM

In this chapter, devices based on bulk heterojunction devices of porphyrins and PCBM are discussed in detail. The devices are based on blend films of a porphyrin derivative 5,10,15,20-tetraphenyl-21H,23H-porphine zinc (ZnTPP) and the fullerene derivative [6,6]-phenyl-C_{61} butyric acid methyl ester (PCBM) as the active layer. In these devices, the weight ratio of ZnTPP and PCBM is varied from 5:5 to 0:10. The devices with ZnTPP: PCBM in 1:9 ratios have the best performance. Porphyrins are chosen for this study as they have been found to exhibit interesting optical and electrical properties and hence has been studied in photovoltaic cells, OLED and OFET's [1]. Porphyrins are macrocyclic aromatic compounds with a p-type nature, which are similar to chlorophyll [2]. Porphyrins are known for their capability of strong light absorption as they are involved in the light absorption and also act as catalyst in natural photosynthesis [3]. Hence they can potentially be used in photovoltaic applications. However, porphyrins are not easily soluble in the ordinary solvents and hence can be difficult to process into the devices. However, in this study, a derivative of porphyrins which is soluble, is used as the active materials. The devices based on blends of a porphyrin derivative 5,10,15,20-tetraphenyl-21H,23H-porphine zinc (ZnTPP) and a fullerene derivative [6,6]-phenyl-C_{61} butyric acid methyl ester (PCBM, Nano C) as the active layer.

ZnTPP is used as a p-type semiconductor [4], and PCBM with excellent electron affinity is used as an n-type one. The porphyrin has a strong optical absorption in the visible spectrum [5] and was expected to form co-crystallites with PCBM [6,7]. The molecular structures of ZnTPP and PCBM are shown in Figure 6.1.

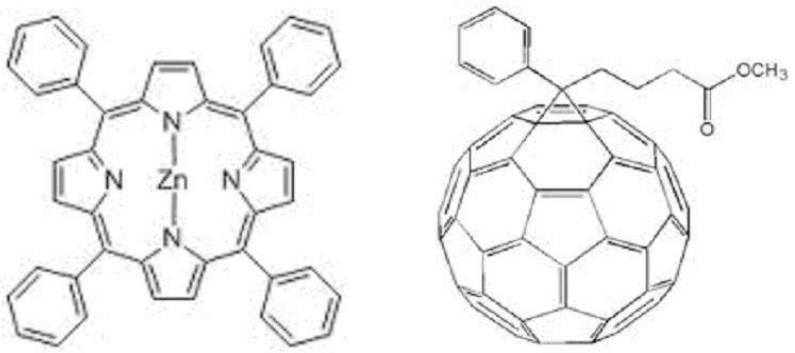

(a) (b)

Figure 6.1 Molecular structures of (a) ZnTPP and (b) PCBM.

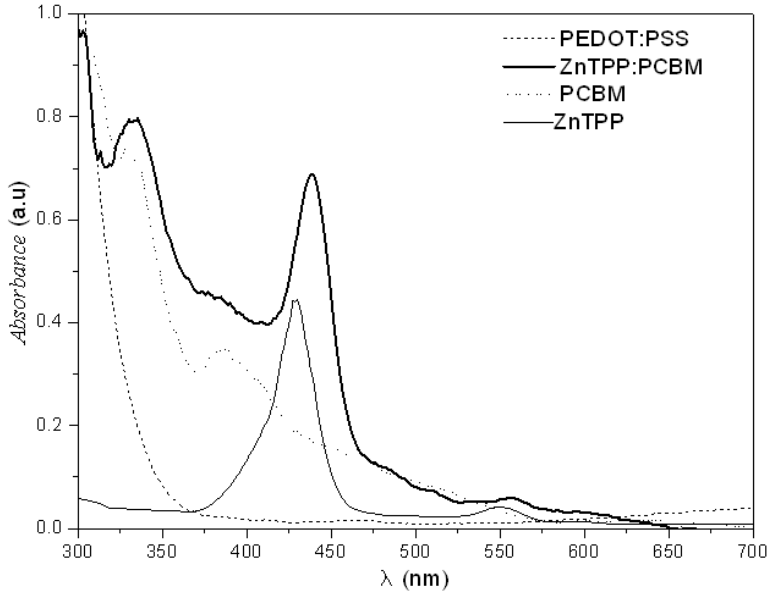

Figure 6.2 Absorption spectrum of ZnTPP: PCBM, ZnTPP, PCBM and PEDOT: PSS.

The absorption spectrum of ZnTPP shows an intense B band (Soret band) at 428 nm and Q band at 550 nm (which are shown in Figure 6.2) both arising from the corresponding π-π* transitions [8,9]. The absorption spectrum of PCBM is similar to that of C_{60}, with the absorption maximum at 327 nm and a smaller peak located at 385 nm [10]. The absorption peaks of the ZnTPP: PCBM blend have been observed at 440 nm and 333 nm and are attributed to ZnTPP and PCBM, respectively. The red shifts in the absorption peaks of ZnTPP and PCBM indicate that ZnTPP forms a new complex with PCBM [11]. The red shifts in the absorption spectrum of the blend compared to the pristine layer are evident in Figure 6.2. The electron mobility in PCBM is found to be in the range of ~10^{-3} cm^2/Vs [12,13] and the hole mobility of ZnTPP is of the order 10^{-10} cm^2/Vs [14].

The central part of the ZnTPP ring is occupied by a Zn ion linked to a pyrrole ring. The Zn ion accepts the lone-pair-electrons of the N atoms of the pyrrole ring, while the electrons of the Zn ion are donated to the porphyrin molecule, forming delocalized π bonds that permit the easy flow of electrons within the delocalized π system. The increased density in the electronic levels for π-π* transitions makes ZnTPP a relatively good electron donor [15, 16]. Generally, porphyrin/fullerene films delocalize the excited electrons from the excited molecule more efficiently as compared to pure porphyrin films on a timescale that competes effectively against the recombination or other loss processes, suggesting its application for efficient solar energy conversion [17].

6.1 ZnTPP: PCBM Bulk Heterojunction

In this set of experiments, the weight ratio of ZnTPP to PCBM was varied to study its effect on the device performance. ZnTPP and PCBM were co-dissolved in varied ratios in ODCB to make 2.0 wt/vol% solutions. 1" by 1" ITO glass substrates were spin coated with poly (3,4-ethylenedioxythiophene):poly(styrenesulfonate) (PEDOT:PSS) complex (Bayer Corporation). The spin casting of PEDOT: PSS on ITO substrate smoothens the ITO surface which is quite rough [18] as is evident from SEM image of the ITO substrate in Figure 2[b]. The PEDOT: PSS coated ITO substrates were annealed at 100 ºC for 10 minutes under atmospheric conditions. ZnTPP: PCBM solution with varied weight ratio was next spin cast onto the PEDOT: PSS coated substrates at 1200 rpm. The weight ratios studied were 5:5, 3:7, 1:9 and 0:10. The choice of the proper casting solvent for the blend solution is very important in this study, in order to obtain a smoother film of the active layer. Chlorobenzene (CB) and dichlorobenzene (o-DCB) are the best solvents for PCBM [6, 19] reported up to now. PCBM films spin-cast in these solvents show better mechanical stiffness and adhesion properties. However as ZnTPP has better solubility in o-DCB than CB [6], o-DCB has been used as the solvent for spin casting ZnTPP: PCBM film.

The thickness of each layer was determined by measuring the optical transmission and reflection using the Filmetrics F20-UV thin film spectrometer system. Finally, the electrode deposition was carried out by thermal evaporation of Al under a vacuum better than 10^{-6} Torr. The rate of the deposition was maintained at 15-20 Å/s and thickness of the order of 70 nm was deposited for each device studied. In some of the devices, thermal annealing of the devices was done prior to electrode deposition to see if it can enhance the device performance. The schematic diagram of the device construction and SEM image of cross section of a ZnTPP: PCBM 1:9 BHJ

solar cell is shown in Figure 6.3. The results for all the devices studied are summarized in Table 6.1.

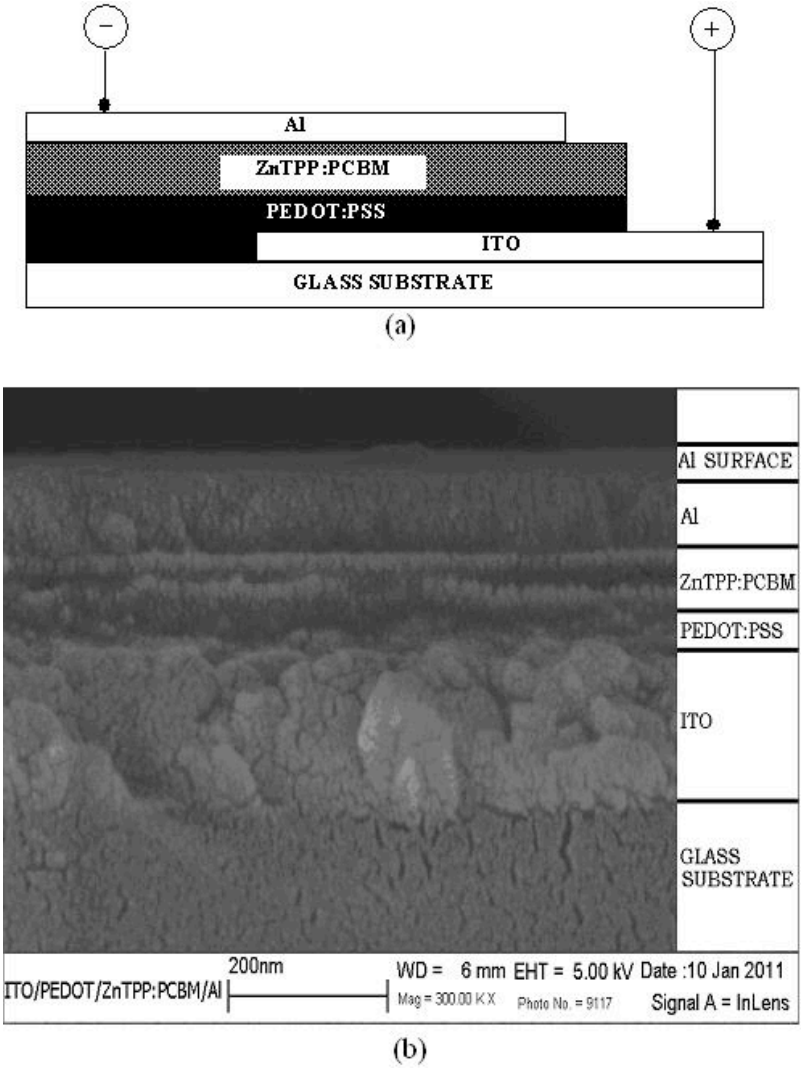

Figure 6.3 (a) Schematic diagram and (b) SEM image of cross section of fabricated ZnTPP: PCBM 1:9 BHJ solar cell.

The work functions of ITO, PEDOT: PSS and Al electrodes are -4.7, −5.2 and −4.3 eV respectively. The work function corresponds to the energy between the vacuum level and Fermi level. The energy level diagram of the ZnTPP: PCBM BHJ solar cell is shown in Figure 6.4 relative to the vacuum level. The highest occupied molecular orbital (HOMO) and lowest unoccupied molecular orbital (LUMO) levels of ZnTPP are −5.1 and −2.4 eV, respectively [20]. The HOMO and LUMO energy levels of PCBM are -6.1 and −3.7 eV, respectively [21]. After absorbing a photon, ZnTPP produces an exciton, which diffuses to the nearest D-A interface and dissociates into an electron and hole. ZnTPP transfers electrons and holes to PCBM and PEDOT: PSS respectively. PCBM transports electrons to the Al cathode while PEDOT:PSS, which acts as a hole transport and electron blocking layer, transports holes to the ITO. As PCBM can also absorb light, and generate charge carriers (not shown in energy level diagram), the two materials can work synergistically to improve the cell efficiency.

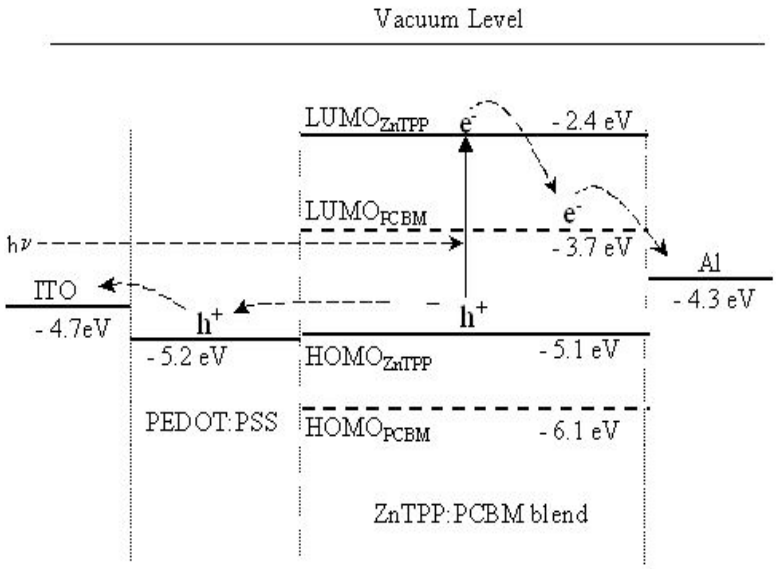

Figure 6.4 Energy level diagram of ITO/PEDOT: PSS/ZnTPP: PCBM/Al BHJ solar cell.

Photocurrent spectra of the devices were measured using a 300 W Xe lamp in combination with a CVI CM 100 monochromator as the illumination source and a Keithley 485 pico-ammeter to record the short circuit current, I_{sc}. Current-Voltage (I–V) curves were measured with a Keithley 236 source measure unit in the dark as well as under AM1.5G simulated solar spectrum. The optical density (OD), of the ZnTPP: PCBM blended layer was determined from the reflection (R) and transmission (T) data obtained with the F20 UV spectrometer. The resulting OD was used to determine film thickness of the active layer using Beer-Lambert's Law. The absorption coefficient values used for the thickness calculation are 1.1×10^4 cm^{-1} at 510 nm for ZnTPP [22] and 2×10^4 cm^{-1} at 512 nm for PCBM [23] based on their weight ratio. Figure 6.2 shows the absorption spectra of the ZnTPP: PCBM 1:9 weight ratio blend layer relative to the spectra of ZnTPP, PCBM and PEDOT: PSS. The active layer spectrum shows the red shifts in the absorption peaks compared to the pristine layer indicating the formation of a new complex when blend is made.

6.1.2 Effect of Variation of the Weight Ratio on the ZnTPP: PCBM Blend Device Performance

Figure 6.5 shows the photocurrent spectra recorded for the devices with different weight ratio. The maximum of the photocurrent occurred at 440 nm for all the devices as is evident from Figure 6.5, except for the 0:10 weight ratio device which has maxima at 400 nm as it is a purely PCBM device. The photocurrent spectrum is in quite good correlation with the OD spectra of the devices. Figure 6.6 shows the OD spectra of these devices with varied weight ratios.

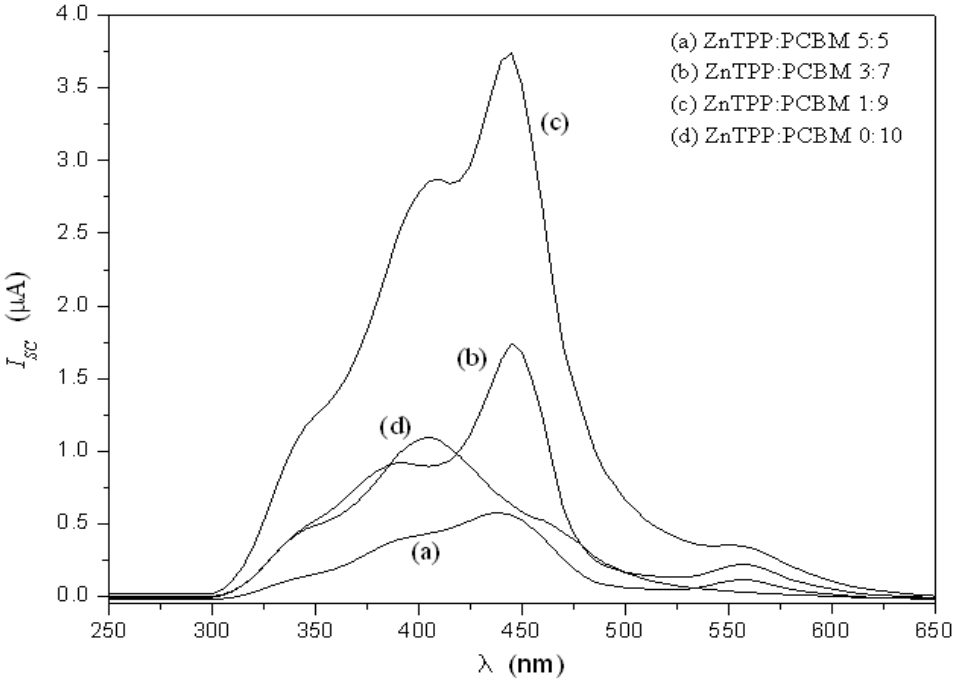

Figure 6.5 Comparative photocurrent spectra of ZnTPP: PCBM BHJ solar cells.

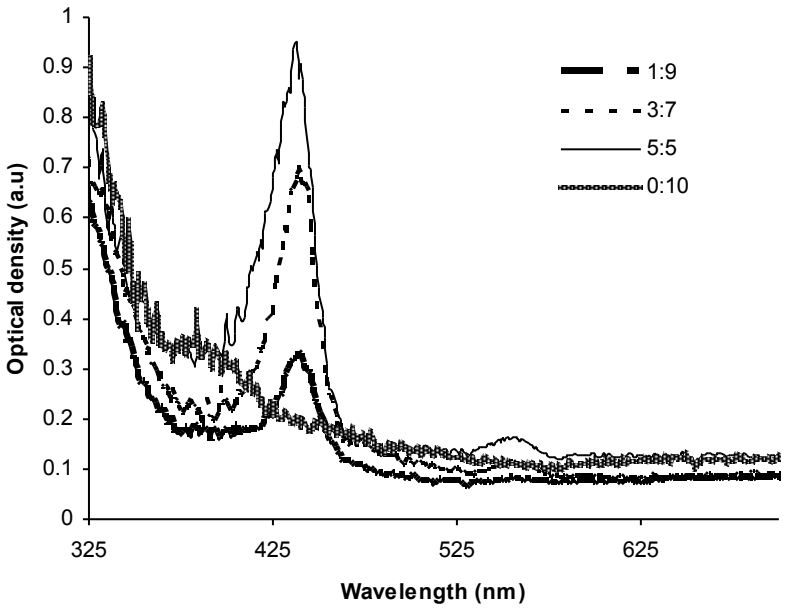

Figure 6.6 Comparative optical density spectra of ZnTPP: PCBM BHJ solar cells.

Figure 6.6 shows the optical density spectra of the ZnTPP:PCBM devices with varied weight ratio. There is an increase in the absorption signal at 440 nm as ZnTPP to PCBM ratio is increased from 1:9 to 5:5. The enhancement of photocurrent at 440 nm for 1:9 ZnTPP: PCBM device could be because of the lower rate of recombination at that weight ratio. It has been found that there are intermediate energy levels or gap states that are present in between the conduction and valence band of ZnTPP and they act as the centers for recombination on illumination [24, 25]. A more recent study has revealed that, first, the gap states in the porphyrin semiconductor are responsible for the NIR light absorption and second, that the electronic transitions to or from the gap states diminishes the rate of recombination of electron-hole pairs via these intermediate states, leading to the enhancement of the 440 nm photocurrent [26].

Figure 6.7 shows the EQE spectra of the ZnTPP: PCBM bulk heterojunction devices as the weight ratio is varied. The devices with 1:9 weight ratios have higher EQE than the devices with other ratios. The spectrum profile of the 3:7 ratio looks similar to the 1:9 weight ratio however, the devices with 1:9 ratios have enhanced performance. These devices were made with 2% wt/vol solution in ODCB.

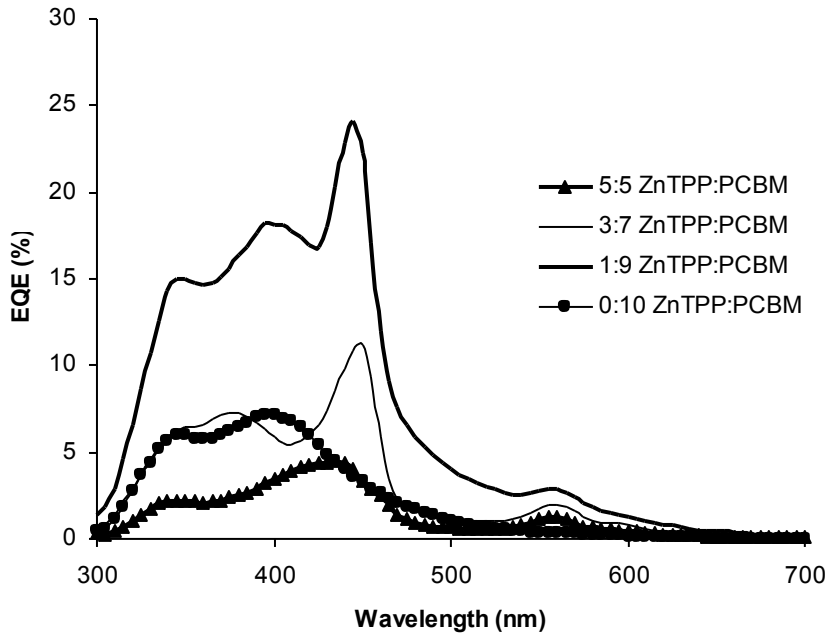

Figure 6.7 EQE spectra of ZnTPP: PCBM bulk devices with the varied weight ratios.

Figure 6.8 shows the I-V spectra of the ZnTPP:PCBM 1:9 device under dark, monochromatic and AM1.5G illuminations. The active area of each device is 0.12 cm^2. The rectification behavior of the device is quite evident from the I-V characteristics. The rectification ratio of the different devices is shown in Table 6.1. Table 6.1 summarizes the various parameters such as efficiency, FF, I_{sc} and V_{oc} respectively, calculated for the different devices with varied weight ratios. Table 6.1 also lists the various parameters for the devices made with 2% wt/vol and with varying weight ratios along with annealing conditions (if done) as well as the devices made with 3.0% wt/vol.

Devices made with 2.0% wt/vol show an increasing trend in the RR, V_{oc}, I_{sc}, FF and η as the weight ratio of ZnTPP (D): PCBM (A) is increased from 5:5 to 1:9 with a drop in performance as 0:10 ratio is reached. The best efficiency is obtained for devices with weight ratio

of 1:9, the highest being 0.21% under AM1.5 illumination, which is better than the devices reported previously with ZnTPP as the donor [6].

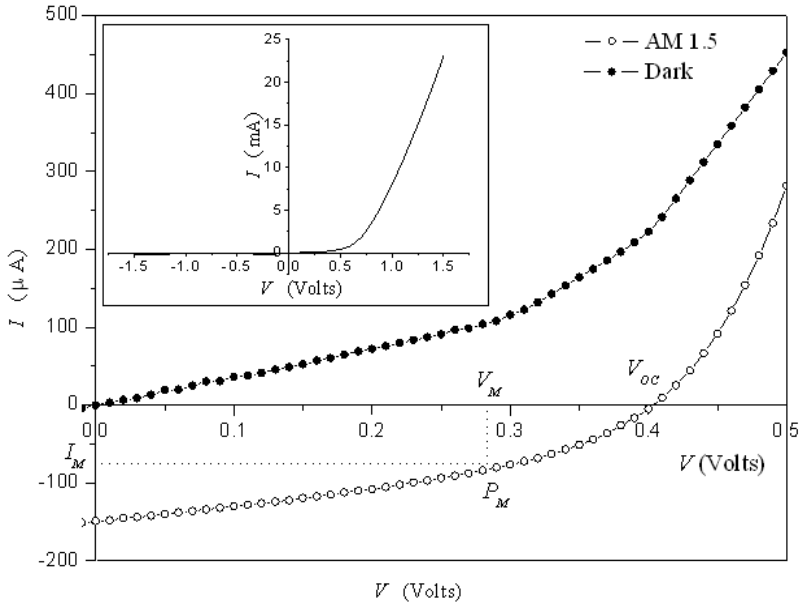

Figure 6.8 I-V characteristics of ZnTPP: PCBM 1:9 BHJ solar cells in dark (solid circles) and under an illumination of AM1.5 G (empty circles).The inset show dark *I-V* Characteristics.

These earlier reported devices with ZnTPP as the donor [6] were made with C_{60} as an acceptor molecule. The devices fabricated with PCBM as acceptor molecules are expected to have better performance than C_{60} due to the higher LUMO level of PCBM compared to C_{60} which can give better V_{oc} and FF of the devices.

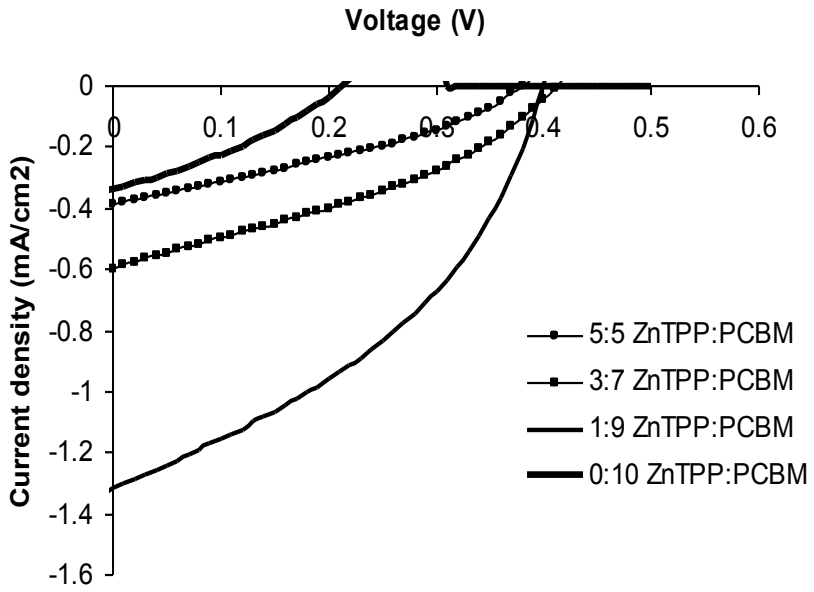

Figure 6.9 AM1.5G illumination 4th quadrant J-V characteristics for ZnTPP: PCBM devices with varied weight ratios in the blend.

Figure 6.9 shows the 4th quadrant J-V characteristics of ZnTPP: PCBM bulk devices. The devices with 1:9 ratios have the highest V_{OC} and FF of all devices. Figure 6.10 and Figure 6.11 shows the trend of series and shunt resistance as the weight ratio of ZnTPP to PCBM is varied. As the weight ratio is varied from 5:5 of ZnTPP: PCBM to 0:10 of ZnTPP:PCBM, there is a dip in the series resistance at 1:9 and a large increase in shunt resistance under the same conditions.

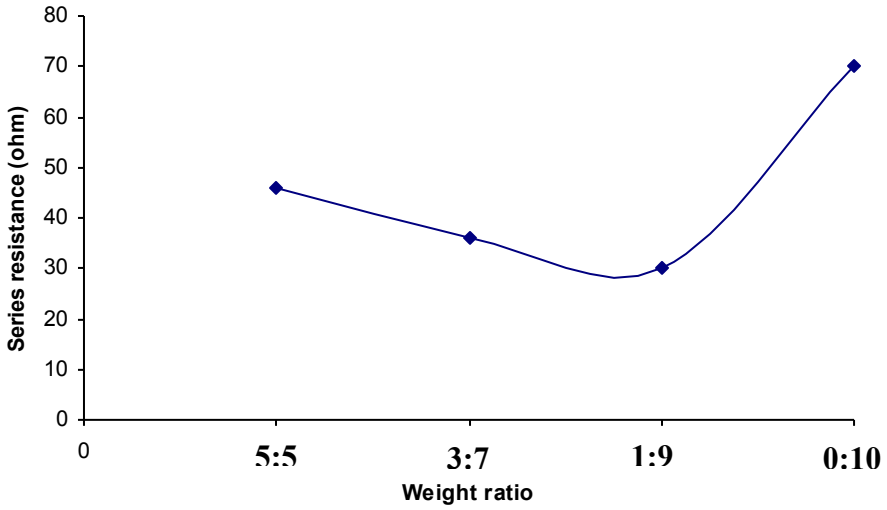

Figure 6.10 Trend of series resistance for ZnTPP: PCBM devices with varied weight ratios in the blend.

Figure 6.10 shows the trend of series resistance as the weight ratio is varied. The devices with 1:9 weight ratios have the highest performance. The series drops significantly for the 1:9 ratios ZnTPP:PCBM devices. Figure 6.11 shows the trend of shunt resistance, as the weight ratio is varied from 5:5 to 0:10, the devices with 1:9 ratio have the highest shunt resistance. In general, the devices should have lowest series resistance and the highest shunt resistance for the efficient device performance.

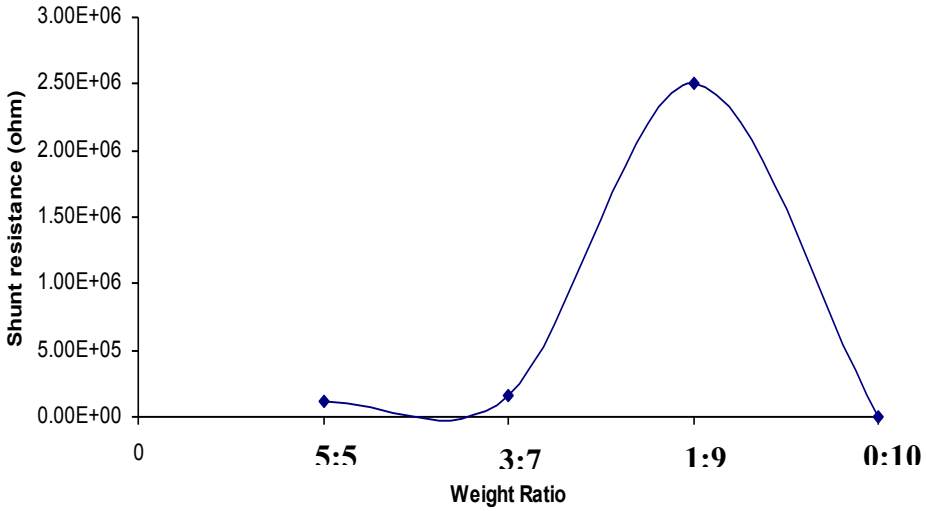

Figure 6.11 Trend of shunt resistance for ZnTPP: PCBM devices with varied weight ratios in the blend.

Table 6.1 Measured parameters of ITO/PEDOT: PSS/ZnTPP: PCBM /Al bulk heterojunction solar cells under AM1.5 conditions.

ZnTPP:PCBM Ratio	Concentration (% Wt. / Vol.)	Thickness (nm)	Annealing Conditions	*RR* (at ±1V)	*V*oc (V)	*I*sc (uA)	*FF*	η (%)
5:5	2.0	75		42.6	0.37	46	0.34	0.049
5:5	2.0	75	130 °C/10 min	13.9	0.42	25	0.3	0.026
3:7	2.0	69		78.1	0.4	67.4	0.35	0.09
3:7	2.0	69	100 °C/10 min	38.9	0.34	48.2	0.25	0.034
3:7	3.0	119		36.2	0.48	20	0.19	0.015
1:9	2.0	68		106	0.4	149	0.4	0.19
1:9	2.0	68		106	0.4	158	0.4	0.21
0 :10	2.0	70		4.6	0.21	40	0.32	0.023

As the devices fabricated with 3.0% wt/vol had lower power performance compared to the similar devices fabricated with 2.0% wt/vol. Hence most of the devices were made with 2.0% wt/vol solution. The annealing of the devices was also performed on a couple of samples, in order to try to minimize the defects in the films. However, as is evident from Table 6.1, annealing leads to degradation in the performance of the devices. The degradation of the device performance on annealing can be attributed to the enhancement of the aggregation of porphyrins [7]. The excitons formed in these larger aggregates have lower probability of reaching the interface before recombination. Hence, annealing of the subsequent samples was not carried out. *The best devices performance is achieved for devices which are non-annealed and with 1:9 weight ratios of ZnTPP: PCBM.*

The best performance is attained for devices with 1:9 ZnTPP: PCBM ratio which suggests that the devices with this weight ratio have better morphology than the others. Porphyrins have been found to co-crystallize with fullerenes [6], which may results in the aggregation. As the microstructure of the bulk layer is strongly dependent on the weight ratio, this suggests that the devices with 1:9 weight ratio are the most favorable to form co-crystallites and have the most favorable microstructure. The presence of continuous co-crystallite structures perpendicular to the thin film layer is expected to suppress the recombination of electrons and holes. Hence the better performance of the devices with 1:9 weight ratios could mean that this ratio provides a continuous co-crystallize structure compared to other devices with other weight ratios (intermittent co-crystallite structures). As evident from Table 6.1, the devices with 1:9 weight ratios have the highest device efficiency as well as better performance to other devices.

The thickness calculation of the active layer was also done by using a DekTak-150 profilometer along with thickness calculation from the optical density spectra using Filmetrics UV-20 spectrometer. The thickness observed from the step profile of profilometer is in close proximity to the thickness determined by using Filmetrics. The surface roughness is another parameter that was studied using profilometer. Figure 6.12 shows the observed surface roughness of the blend sample. The surface roughness is found to be within the ± 8 nm as evident from Figure 6.12.

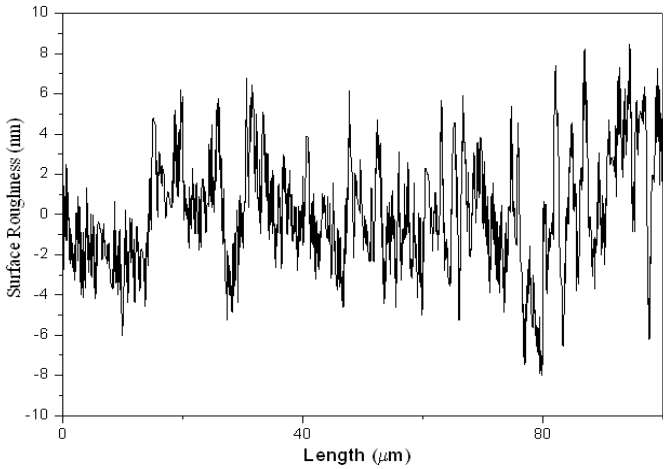

Figure 6.12 Surface profile of a ZnTPP: PCBM films spin casted in o-DCB.

6.2 Summary of ZnTPP: PCBM Bulk Heterojunction Devices

ZnTPP:PCBM BHJ solar cells were fabricated and characterized for their electronic and optical properties. ZnTPP:PCBM bulk heterojunction devices were successfully studied primarily by varying the weight ratio in the blend. The effects of the

variation of the thickness of the active layer and the annealing conditions on the device performance were also studied. It was found that devices with 1:9 weight ratios have the highest performance. Furthermore, annealing of the devices is found to degrade the device performance. The degradation of the device performance on annealing can be attributed to the enhancement of the aggregation of porphyrins [7]. The excitons formed in these larger aggregates have lower probability of reaching the interface before recombination.

The highest performance of the 1:9 weight ratio devices can be attributed to the better morphology and most favorable microstructure of the devices. Porphyrins have been known to co-crystallize with fullerenes [6], which may results in the aggregation. The presence of continuous co-crystallite structures perpendicular to the thin film layer is expected to suppress the recombination of electrons and holes. Hence the better performance of the devices with 1:9 weight ratios could mean that this ratio provides a continuous co-crystallize structure compared to other devices with other weight ratios (intermittent co-crystallite structures).

PCBM has high electron mobility (~10^{-3} cm^2/Vs) [13], as compared to the hole mobility of ZnTPP which is of the order 10^{-10} cm^2/Vs [14]. A further enhancement in efficiency could be achieved with a porphyrin derivative having mobility on a par with PCBM. Thus, new donor and acceptor materials, having higher mobilities and that are soluble in common solvents for solution processing can be used to fabricate the BHJ solar cells at their optimum ratios. In the future, this can be used to boost the performance of porphyrin and phthalocyanine BHJ solar cells fabricated by wet processing.

References

1. H. Mao, Y. Sun, H. Li, Q. Zhou, X. Zhang, J. Shen, H. Xu, Sci. China, **Ser. B: Chem.**, 41, 449-454, (1998).

2. Y. Harima, K. Takeda, K. Yamashita, "Molecular solid of zinc tetraphenylporphyrin as a model organic semiconductor with a well-defined depletion layer", **J. Phys. Chem. Solids**, 56, 1223- 1229, 1995.

3. C.W. Tang, A.C. Albrecht,"Chlorophyll-a photovoltaic cells", **Nature**, 254, 507-509, (1975).

4. K. Takahashi, N. Kuraya, T. Yamaguchi, T. Komura, K. Murata, "Three-layer organic solar cell with high-power conversion efficiency of 3.5%", **Sol. Energy Mater. Sol. Cells**, 61, 403-416, (2000).

5. Q. Sun, L. Dai, X. Zhou, L. Li, Q. Li, **Appl. Phys. Lett**., 91, 253505-253501-253503, (2007).

6. T. Oku, T. Noma, A. Suzuki, K. Kikuchi, S. Kikuchi, "Fabrication and characterization of fullerene/porphyrin bulk heterojunction solar cells", **J. Phys. Chem. Solids**, 71, 551-555, (2010).

7. W.J. Belcher, K.I. Wagner, P.C. Dastoor," The effect of porphyrin inclusion on the spectral response of ternary P3HT:porphyrin:PCBM bulk heterojunction solar cells", **Sol. Energy Mater. Sol. Cells**, 91, 447–452, (2007).

8. D.M. Cleland, K.C. Gordon, D.L. Officer, P. Wagner, P.J. Walsh, "Tuning the optical properties of ZnTPP using carbonyl ring fusion", Spectrochim. **Acta, Part A**, 74, 931–935, (2009).

9. J. Spadavecchia, R. Rella, P. Siciliano, M.G. Manera, A. Alimelli, R. Paolesse, C.D. Natale, A. D'Amico, "Optochemical vapour detection using spin coated thin film of ZnTPP", **Sens. Actuators, B**, 115, 12-16, (2006).

10. L. Shengli, Y. Mujie, **Chemistrymag**, 5, 49, (2003).

11. G.Yin, D. Xu, Z. Xu, "Spectral behavior of cis-2′,5′ dipyridinylpyrrolidino[3′,4′:1,2][60]fullerene and its coordination complex with Zinc porphyrin (ZnTPP)" , **Chem. Phys. Lett**., 365, 232-236, (2002).

12. J.M. Kroon, S.C. Veenstra, L.H. Slooff, W.J.H. Verhees, M.M. Koetse, J. Sweelssen, H.F.M. Schoo, W.J.E. Beek, M.M. Wienk, R.A.J. Janssen, X. Yang, J. Loos, V.D.

Michailetchi, P.W.M. Blom, J. Knol, J.C. Hummelen, "Polymer based photovoltaics: novel concepts, materials and state-of-the art efficiencies", 20th European Photovoltaic Solar Energy Conference and Exhibition, Barcelona, Spain, (2005).

13. E.V. Hauff, V. Dyakonov, J. Parisi, "Study of field effect mobility in PCBM films and P3HT:PCBM blends" ,**Sol. Energy Mater. Sol. Cells**, 87, 149-156, (2005).

14. Y. Harima, S. Furusho, Y. Kunugi, K. Yamashita, "Drift mobility of holes in vacuum-deposited films of zinc tetraphenylporphyrin", **Chem. Phys. Lett.**, 258, 213-216, (1996).

15. S. Uttiya, Development of molecular sensors based on optical absorption of organic thin films., in: Faculty of graduate studies, Mahidol University, Nakhon Pathom,Thailand, (2008).

16. W. Zheng, N. Shan, L. Yu, X. Wang, **Dyes Pigm.**, 77, 153-157, (2008).

17. P. Vilmercati, C.C. Cudia, R. Larciprete, C. Cepek, G. Zampieri, L. Sangaletti, S. Pagliara, A. Verdini, A. Cossaro, L. Floreano, A. Morgante, L. Petaccia, S. Lizzit, C. Battocchio, G. Polzonetti, A. Goldoni, "Molecular orientations, electronic properties and charge transfer timescale in a Zn-porphyrin/C70 donor–acceptor complex for solar cells", **Surf. Sci.**, 600, 4018–4023, (2006).

18. M. Egginger, Zn-Phthalocyanine / C60 Solar Cells, in: Wirtschaftsingenieurwesen - Technische Chemie, Johannes Kepler Universität Linz, Linz, Austria, pp. 76, 2005.

19. S.E. Shaheen, C.J. Brabec, N.S. Sariciftci, F. Padinger, T. Fromherz, J.C. Hummelen," 2.5% efficient organic plastic solar cells", **Appl. Phys. Lett.**, 78, 841-843, (2001).

20. R. Ma, P. Guo, H. Cui, X. Zhang, M.K. Nazeeruddin, M. Gratzel, "Substituent Effect on the Meso-Substituted Porphyrins: Theoretical Screening of Sensitizer Candidates for Dye-Sensitized Solar Cells", **J. Phys. Chem. A**, 113, 10119–10124, (2009).

21. P. Kumar, S.C. Jain, V. Kumar, S. Chand, R.P. Tandon, "Effect of illumination on the space charge limited current in organic bulk heterojunction diodes", **Appl. Phys. A**, 94, 281-286, (2009).

22. J.A. Ferreira, R. Barral, J.D. Baptista, M.I.C. Ferreira, "Absorption coefficients and fluorescence quantum yields of porphyrin films determined by optical and photoacoustic spectroscopies", **J. Lumin.**, 48-49, 385-390, (1991).

23. M. Kaur, A.Gopal, R.M. Davis, J.R. Heflin, "Concentration Gradient P3OT/PCBM Photovoltaic Devices Fabricated by Thermal Interdiffusion of Separately Spin-Cast Organic Layers", **Sol. Energy Mater. Sol. Cells**, 93 ,1779-1784, (2009).
24. Y. Harima, M.Miyatake, K. Yamashita, "Synergism in photocurrent induced by simultaneous illumination of porphyrin solids with visible and near-infrared lights." **Chem. Phys. Lett.**, 200, 263-266, (1992).
25. Y. Harima, M.Miyatake, K. Yamashita, "Recombination process via gap-state responsible for photocurrent synergism observed with porphyrin solids", **Chem. Phys. Lett**., 229 , 47-50, (1994).
26. Y. Harima, T. Kodaka, P. Price, T. Eguchi, K. Yamashita, "Light absorption in the near-infrared and photocurrent synergism observed with vacuum-sublimed films of zinctetraphenylporphyrin" **Thin Solid Films**, 307, 208-214 (1997).

Chapter 7

Endohedral Fullerene Acceptors

A series of bulk heterojunction devices were made by incorporating the endohedral fullerenes as an acceptor material in the device structure. Trimetallic Nitride Template endohedral fullerenes are fullerene cages that enclose a nitrogen atom and three metal atoms. Discovered by Prof. Harry Dorn and collaborators, this class of fullerenes offers a wide range of tunability of structures with higher yields than any fullerenes other than C_{60} and C_{70} [1]. PCBM is the most widely used acceptor for most of the work done in this thesis, as well as in the broader research community. It has been shown that open circuit voltage of the bulk heterojunction solar cells can be related to the difference between the HOMO level of the donor and the LUMO level of the acceptor [2, 3, and 4]. Hence, recent attempts have been made to synthesize new acceptor materials with raised LUMO levels compared to PCBM. TNT endohedral fullerenes exhibit higher LUMO levels compared to empty cage fullerenes like PCBM due to the electron transfer from the endohedral cluster to carbon cage [5]. The main reason for interest in this material is that the LUMO level, and consequently, the band gap and V_{oc} can be tuned by varying the metal atoms that are enclosed. Figure 7.1 shows the predicted V_{oc} of the solar cells devices when different molecules are used with MDMO-PPV as the donor material. The predicted V_{oc} of these devices is of the order of 1.2-1.3 eV which is much higher than the highest V_{oc} predicted by Hummelen *et al.* [6]. Hummelen and co-workers predicted that the highest V_{oc} possible with different substituents on the phenyl ring of the PCBM is

0.85 eV. In this chapter, different new acceptor materials were studied to examine their influence on the device performance.

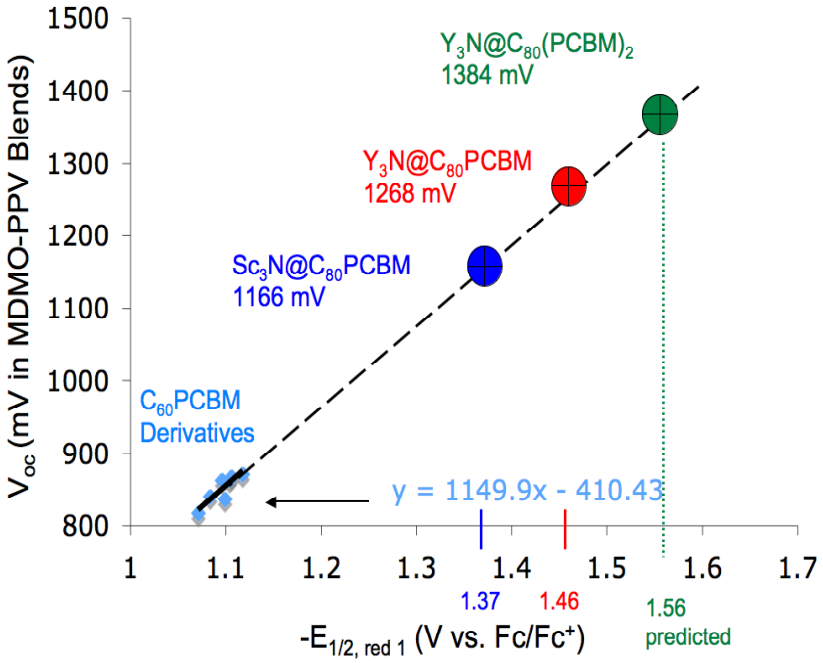

Figure 7.1 Extrapolation of the data of Hummelen *et al*. to estimate V_{oc} for various TNT endohedral fullerenes acceptor molecules in solar cells with MDMO-PPV.

Figure 7.1 shows predicted V_{oc} of the bulk heterojunctions devices of P3HT with various acceptor molecules. It is evident from Figure 7.1, $Y_3N@C_{80}$-PCBM based devices can have better V_{oc} than the $Sc_3N@C_{80}$-PCBM devices. This fact is supported by the oxidation and reduction potential data collected by cyclic voltammeter in Table 7.1. The reduction potential corresponds to LUMO level and the oxidation potential corresponds to HOMO level. It is evident from Table 7.1, that $Y_3N@C_{80}$-PCBM can have

reduced energy offset with P3HT compared to $Sc_3N@C_{80}$-PCBM, and thus hence lower energy losses in the charge transfer process and better device performance.

Table 7.1 Reduction and Oxidation potential of TNT Endohedral fullerenes.

	E_{red} (LUMO)	E_{ox} (HOMO)
$Sc_3N@C_{80}$-PCBM	-1.416	0.503
$Y_3N@C_{80}$-PCBM	-1.51	0.64

7.1 TNT Endohedral Fullerenes

$M_3N@C_{80}$ -PCBM (M= Sc; Y)

$Sc_3N@C_{80}$ -PCBM (2a) was synthesized in the groups of Profs. Harry Dorn and Harry Gibson from $Sc_3N@C_{80}$ and methyl 4-benzoylbutyrate *p*-tosylhydrazone as shown in Figure 7.1. $Sc_3N@C_{80}$ is the most abundant species in endohedral fullerenes and has been previously studied in detail in bulk heterojunction devices with P3HT as the donor material [7]. In this chapter, bulk heterojunction devices with P3HT as donor material and $M_3N@C_{80}$ -PCBM (M=Sc, Y) as an acceptor material are discussed. The goal is to combine the solution processability and compatibility with polythiophenes of the PCBM side chain with the potential for higher V_{oc} associated with the higher LUMO level of the endohedral fullerenes. Ross *et al.* have done studies on the blend devices of TNT endohedral fullerenes and P3HT and efficiency of the order of 4% was observed for these devices under AM1.5 illuminations [8]. This study has shown by using TNT endohedral

fullerenes, the energy offset of the molecular orbital of the acceptor molecule and P3HT can be reduced and hence lower energy losses in the charge transfer process.

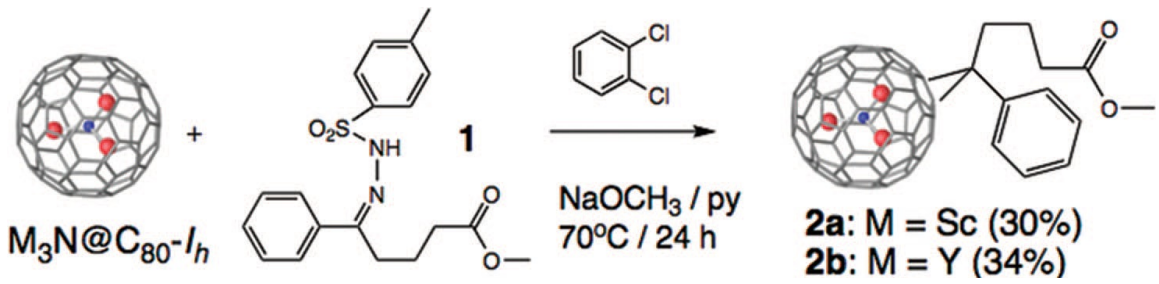

Figure 7.2 Process of synthesis of $M_3N@C_{80}$ -PCBM.

1" by 1" ITO glass substrates were spin coated with poly (3,4-ethylenedioxythiophene):poly(styrenesulfonate) (PEDOT:PSS) complex (Bayer Corporation). PEDOT: PSS coated ITO substrates were annealed at 100 ºC for 10 minutes under atmospheric conditions. P3HT:$M_3N@C_{80}$ -PCBM, M = Sc, Y , (1:1) blend solution was spin casted onto the PEDOT: PSS coated ITO substrates. In some of the devices, the active layer is annealed at various temperature profiles under the continuous supply of argon, followed by the electrode deposition.

7.2 P3HT:$Sc_3N@C_{80}$-PCBM Devices

1% wt/vol P3HT: $Sc_3N@C_{80}$-PCBM (1:1) solution was used to spin cast the active layer of the devices. The blend solution in chlorobenzene (CB) is spin casted at 1000 rpm. The active layer thickness was calculated by measuring the optical reflection and transmission using Filmetrics F20-UV thin film spectrometer system as explained in

Chapter 3. The thickness of the active layer was maintained at 25 nm. A large thickness would have been desired, but the $Sc_3N@C_{80}$ had insufficient solubility in CB. Finally, the electrode deposition was carried out by thermal evaporation of Al under a vacuum better than 10^{-6} Torr. The rate of the deposition was maintained at 15-20 Å/s and thickness of the order of 70 nm of Al is deposited for each device studied. The devices were annealed at varied conditions to optimize the device performance. Figure 7.2 shows the EQE plot of devices annealed at various conditions. The devices annealed at 110 °C for 5 minutes were found to have better performance. However, it should be noted that the EQE values are smaller than those for P3HT:PCBM by about a factor of 100.

7.3 P3HT:$Y_3N@C_{80}$-PCBM devices

P3HT: $Y_3N@C_{80}$-PCBM (1:1) 1% wt/vol solution in CB was used for the active layer. The active layer was spin cast onto the PEDOT: PSS coated ITO substrate at 1000 rpm. The active layer thickness was maintained at 25 nm. Figure 7.3 shows the comparison of EQE of the devices annealed at varied conditions. As is evident from Figure 7.3, the devices with $Y_3N@C_{80}$-PCBM as the acceptor material have been found to have better performance than the devices with $Sc_3N@C_{80}$-PCBM as the acceptor but still substantially lower than the P3HT:PCBM.

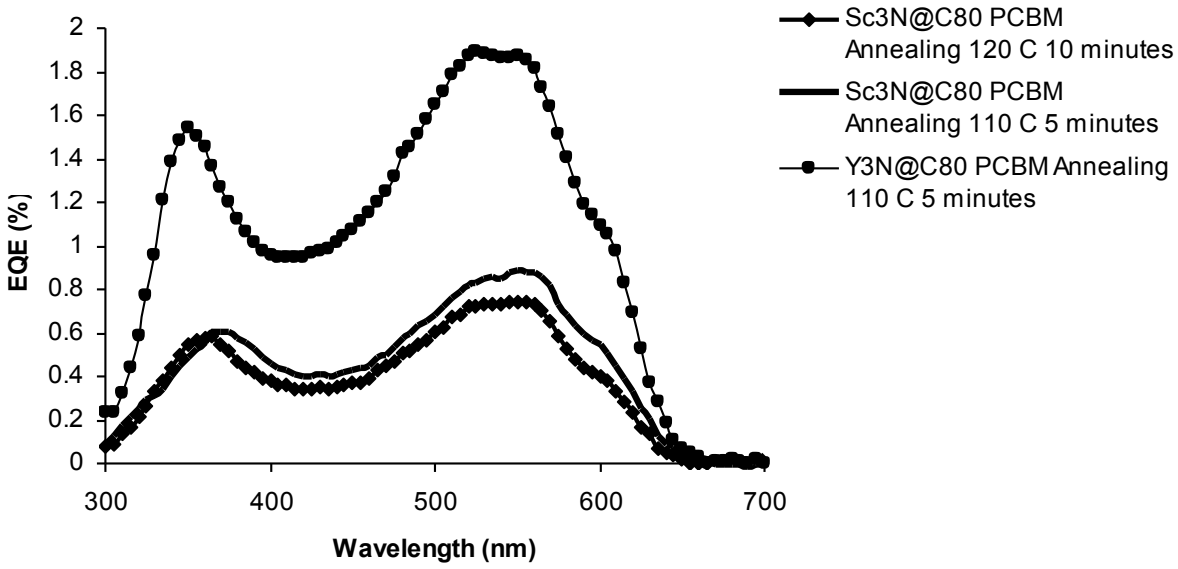

Figure 7.3 EQE plot of comparison of P3HT: $M_3N@C_{80}$-PCBM; M=Sc, Y; devices annealed at varied conditions.

The better performance of $Y_3N@C_{80}$-PCBM based devices can be due to better V_{oc} of these devices compared to $Sc_3N@C_{80}$-PCBM based devices as evident from Figure 7.1 and Table 7.1.

7.4 P3HT: $Y_3N@C_{80}$-PCBH Devices

As is evident from Figure 7.3, the devices made with $Y_3N@C_{80}$-PCBM have better performance than the devices with $Sc_3N@C_{80}$-PCBM as an acceptor. Thus, different derivatives of Y_3N based endohedral fullerenes were studied further. Earlier studies done on PCBH based derivatives have shown that they are most closely similar in solubility and miscibility to PCBM than the PCBM based derivatives. Also, it was found that $Lu_3N@C_{80}$-PCBH has similar charge carrier mobility to PCBM ($4x10^{-4}$ $cm^2V^{-1}s^{-1}$ for

$Lu_3N@C_{80}$-PCBH versus $1.4x10^{-3}$ for PCBM) [8]. Blend devices of $Lu_3N@C_{80}$-PCBH and P3HT achieved an efficiency of 4.0% under AM1.5 illumination. Hence, the rest of the work is focused on the study of bulk heterojunction devices of PCBH based derivatives and P3HT.

The bulk heterojunction devices with P3HT: $Y_3N@C_{80}$-PCBH as the active layer was annealed at varied conditions to enhance the device performance. P3HT:$Y_3N@C_{80}$ -PCBH was spin casted onto the PEDOT: PSS coated ITO glass substrates. 1.0% wt/vol blend solution of P3HT: $Y_3N@C_{80}$-PCBH in ortho dichlorobenzene (ODCB) is spin casted at 1000 rpm. The active layer was annealed before the electrode deposition and in some cases, the active layer was annealed before as well as after the electrode deposition. Figure 7.4 shows the EQE plot of the P3HT: $Y_3N@C_{80}$ -PCBH devices annealed at varied conditions. Annealing was either done before the electrode deposition (pre annealing) or in some of the devices, annealing was done before as well as after the electrode deposition. The EQE plot of the comparison of the blend devices is shown in Figure 7.4. The devices were either pre-annealed at 110 °C for 10 minutes or were pre- annealed at 110 °C for 10 minutes followed by post annealing done at 140 °C for 1 minute [8]. The devices with pre as well as post annealing cycles have better performance than the pre annealed devices.

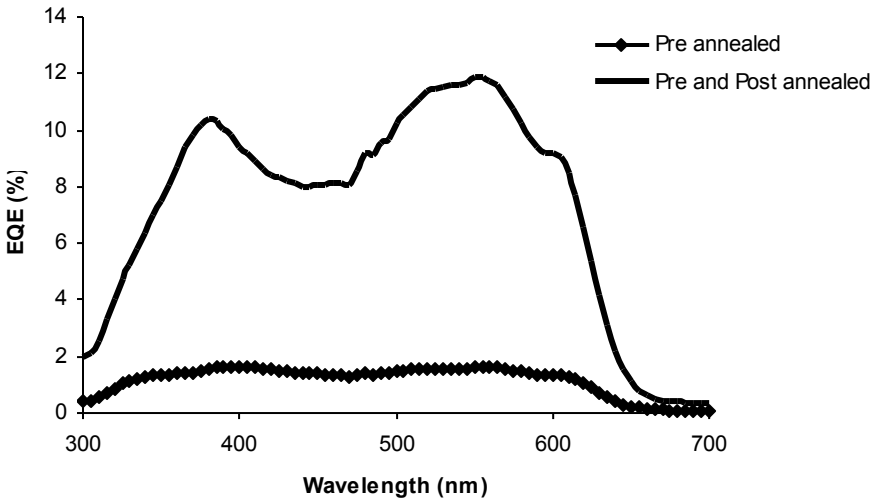

Figure 7.4 EQE plot of comparison of P3HT: $Y_3N@C_{80}$-PCBH; devices annealed at varied conditions.

Figure 7.4 shows the J-V characteristics of the P3HT:$M_3N@C_{80}$-PCBX (X = M, H) blend devices under AM1.5. The J-V plot shows the enhanced performance of the Y_3N endohedral fullerenes based devices which are pre as well as post annealed.

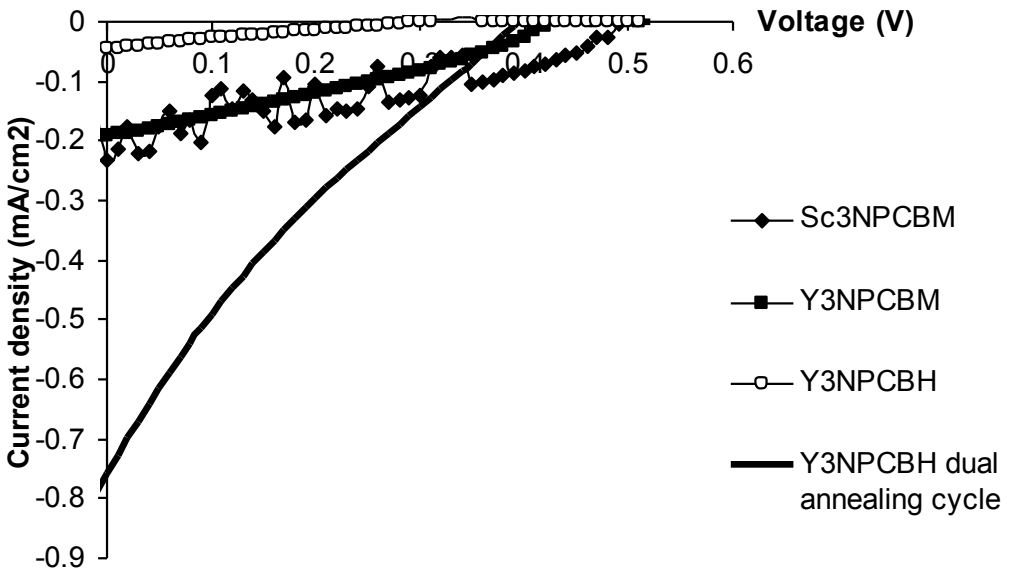

Figure 7.5 J-V characteristics of P3HT:$M_3N@C_{80}$ PCBX (X= M, H) bulk heterojunction devices

As is evident, Y_3N based devices have better performance than Sc_3N based devices. The devices with dual annealing cycles led to the enhancement in the performance. Table 7.2 shows the efficiency, FF, V_{OC} and J_{SC} for the different devices under AM1.5 illuminations.

Table 7.2 Efficiency (η), FF, V_{oc}, J_{sc}, RR values for P3HT: $M_3N@C_{80}$-PCBX (X=M,H) bulk heterojunction devices where M = Sc, Y, the donor material is P3HT in all of these devices.

Acceptor material	Thickness (nm)	Annealing Conditions	RR (at ±1V)	Voc (V)	J_{SC} (mA/cm^2)	FF	η (%)
$Sc_3N@C_{80}$ PCBM	25	Pre anneal 110 °C 5 minutes	326	0.505	-0.11	0.31	0.017
$Y_3N@C_{80}$ PCBM	20	Pre anneal 110 °C 5 minutes	63	0.425	-0.19	0.31	0.026
$Y_3N@C_{80}$ PCBH	20	Pre anneal 110 °C 10 minutes	17	0.215	-0.067	0.24	0.003
$Y_3N@C_{80}$ PCBH	20	Pre anneal 110 °C 5 minutes Post anneal 140 °C 1 minute	444	0.395	-0.76	0.2	0.06

As is evident from Table 7.2, the devices which are pre as well post annealed have better performance to the devices annealed before electrode deposition.

7.5 Summary of P3HT $M_3N@C_{80}$-PCBX devices (M = Sc, Y; X = M, H)

In this chapter, bulk heterojunction devices with P3HT as donor material and $M_3N@C_{80}$ –PCBX (M=Sc, Y; X= M, H) as an acceptor material are discussed. Figure 7.3 shows that, Y_3N based devices have better performance than Sc_3N based devices. This is mainly because of the better solubility. Also, the reduced energy offset of $Y_3N@C_{80}$ – PCBM with P3HT compared to $Sc_3N@C_{80}$ –PCBM with P3HT offers reduced losses in charge transfer and hence, better device performance.

Further, PCBH based endohedral fullerenes are studied and it was concluded that devices made with PCBH based endohedral fullerenes with P3HT have better device performance when the pre and post annealing is done on the devices. The better performance of devices based on PCBH based derivatives compared to PCBM based ones is due to their better solubility and miscibility to PCBM than the PCBM based derivatives. Also, the mobility values of PCBH based derivatives are close to PCBM. The devices with dual annealing cycles led to the enhancement in the performance. Figure 7.4 shows the EQE plot of the comparison of P3HT:$Y_3N@C_{80}$ –PCBH blend devices. The devices with pre as well as post annealing cycles have better performance than the pre annealed devices.

References

1. S. Stevenson, P.W. Fowler, T. Heine, J.C. Duchamp, G. Rice, T. Glass, K. Harich, E. Hajdu, R. Bible, H. C. Dorn, "A stable non-classical metallofullerene family". **Nature**, 408, 427-428, (2000).

2. S. Gunes, H. Neugebauer, N. S. Sariciftci,"Conjugated Polymer-Based Organic Solar Cells",**Chem. Rev.**,107, 1324-1338, (2007).

3. B. C. Thompson, J. M. J. Frechet, "Polymer–Fullerene Composite Solar Cells", **Angew. Chem., Int. Ed.**, 47, 58-77, (2008).

4. G. Dennler, M. C. Scharber, T. Ameri, P. Denk, K. Forberich, C. Waldaauf, C. J. Brabec, "Design rules for donors in bulk-heterojunction tandem solar cells - towards 15% energy-conversion efficiency", **Adv. Mater.**,20, 579-583, (2008).

5. C. Shu, W. Xu, C. Slebodnick, H. Champion, W. Fu, J.E. Reid, H. Azurmendi, C. Wang, K. Harich, H.C. Dorn, H.W. Gibson, "Syntheses and Structures of Phenyl-C_{81} Butyric Acid Methyl Esters (PCBMs) from $M_3N@C_{80}$", **Organic Letters**, 11, 8, 1753-1756, (2009).

6. F.B. Kooistra, J. Knol, F.Kastenberg, L.M. Popescu, W. J. H. Verhees, J.M. Kroon, J.C. Hummelen, "Increasing the Open Circuit Voltage of Bulk-Heterojunction Solar Cells by Raising the LUMO Level of the Acceptor", **Organic Letters**, 9, 4, 551-554, (2007).

7. A. Gopal, Effects of Thickness, Morphology and Molecular Structure of Donor and Acceptor Layers in Thermally Interdiffused Polymer Photovoltaics, (2007).

8. R.B. Ross, C.M. Cardona, D.M. Guldi, S. G. Sankaranarayanan, M.O. Reese, N.Kopidakis, J.Peet, B.Walker, G.C. Bazan, E.V.Keuren, B.C. Holloway and M. Drees, "Endohedral fullerenes for organic photovoltaic devices", **Nature Materials**, 8, 208-212, (2009).

Chapter 8
Conclusions and Future Work

Dual spin cast interdiffused polymeric photovoltaic devices in which donor and acceptor layers are sequentially spin cast have been studied at length in this thesis. The dual spin cast bilayer devices are heated under various temperature conditions in order to allow interdiffusion and optimize the device performance. Some work has also done on the bulk heterojunction devices and in some cases, the performance of the bulk heterojunctions and thermally interdiffused bilayers was compared. P3OT, P3HT and porphyrins have been used as the donor materials and PCBM has been primarily used as an acceptor in the work presented in this thesis. A brief study was also done on the TNT endohedral fullerenes as an acceptor with P3HT as the donor material in bulk heterojunction devices. The active layer thickness, annealing conditions and interdiffusion conditions were the key parameters studied in detail in order to optimize the device performance. The various device performance parameters such as power conversion efficiency, EQE, FF, efficiency, V_{oc}, J_{sc} and series resistance have been studied and compared for devices fabricated under different conditions.

P3OT:PCBM

The performance of P3OT:PCBM bulk heterojunction devices was studied by varying the active layer thickness and also by varying the annealing conditions. The devices with active layer thickness of 80 nm were found to have better device performance than the devices with active layer thickness of 50 nm or 110 nm. The

devices with thickness of 110 nm were found to have high series resistance, which is responsible for a decrease in the efficiency. The series resistance of the devices with thickness of 50 nm and 80 nm was found to be of the order of ~35 ohms. However, for devices with thickness ~ 50 nm, the active volume is quite small for efficient charge generation and hence there is a drop in the efficiency. In all of these cases, the devices were pre-annealed at 140 °C for 10 minutes.

In addition, the thickness was maintained at 80 nm and the annealing conditions were varied to study the device performance. The devices that were annealed at 140 °C have better performance compared to the devices annealed at 130 °C or 150 °C. Also for the same thickness, the increase of time of annealing from 5 minutes to 10 minutes, at 140 °C leads to degradation of device performance. The highest efficiency was obtained for devices annealed at 140 °C for 5 minutes. Power conversion efficiency of the order of 1.5% was obtained under AM1.5 solar simulated conditions for the P3OT:PCBM bulk heterojunction devices with active layer thickness of 80 nm.

Concentration gradient devices have been a success demonstrated for the P3OT:PCBM system. Bilayer devices, devices which were not annealed but interdiffused and the devices which were annealed as well as interdiffused were studied in detail. A systematic study done on the P3OT:PCBM interdiffused devices, found that interdiffused devices have dramatically better performance than the bilayer devices, demonstrating the importance of donor-acceptor proximity for efficient charge transfer. It was also concluded that annealing of the P3OT films before PCBM was spin cast, helps by increasing the crystallinity of the polymer and was not found to hinder the interdiffusion process. The devices which were interdiffused for 20 minutes at 150 ºC have the highest

performance. The thickness, interdiffusion temperature and time of interdiffusion are the three parameters which were primarily studied for their effect on the device performance. It was found that devices with 70 nm of P3OT and 40-50 nm of PCBM have the highest efficiency. Furthermore, the devices with 70 nm of P3OT and 40-50 nm of PCBM were interdiffused at 140 ºC and 150 ºC for various amounts of time. It was found that devices which were interdiffused for 20 minutes have better performance than the ones interdiffused for 10,30 or 40 minutes. An AM1.5G power conversion efficiency of 1.0% was obtained for devices in which a 70 nm P3OT film was annealed at 120 ºC followed by spin-casting of 40-50 nm thick PCBM from pyridine and interdiffusion of the two films at 150 ºC for 20 minutes.

The series resistance is another parameter studied in detail. The series resistance of the devices is calculated by plotting the differential resistance as a function of voltage. In the high limit voltage limit, the value of the differential resistance is series resistance. It was found that devices which were interdiffused at 140 ºC and 150 ºC for 20 minutes have the lowest series resistance. This indicates that devices with P3OT thickness of 70 nm and PCBM thickness of 40-50 nm when interdiffused at 150 °C for 20 minutes lead to the interpenetrating network that has the lowest series resistance. For interdiffusion done for a longer period, the films tend toward a homogenous donor-acceptor distribution that has less of the material that carries the majority carriers in the vicinity of the electrodes.

Since P3OT contains sulfur while PCBM does not, the sulfur content can be used to indicate the relative amount of P3OT in the film as a function of depth. Concentration gradient profiles of sulfur signal were studied by Auger spectroscopy, to determine the

extent of interdiffusion. The concentration gradient profiles show that, for the devices with highest performance, gradients extend all the way through the film ending just short of the electrodes. The concentration gradient profile of the devices interdiffused at 150 ºC for 20 minutes resemble closely to the profile of ideal interdiffusion, which provides these devices the best performance.

P3HT:PCBM

P3HT:PCBM bulk heterojunction devices with various thicknesses and annealing conditions were fabricated. Then, active layer thickness was maintained at 90 nm and the devices were pre-annealed at 110 ºC, 120 ºC, 130 ºC, 140 ºC and 150 ºC for 5, 10 and 15 minutes. The devices which were pre-annealed show a drop in devices efficiency from 3.3% to 1.1% under AM1.5G illumination as the temperature of annealing was increased from 110 °C to 150 °C. Also, with the increase in the time of annealing from 5 to 15 minutes at a particular temperature, there is a decrease in the efficiency of the devices. P3HT:PCBM blend / bulk heterojunction devices showed highest efficiency of 3.3% when the annealing is done at 110 °C for 5 minutes and the active device thickness was maintained at 90 nm.

Interdiffused devices with the same total active layer thickness were also studied. The P3HT thickness was maintained at 45 nm and the PCBM thickness was maintained at 40-50 nm. The performance of the interdiffused devices increased as the temperature of the interdiffusion was increased from 120 °C to 150 °C as this leads to a larger active volume where charge separation can take place. However, heating the bilayer beyond 150 °C and for a time period beyond 20 minutes, leads to the degradation in the device performance, which can be attributed to the accumulation of P3HT at the surface. Auger

spectroscopy and X-ray photoelectron spectroscopy were used to study the concentration gradient profiles of the sulfur signal. The gradient profiles of bilayer and interdiffused devices were studied and it was found that for devices which are interdiffused beyond 20 minutes at a particular temperature, the sulfur moves to the cathode surface. Thus, the devices which are interdiffused for longer period lead to decreased efficiency.

In order to compare the blends and bilayer interdiffused devices, devices with the same thickness and under similar heat treatments were compared. For the heat treatments which were done at 120 °C, the device performance of the blends is better than the interdiffused devices. However, as the temperature of the heat treatment is increased, the device performance of interdiffused devices becomes better than the blends heated at similar temperature. The active layer thickness was maintained at 90 nm.

The efficiency and FF under AM1.5G was plotted for blends which were annealed at 120 °C, 130 °C, 140 °C and 150 °C for 10 minutes and the bilayers which are interdiffused at the respective temperatures for 10 minutes and also at 160 °C. The device performance of the blends starts degrading as the annealing temperature is increased beyond 120 °C, however for interdiffused devices, the performance improves as the temperature of interdiffusion is increased from 120 °C to 150 °C.

P3HT:PCBM blends or bulk heterojunction devices have better device performance for the devices when the annealing is done at lower temperatures. As the time and temperature of the annealing is increased beyond 110°C, there is degradation in the efficiency. The device thickness was maintained at 90 nm for these pre- annealed P3HT PCBM bulk heterojunction devices.

However for P3HT/PCBM interdiffused devices, the device performance was better for devices interdiffused at 150°C. Heat treatments done at higher temperature increase the interpenetrating network of polymer and fullerene and lead to an increase in the efficiency of these devices.

Porphyrin:PCBM

Bulk heterojunction devices with the soluble porphyrin derivative ZnTPP and PCBM were studied. The device performance was studied by the variation of porphyrin to PCBM ratio and it was found that device with 1:9 ZnTPP: PCBM ratios have the better device performance. As there is an increase in porphyrin ratio, there is degradation in the device performance. Also, annealing of the devices, tends to degrade the device performance. The highest performance of the 1:9 weight ratio devices can be due to the better morphology and most favorable microstructure of the devices.

P3HT:$M_3N@C_{80}$ PCBX(M= Sc, Y ; X=M, H)

Bulk heterojunction devices with P3HT as donor material and $M_3N@C_{80}$ –PCBX (M=Sc, Y; X= M, H) as an acceptor material were fabricated and studied. The Y_3N based devices had better performance than the Sc_3N based devices which is mainly because of the better solubility. Also, the reduced energy offset of $Y_3N@C_{80}$ –PCBM with P3HT compared to $Sc_3N@C_{80}$ –PCBM with P3HT offers reduced energy losses upon charge transfer and hence, better device performance.

Further, PCBH based endohedral fullerenes were studied and it was concluded that devices made with PCBH based endohedral fullerenes have better device performance when the pre and post-annealing is done on the devices. The better

performance of devices based on PCBH derivatives compared to PCBM based ones is due to their better solubility and miscibility to P3HT than the PCBM based derivatives. Also, the mobility values of PCBH based derivatives are close to PCBM. The devices with dual annealing cycles led to the enhancement in the performance.

Future Work

In order to further optimize the performance of dual spin cast devices, new donor materials with lower band gap and higher mobility can be used as the donor material. The reduction in the band gap allows more photons to be absorbed from the solar spectrum which can increase the performance of the devices.

In work related to the porphyrins, a further enhancement in efficiency could be achieved with a porphyrin derivative having mobility on a par with PCBM. The electron mobility of PCBM is of the order of ~10^{-3} cm^2/Vs, as compared to the hole mobility of ZnTPP which is of the order 10^{-10} cm^2/Vs. Thus, new donor and acceptor materials, having higher mobilities and that are soluble in common solvents for solution processing can be used to fabricate the BHJ solar cells at their optimum ratios. In the future, this can be used to boost the performance of porphyrin and phthalocyanine BHJ solar cells fabricated by solution processing.

The TNT endohedral devices presented in this thesis have active layer thickness of the order of ~25 nm which is quite small. Hence by increasing the thickness, the active volume where photons can be absorbed increases and hence is expected to show enhancement in the device performance.